Dissertation
submitted to the
Combined Faculties for the Natural Sciences and for Mathematics
of the Ruperto-Carola University of Heidelberg, Germany
for the degree of
Doctor of Natural Sciences

Put forward by

M.Sc. Yapeng Zhang
born in Gansu, China

Oral examination: 22th January, 2013

${}^{3}_{\Lambda}$H and ${}^{4}_{\Lambda}$H Production in Ni+Ni Collisions at 1.91A GeV

Referees: **Prof. Dr. Norbert Herrmann**

Prof. Dr. Johanna Stachel

Zusammenfassung

Diese Arbeit beschäftigt sich mit der ersten experimentellen Beobachtung des pionischen Zweikörperzerfalls von ${}^{3}_{\Lambda}$H und ${}^{4}_{\Lambda}$H in Ni+Ni-Kollisionen bei 1.91A GeV. Das Experiment wurde mit dem FOPI Spektrometer am SchwerIonen - Synchrotron SIS18 an der GSI durchgeführt. Der analysierte Datensatz besteht aus 56×10^6 Ereignissen, die den zentraleren Anteil von etwa 60% des gesamten Reaktionswirkungsquerschnittes ausmachen. Die rekonstruierte invariante Masse von ${}^{3}_{\Lambda}$H beträgt 2.9926 ± 0.0017 GeV/c^2 und hat eine Signalbreite von 5.6 ± 1.0 MeV/c^2. Bei ${}^{4}_{\Lambda}$H wurde eine invariante Masse von 3.9226 ± 0.0010 GeV/c^2 und eine Breite von 4.0 ± 1.6 MeV/c^2 gemessen. Die ${}^{3}_{\Lambda}$H- und ${}^{4}_{\Lambda}$H-Signale wurden nur in bestimmten Phasenraumbereichen in der $p_t/m - y_{lab}-$Ebene beobachtet. Die statistische Signifikanz dieser Signale beträgt 5.6 für ${}^{3}_{\Lambda}$H und 4.2 für ${}^{4}_{\Lambda}$H. Unter Anwendung der differentiellen Zerfallszeiteffizienz, die mittels einer vollständigen MonteCarlo Simulation des Experimentes bestimmt wurde, konnte für ${}^{3}_{\Lambda}$H eine mittlere Lebensdauer von $263\pm64(\text{sta})\pm44(\text{sys})$ ps und für ${}^{4}_{\Lambda}$H eine von $196\pm75(\text{sta})\pm43(\text{sys})$ ps ermittelt werden. Die Produktionsraten pro Ereignis für ${}^{3}_{\Lambda}$H und ${}^{4}_{\Lambda}$H liegen unter Berücksichtigung der jeweiligen Zerfallsbreite und der Rekonstruktioneffizienz bei 7.5×10^{-4} und 1.3×10^{-4}. Als Produktionsmechanismus wird die Koaleszenz von Λ Hyperonen mit den Spektatorfragmenten in den Ni+Ni Kollisionen bei 1.91A GeV diskutiert. Es wird gezeigt, dass die Voraussagen mit dem gemessene Ergebnis nicht übereinstimmen. Des weiteren werden die ${}^{3}_{\Lambda}$H/^{3}He und ${}^{4}_{\Lambda}$H/^{4}He Produktionsverhältnisse mit Vorhersagen des statistischen Modells zur Teilchenproduktion verglichen.

Abstract

${}^{3}_{\Lambda}$H and ${}^{4}_{\Lambda}$H are identified from their two-body π^--decay channel in Ni+Ni collisions at 1.91A GeV for the first time. The experiment was performed by the FOPI spectrometer at the SIS18 of GSI. The analyzed data sample consists of 56×10^6 events covering the most central 60% of the total reaction cross section. The reconstructed invariant mass of ${}^{3}_{\Lambda}$H is 2.9926 ± 0.0017 GeV/c^2 with a width of 5.6 ± 1.0 MeV/c^2, and the one of ${}^{4}_{\Lambda}$H is 3.9226 ± 0.0010 GeV/c^2 with a width of 4.0 ± 1.6 MeV/c^2. The significance of the ${}^{3}_{\Lambda}$H and ${}^{4}_{\Lambda}$H signal is 5.6 and 4.2, respectively. The ${}^{3}_{\Lambda}$H and ${}^{4}_{\Lambda}$H signal is observed in a certain phase space region in the $p_t/m - y_{\text{lab}}$ plane only. By applying the differential decay time efficiency obtained from MC simulation, the mean lifetime of ${}^{3}_{\Lambda}$H and ${}^{4}_{\Lambda}$H is found to be $263\pm64(\text{sta})\pm44(\text{sys})$ ps and $196\pm75(\text{sta})\pm43(\text{sys})$ ps, respectively. By taking reconstruction efficiency and the decay branching ratio into account, the yield of ${}^{3}_{\Lambda}$H and ${}^{4}_{\Lambda}$H for the analysed event sample is 7.5×10^{-4} and 1.3×10^{-4} per event, respectively. The ${}^{3}_{\Lambda}$H and ${}^{4}_{\Lambda}$H production in Ni+Ni at 1.91A GeV via coalescence process is naively discussed and it is shown that the observed results are not compatible with the expectations. The yield ratio of ${}^{3}_{\Lambda}$H/^{3}He and ${}^{4}_{\Lambda}$H/^{4}He is compared with the predictions of the thermal model for hadron chemistry.

Contents

List of Figures

List of Tables

Overview

This thesis presents the results of ${}^{3}_{\Lambda}$H and ${}^{4}_{\Lambda}$H production in relativistic heavy-ion collisions at a beam energy of 1.91A GeV in the Ni+Ni system. The experiment was carried out in March of 2008 with the FOPI detector at the 'Schwerionensynchrotron'(SIS) of 'Gesellschaft für Schwerionenforschung' (GSI), Darmstadt.

In the first chapter of the thesis, the general motivations for studying heavy-ion collisions (HICs) are briefly reviewed. The kinematics of HICs and the scenarios for hypernuclei productions in HICs are described. The current measurement status of the strangeness bound states, e.g. the hypernuclei and kaonic bound states, is presented.

In chapter two, the geometrical configuration and the performance of the sub-detectors of the FOPI spectrometer are described. In chapter three, the variables, used to characterise the events, are introduced. The particle identification methods are described here as well.

In chapter four, the procedure used to reconstruct the invariant mass of particles decaying into two charged products, and the mixed event technique, used to reproduce the combinatorial background, are explained. The selection criteria for the two-body π^--decay of ${}^{3}_{\Lambda}$H and ${}^{4}_{\Lambda}$H are introduced. With those selection cuts, the invariant mass spectrum of (π^-,^{3}He) and (π^-,^{4}He) pairs in various phase space regions is obtained. The significance of the ${}^{3}_{\Lambda}$H and ${}^{4}_{\Lambda}$H signal and its dependence on the production options is evaluated.

In the fifth chapter, the results of the Geant simulation and analysis of the background and the signal events are shown. The detection efficiency of ${}^{3}_{\Lambda}$H and ${}^{4}_{\Lambda}$H in various phase space regions is derived. In order to extract the mean lifetime of ${}^{3}_{\Lambda}$H and ${}^{4}_{\Lambda}$H, the differential decay time efficiency of ${}^{3}_{\Lambda}$H and ${}^{4}_{\Lambda}$H is obtained, respectively.

Chapter six presents the final results of this work. Firstly, the yields of the charged particles, Λ hyperon, ${}^{3}_{\Lambda}$H and ${}^{4}_{\Lambda}$H in the phase space regions concerned are finalized. The mean lifetime of ${}^{3}_{\Lambda}$H and ${}^{4}_{\Lambda}$H is obtained by applying the corresponding differential decay time efficiency. The favored impact parameter range for ${}^{3}_{\Lambda}$H and ${}^{4}_{\Lambda}$H production is discussed. Afterwards, the coalescence scenario for the hypernuclei production in HICs is naively discussed, based on the measured particle yields. The yield ratio of ${}^{3}_{\Lambda}$H/^{4}He and ${}^{4}_{\Lambda}$H/^{4}He are compared with the thermal predictions.

In the last chapter, the results and the conclusions of this work are summarised. The future perspectives and the still open questions are discussed.

Chapter 1

Introduction

Heavy-ion collisions (HICs) are considered to be a powerful tool in studying the properties of strongly interacting matter. Matter with extreme temperature and density is created during a heavy-ion collision, typically referred to as "fireball". In HICs at the SIS18 accelerator of GSI, where beam energies of 1 - 2 GeV/nucleon are available, the density inside the fireball can reach values of 2-3$\cdot\rho_0$ with $\rho_0 = 0.17$ fm^{-3} representing the ground state density of nuclear matter as it is found in the center of large nuclei. The available energy is sufficiently high that a new quark degree of freedom called "strangeness" can be created. Mesons like π, K, ρ, ϕ and baryons like $\Lambda,\ \Sigma,\ \Delta,\ N^*$ are produced in the fireball. Inevitably, those particles would interact with the surrounding hadronic matter and may eventually bind with conventional nucleons forming new few-body states, like hypernuclei or K^--nucleus bound states. Since these reactions happen in an environment of non-zero baryon density and the properties of hadrons may be modified by the surrounding medium, cross sections and reaction rates could be modified as well. Therefore, HICs provide a possibility to study the in-medium properties of hadrons by investigating the production of hypernuclei and K^--nucleus bound states. Like the nucleon-nucleon (NN) interaction, the hyperon-nucleon (YN) and the hyperon-hyperon (YY) interaction are of fundamental interest in hadron physics. Due to the short lifetime of the hyperons, the YN or YY interaction can not be well investigated in hyperon scattering experiments. The study of hypernuclei is the only effective way to access the YN and YY interaction.

In this chapter, first the properties of hadronic matter and its equation of state are briefly reviewed. The kinematics of HICs and the collective behavior of particle emission are discussed. In the second part, the historical developments and the basic properties of single-Λ hypernuclei are presented. For completeness concerning the probes of in-medium properties of hadrons, the status of the search for kaonic bound states is briefly described.

1.1 Hadronic matter

The bulk properties of hadronic matter are the macroscopic features of a many-body system, which can be characterised by thermodynamic parameters, e.g. temperature

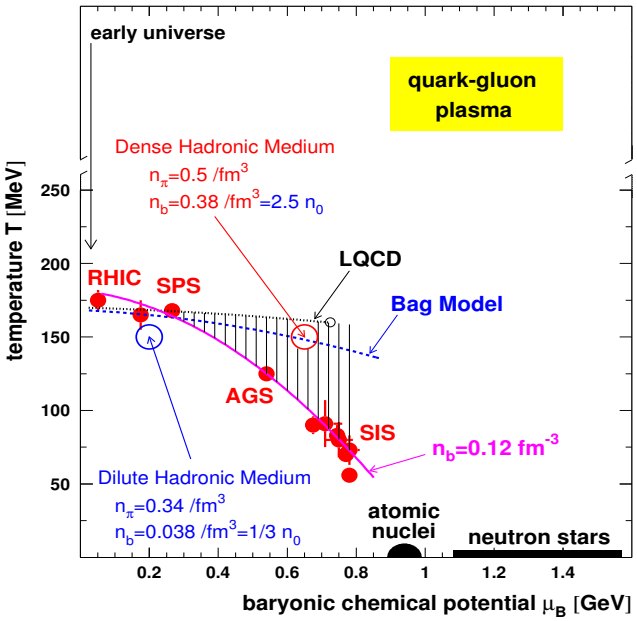

Figure 1.1: Phase diagram of hadronic matter in the plane of temperature T and baryon chemical potential μ_b. The red points are the thermodynamic parameters determined from the experiments at RHIC, SPS, AGS and SIS. The figure is taken from [1].

T, pressure P and baryon chemical potential μ_b. Under different conditions, hadronic matter appears in various forms, which are called the phases of hadronic matter. This is in analogy to the description of water that for different temperatures and pressures exists in the form of ice, liquid and vapor.

1.1.1 Phases of hadronic matter

High-energy HIC experiments provide a unique opportunity to explore the phases of strongly interacting matter in the laboratory. In HICs at RHIC/LHC energies, the hadrons are expected to be dissolved leading to a deconfined phase of free quarks and gluons. This state is referred to as a quark-gluon plasma (QGP). The properties of QGP are the main research topic at ultra-relativistic energies. In HICs at moderate energies like those available or planned for at SIS, AGS, SPS and FAIR, a first-order phase transition between hadronic and partonic matter is expected to occur. Exploring the phase boundary and the properties of the hadrons in the nuclear medium are the main research topics.

The phases of hadronic matter and the experimental data from HICs are connected by the quantities of the statistical model [1]. A phase diagram expressed in the temperature T and baryon chemical potential μ_b plane is shown in Fig. 1.1. The red filled circles depict the parameter pairs determined by a thermal analysis of hadron multiplicities measured in central Pb+Pb or Au+Au collisions at SIS, AGS, SPS and RHIC energies. All data points are in close vicinity to the solid curve (magenta), corresponding to a constant baryon density of $n_b = 0.12$ fm^{-3}. This suggests that the chemical freeze-out takes place at a constant total baryon density. The dashed and the dashed-dotted line are representing the predictions from lattice QCD and bag model calculations for the

first-order phase transition from the hadron gas phase to the QGP phase.

In the region above the freeze-out line at moderate temperatures and high baryon density, a quarkyonic phase is suggested in [2,3]. In this phase, the quarks are still confined inside the hadrons. The high energy density is mainly due to the excitation of quarks from the deep Fermi sea, which could allow the system to reach chemical and thermal equilibrium faster.

In the region below the freeze-out line the hadronic matter is in a hadron gas phase, which exists until the hadrons liquefy. The liquid phase is found in normal nuclei described by the thermodynamic parameters T=0 and $\mu = m_N(\sim 1$ GeV). When the nuclei are heated up to tens of MeV, the nucleons are evaporated from the liquid phase to the hadron gas phase. The first order phase transition line ends in a critical point beyond which the phase separation between liquid and gas phase disappears. The critical end point temperature of this phase transition is measured to be about 5-10 MeV [4]. The matter in the interior of neutron stars is in the high chemical potential and low temperature phase, which is indicated by the black band in the lower-right corner of Fig. 1.1.

1.1.2 Nuclear equation of states

The nucleon-nucleon (NN) interaction is attractive at a distance of 1 to 2 fm and becomes repulsive at small separation distance (< 0.5 fm). The nuclear equation of state (EOS) describes the compressional energy as a function of nuclear matter density. The EOS governs the interior structure of the neutron stars and the supernova explosions. In an equilibrated nuclear matter system with density ρ and temperature T, the total energy per nucleon can be decomposed into a thermal contribution E_t and a compressional part E_c [6],

$$E(\rho, T) = E_c(\rho) + E_t(\rho, T) + E_0 \tag{1.1}$$

where, $E_0 \sim 931$ MeV is the rest energy of a nucleon at equilibrium density. The EOS is characterized by the incompressibility κ_∞, which is defined by the following formula,

$$\kappa_\infty = 9\rho_0^2 \left(\frac{d^2(E/A)}{d\rho^2} \right)_{\rho=\rho_0}, \tag{1.2}$$

where E is the total energy of the system, A is the number of participating nucleons and ρ is the nuclear density. The average density of normal nuclei is $\rho_0 = 0.17$ fm^{-3}. The binding energy of the nucleus is given by the Weizsäcker formula. For an infinite system of symmetric hadronic matter at temperature $T = 0$, in the absence of Coulomb interactions, the energy per nucleon has a minimum energy of -16 MeV that is obtained from the volume term of the Weizsäcker mass formula [7]. The EOS can be probed by various experimental techniques, e.g. the giant monopole resonance, the observation of supernovae and neutron stars, the collective flow, the meson ($\pi^\pm$, kaon) production in HICs and so on. Hitherto, κ has been constrained to a range of 200-400 MeV [8,9,10,11,12]. If $\kappa > 250$ MeV, this case is called "hard" EOS while if $\kappa < 250$ MeV the EOS is named "soft". EOS curves with different values of the incompressibility are sketched in Fig. 1.2, the green line represents

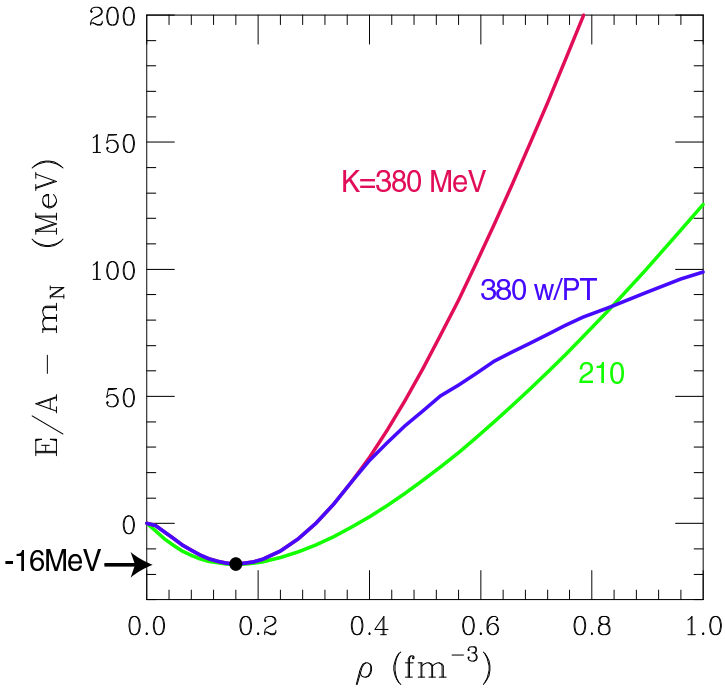

Figure 1.2: Energy per baryon as a function of baryon density ρ. Equations of state with different incompressibility values of κ = 210 MeV (green line), 380 MeV (red line) and 380 MeV with a high-density phase transition (blue line) at T=0 are shown. The binding energy of the ground states is $E = -16$ MeV and $\rho = \rho_0$. The figure is taken from [7].

a "soft" EOS with κ = 210 MeV, the red line is given by a "hard" EOS with κ = 380 MeV, the blue line is found using κ = 380 MeV while taking the contribution of a phase transition into account.

Since a wide range of nuclear density can be created by HICs at different energies, HICs are a suitable tool to investigate the EOS. For example, in HICs at SIS18 energies, the central density of the collisions can reach 2-3ρ_0. For Au+Au collisions at incident energies of 20 - 30 A GeV, the density in the overlap region is expected to reach up to 8ρ_0. Different EOS would influence the collective behavior of emitted particles in HICs effectively. By comparing the measured data to transport model calculation, e.g. BUU [13] and IQMD [14], the incompressibility can be extracted. Currently, the measured data from the HICs can not be described by the theory with a single κ value [7].

1.1.3 Heavy-ion collisions

In the past decades, HICs became a powerful tool to investigate the properties of strongly interacting matter under extreme conditions [10] , which are otherwise inaccessible. The heavy-ion reactions at various energies have been investigated by many fixed target experiments at BEVALAC/SIS(∼2A GeV), AGS(∼12A GeV) and SPS(∼160A GeV) energies, and by collider experiments at RHIC(∼200A GeV) and LHC (∼4A TeV) energies. In non-central HICs, the matter that does not participate in the fireball creation, is referred to as spectator matter. At different energies, the interaction strength between the fireball and the spectator is different, which is strongly related to the possible hypernuclei and $\bar{K}$-nucleus bound states production in HICs.

In order to illustrate how strong the fireball interacts with the spectators in non-central

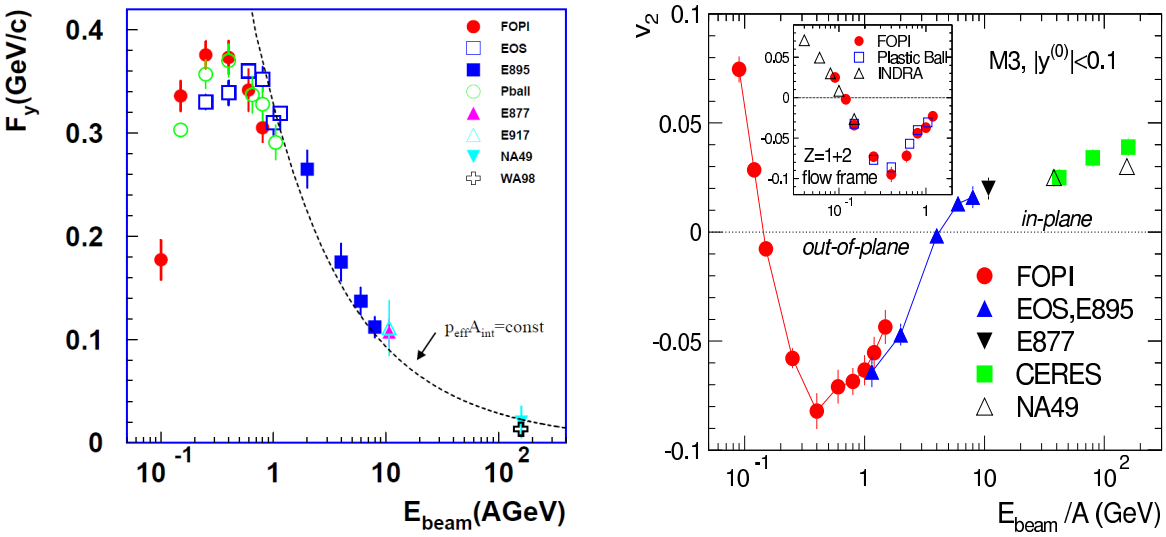

Figure 1.3: Excitation function of the sideflow (left), the dashed line is a calculation under the assumption that a constant force acts on the spectators during the passage time, the figure is taken from [17]. Excitation function of integral elliptic flow (right) in Au+Au system, the figure is taken from [19].

HICs, generally two time scales need to be considered in the center of momentum frame: (a) the passing time of spectators t_{pass} and (b) the expansion time t_{exp} of the fireball. The passing time of spectators is calculated by

$$t_{pass} = \frac{R_p + R_t}{\gamma_{beam} \cdot \beta_{beam} c}, \tag{1.3}$$

where R_p and R_t are the radii of projectile and target nucleus respectively, β is the velocity of the spectator, γ is the corresponding Lorentz factor and c is the speed of light in vacuum. If t_{pass} is far less than t_{exp}, the fireball would expand according to its internal pressure gradient and temperature. If t_{pass} is slower compared to t_{exp}, then the spectators would prevent the fireball from expanding in the direction with the largest pressure gradient. The matter in the fireball would be emitted perpendicular to the reaction plane. The reaction plane is spanned by the impact parameter (the distance between the center of the two involved nuclei in the transverse plane) and the velocity direction of the incident particle. In both cases, i.e. "$t_{pass} < t_{exp}$" and "$t_{pass} > t_{exp}$", the spectator matter and the fireball matter are moving exhibiting common trends, referred to as "collective flow". From the pattern of the final azimuthal angular distribution, these two cases can be distinguished.

The azimuthal angular distribution of emitted particles in HICs can be expanded into a Fourier series [15, 16], the coefficients of the first and the second order term are called the sideflow and the elliptic flow, respectively. The sideflow quantifies how strong the spectator-like matter is deflected in the reaction plane, the elliptic flow is the measure of particle anisotropic emission in the transverse plane [17].

The left panel of Fig. 1.3 shows the excitation function of baryon sideflow [17]. The dashed line is calculated under the assumption that a constant force acts on the spectators

during the passage time. A decreasing sideflow with increasing beam energy means that the "force" integral, as felt by the spectators, from the overlapping zone is decreasing with increasing beam energy due to the decreasing passage time. An excitation function of elliptic flow in Au+Au system [18, 19] is shown in the right panel of Fig. 1.3. By increasing the incident beam energies (>1 GeV/A), the pattern of elliptic flow changes substantially and its sign turns from negative to positive, which means that the impact of the spectators on the fireball expansion gets weaker with increasing beam energy.

The emission pattern of sideflow and elliptic flow vividly illustrates that the hot fireball matter strongly interacts with the cold spectator matter in HICs at SIS18 energies (1-2A GeV). In HICs at these energies, the hadrons, like the pion, the kaon, the Λ hyperon and etc. abundantly produced in the fireball, strongly interact with the cold spectator matter in the nuclear medium. Since the properties of hadrons may be modified by the nuclear medium, the cross sections and reaction rates of reactions with such particles may be modified as well. It is also possible that these hadrons may be absorbed by the cold spectator matter, a few-body system with a special composition can be formed. The hypernuclei and the kaonic bound states could be the probes for such in-medium processes. Contrarily, in HICs at high energies, since the interaction strength between the fireball matter and the spectator matter becomes weaker with increasing beam energy, such exotic states production by the interactions between the spectator and the fireball is less likely to happen. The research status of these concerned exotic clusters, i.e. hypernuclei and kaonic bound states, is briefly described in the following sections.

1.2 Strangeness bound states

Interactions between the hadrons are the fundamental building-blocks of hadron physics. The nucleon-nucleon (NN) interaction is extensively investigated by NN scattering experiments and the bound states only containing conventional "u" and "d" quarks are satisfactorily explained by phenomenological methods and meson-exchange interactions. Due to the short lifetime of hyperons, the hyperon-nucleon (YN) and hyperon-hyperon (YY) interaction can not be investigated well within the hyperon scattering experiment. An interesting and important question is whether the NN interaction can be extended from the quark flavor of SU(2) to SU(3). Fortunately, one or more hyperon(s) ($\Lambda, \Sigma, \Xi, \Omega, \ldots$) could bind with conventional nuclei, referred to as hypernuclei. Investigating the properties of hypernuclei, such as binding energy, lifetime, decay mode and so on, gives access to YN and YY interactions. Beside the bound states with a strange baryon, K^- may be trapped by a normal nucleus and form a deeply bound kaonic state.

This section is composed of two parts. In the first part, the historical developments and the basic properties of hypernuclei are briefly presented. The connection between the YN interaction and neutron stars is reviewed as well. The experimental and theoretical status of hypernuclei production in HICs is described. In the second part, the research status of deeply bound kaonic states is reviewed briefly.

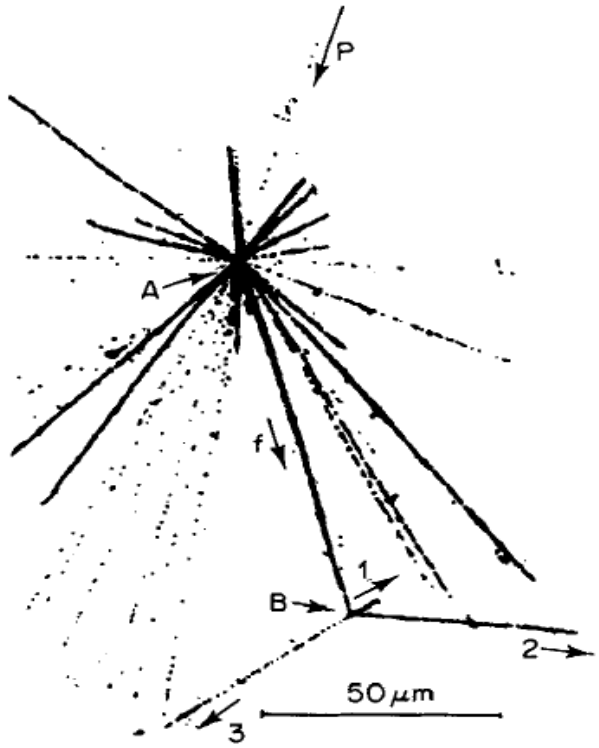

Figure 1.4: First hypernuclear event. The track P is an incident cosmic ray, which interacted with a nucleus of an emulsion at point A. The track "f" is the produced hypernucleus. After flying about 600 μm, it decayed into three charged particles at B. The short thick trajectory 1 is a heavy cluster, thick track 2 is a heavy energetic particle, the thin track 3 is most probably a pion. The figure is taken from [20].

1.2.1 Λ hypernuclei

A hypernucleus is designated by the symbol ${}^{A}_{Y}Z$, where Z is the symbol of the chemical element, A is the total number of baryons (i.e. the number of nucleons and hyperon(s)), and Y is the symbol of the corresponding hyperon. For example, ${}^{3}_{\Lambda}\mathrm{H}$ represents a bound state of a proton, a neutron and a Λ hyperon.

Since a hyperon inside the nucleus is not subject to the Pauli principle, it can be placed in the interior of nucleus. On the other hand, due to the presence of the hyperon, the mean field of the nucleons changes. This allows one to study the possible new structures and properties of nuclei, like magic numbers. Meanwhile, the hypernuclei also provide information about the in-medium properties of the YN interaction. With this new degree of freedom, the nuclei chart can be extended into another dimension. The single-Λ hypernuclei are widely investigated and the YN interaction is obtained by spectroscopically investigating the Λ hypernuclei. YN and YY interactions are important in understanding the structure and the composition of compact stellar objects, like neutron star.

In this section, a historical overview of Λ hypernuclei is presented firstly. Secondly, the basic properties of single-Λ hypernuclei are described. In the third part, the connection between the hypernuclear physics and the neutron star is presented. In the last part, the experimental and theoretical status of hypernuclei production in HICs is reviewed.

Historical overview

The hypernucleus was first discovered by the Polish physicists Marion Danysz and Jerzy Pniewski in 1952 [20], the observed event is shown in Fig. 1.4. A high energy proton

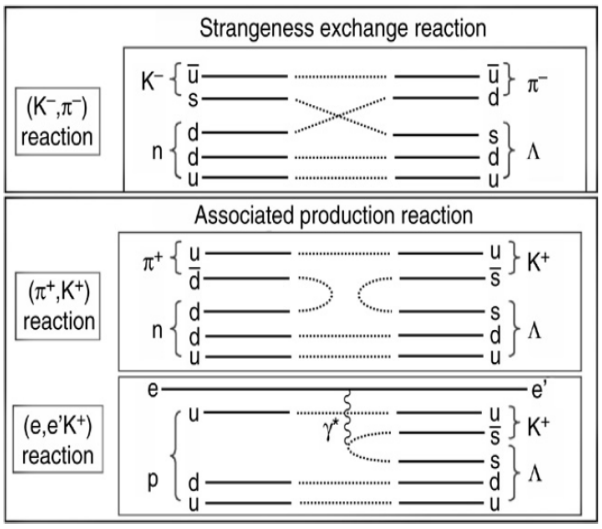

Figure 1.5: Schematic presentation of three Λ hyperon producing reactions, e.g. the strangeness exchange reaction (upper), the π-induced reaction (middle) and $(e, e'K^+)$ reaction (lower). The figure is taken from [31].

(track P) collided with a nucleus of an emulsion at point A. A large number of fragments were produced. One fragment (track f) flew about 600 μm, and decayed into three charged particles at point B. The short thick trajectory 1 is a heavy cluster, thick track 2 is an energetic heavy particle and the thin track 3 is most probably a pion. This fragment is assigned to be a hypernucleus. This weakly decaying particle marked the start of hypernuclear physics.

About 20 years after the first hypernuclear observation, about 22 different hypernuclear species, produced by secondary pion and K^- beam, were measured by emulsion and bubble chambers. The Λ binding energies and the decay mode of light hypernuclei ($3 < A < 16$) were investigated [21]. In the early 1970's, K^- beams were used at CERN, and later on at BNL, the strangeness exchange reaction ($K^-N \rightarrow \Lambda\pi$, see Fig. 1.5) was used to produce hypernuclei. For the strangeness exchange reaction (K^-, π^-), the Λ hyperon can only be populated at substitutional states due to small momentum transfer, i.e. the neutron at the outer shell is converted into a Λ hyperon. This is a powerful tool to study the structure of p-shell hypernuclei [22, 23], but these kinds of experiments were often limited by poor statistics and low beam energy resolution. In the middle of the 1980's, the π^+ beam was used to explore the Λ hypernuclear spectroscopy at AGS [24, 25] and KEK [26, 27]. The hypernuclear spectroscopy was established based on the high-quality single-Λ hypernuclear data. Comparing to the strangeness exchange reaction, the (π^+, K^+) reaction has a larger momentum transfer. Λ hyperon can populate the inner shells of nuclei. In 2002, the (e,e'K^+) production was first realised at the Thomas Jefferson National Accelerator Facility (JLab) [28]. The beam energy resolution was significantly improved from the few MeV of K^-, π^+ beam to a few hundred keV, which can resolve the spin-orbit spiltting of a Λ hyperon inside the nucleus.

A schematic presentation of the strangeness exchange reaction (K^-, π^-) and associated

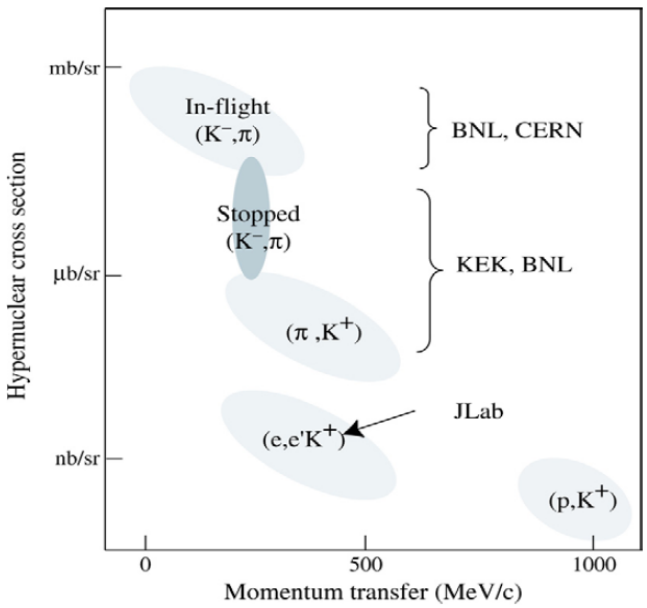

Figure 1.6: Hypernuclear production cross section for various reactions versus momentum transfer. The figure is taken from [31].

production reactions of (π^+, K^+) and $(e, e'K+)$ are shown in Fig. 1.5. The typical hypernuclear production cross section for various reactions versus the transfered momentum is sketched in Fig. 1.6. For the (K^-, π^-) reaction, a recoilless Λ hyperon can be produced at the so called "magic momentum" of an incident kaon at about $p_{K^-} = 0.55$ GeV/c [29]. For the (π^+, K^+) reaction, the cross section peaks at $p_{\pi^+} = 1.05$ GeV/c, where the cross section is about one order of magnitude smaller than the cross section of strangeness exchange reactions [30, 31].

A large number of single-Λ hypernuclei, from the lightest ${}^{3}_{\Lambda}$H to the heaviest ${}^{208}_{\Lambda}$Bi, have been observed, these are compiled in Fig. 1.7 [31]. The abscissa is the mass number and the y-axis is the charge of the hypernucleus. The employed experimental techniques i.e. (K^-, π^-), $(\pi^{\pm}, K^+)$, $(e, e'K^+)$, γ-induced reaction and emulsion data are indicated.

$\Lambda - N$ interaction

The nucleon-nucleon (NN) interactions can be described by the one-pion-exchange (OPE) model [32]. Due to the fact that the isospin (I) of Λ hyperon is $I = 0$, a single pion with isospin I=1 can not be exchanged between a Λ hyperon and a normal nucleon with isospin $I = 1/2$. The exchange of particles with zero isospin, like η, ω, and the strange mesons, like K, K^*, are allowed. These mesons are much heavier than a pion, therefore only within certain distances which is shorter than the one of the reactions with pion exchange, the $\Lambda - N$ interaction becomes effective.

In the absence of the Pauli effect for a Λ hyperon inside the nucleus, the Λ hyperon behaves like an independent particle relative to the core nucleus. The Hamiltonian of the hypernuclei can be written as

$$H = H_{Core} + T_{\Lambda} + \sum v_{\Lambda N}^{effective}, \tag{1.4}$$

where H_{Core} is the Hamiltonian for the core nucleus, T_{Λ} is the kinetic energy of the Λ

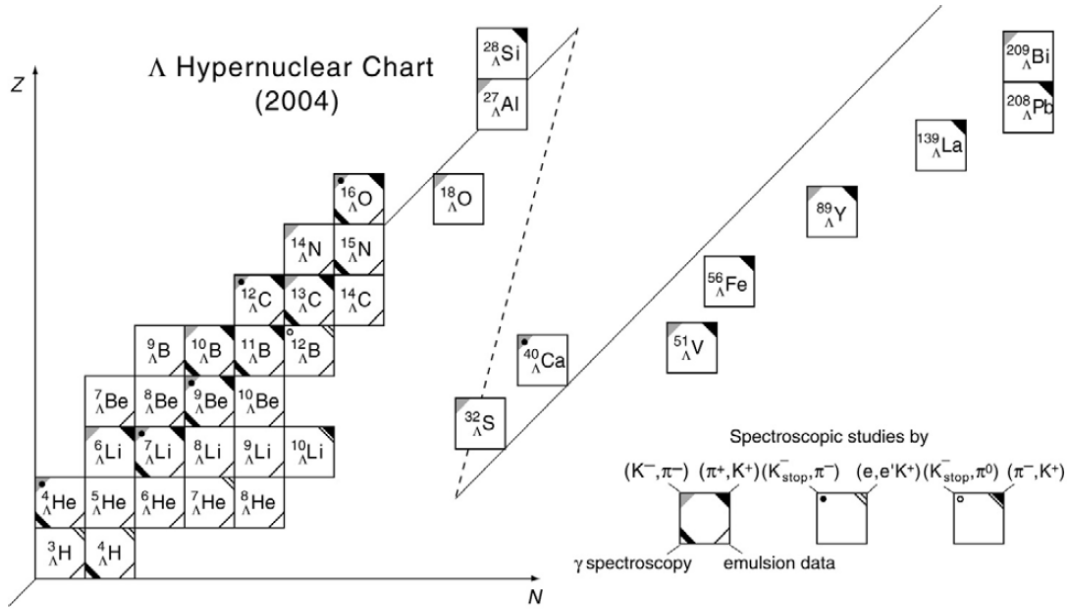

Figure 1.7: Λ hypernuclear chart. The employed experimental techniques, i.e. $(K^-, \pi^-.)$ reaction, $(\pi^\pm, K^+)$, $(e, e'K^+)$, γ-induced reaction and emulsion data, are shown. The figure is taken from [31].

hyperon and $\sum v_{\Lambda N}^{effective}$ is the sum of ΛN interactions. Phenomenologically, the shell model has successfully explained the nuclear transition and the fine structure of a normal nucleus. In the same manner, a Λ hyperon with spin 1/2 in a single-particle orbit couples with a nuclear core state. The effective potential of a p-shell Λ hypernuclei can be parameterized as [33, 34],

$$V_{\Lambda N} = V_0(r) + V_\sigma(r)\cdot s_N\cdot s_\Lambda + V_\Lambda(r)\cdot L_{\Lambda N}\cdot\sigma_\Lambda + V_N(r)\cdot L_{\Lambda N}\cdot\sigma_N + V_T(r)\cdot s_{12} \tag{1.5}$$

where, $V_0(r)$ is the averaged central interaction, $V_\sigma(r)$ is the spin-spin interaction, $V_\Lambda(r)$ is the Λ-spin-orbit interaction, $V_N(r)$ is the core-spin-orbit interaction, $L_{\Lambda N}$ is the relative orbital angular momentum, $V_T(r)$ is the tensor interaction and s_{12} is the tensor operator defined by,

$$s_{12} = 3(\sigma_n\cdot r)(\sigma_\Lambda\cdot r) - \sigma_\Lambda\cdot\sigma_N. \tag{1.6}$$

These calculations describe the experimental data quite reasonably, especially for the Λ binding energy and its γ-transitions. The effective interactions can be calculated by one-boson-exchange (OBE) models such as those of Nijmegen [35] and Jülich interactions [36], the parameters used in the models are constrained by the ΛN and ΣN scattering data. These kinds of studies are essential to understanding the YN interaction in low medium density ($\rho < \rho_0$) environment. In dense hadronic medium however the YN interaction is still unknown.

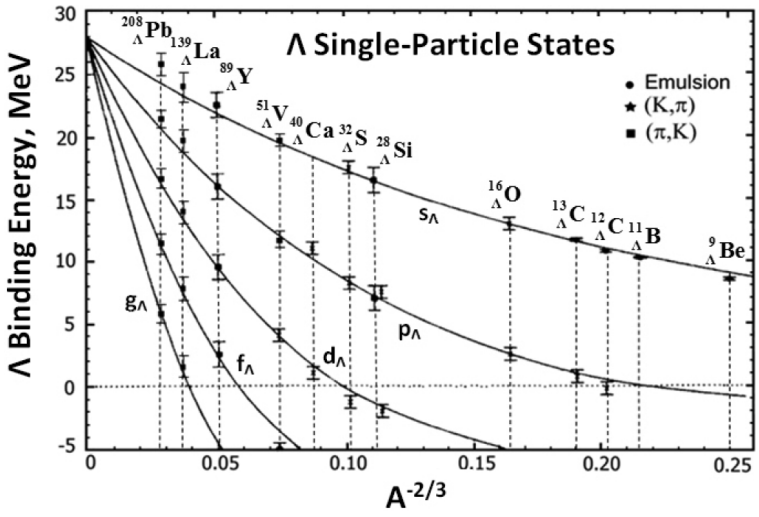

Figure 1.8: Λ binding energy B_Λ obtained from π^+, K^- beam and early emulsion data as a function of $A^{-2/3}$, where A is the mass number of the core nucleus. The curves are the solutions obtained for a Woods-Saxon well with a depth of 28 MeV and a radius parameter $r_0 = 1.128 + 0.439A^{-2/3}$ [38]. The figure is taken from [39].

Λ Binding Energy

A single-Λ hypernucleus can be treated as a core nucleus plus an additional Λ hyperon. The mass of a hypernuclus (M_{hyp}) is derived from the measured momentum vectors of the incident particle, for instance π^+ and outgoing particle K^+ (see Fig. 1.5), which is expressed as the following

$$M_{hyp}c^2 = \sqrt{(E_{\pi^+} + M_A c^2 - E_{K^+})^2 - [(p_{\pi^+}c)^2 + (p_{K^+}c)^2 - 2c^2 p_{\pi^+} p_{K^+} \cos\theta]}, \quad (1.7)$$

where M_A is the mass of the target nucleus, E_{π^+} and E_{K^+} are the total energy of the incident π^+ and outgoing K^+ respectively, θ is the scattering angle of the kaon with respect to the incident direction of the π^+. The Λ binding energy B_Λ is deduced by assuming that the core nucleus is in its ground state,

$$B_\Lambda = M_{core}c^2 + M_\Lambda c^2 - M_{hyp}c^2 \quad (1.8)$$

where M_{core} is the mass of the core nucleus, and $M_\Lambda = 1.1156$ GeV/c^2 is the mass of the Λ hyperon. In general, the single-Λ hypernuclear potential can be expressed in Woods-Saxon form as [37]

$$U_\Lambda = V_0^\Lambda f(r) + V_{LS}^\Lambda \left(\frac{h}{m_\pi c}\right)^2 \frac{1}{r}\frac{\mathrm{d}f(r)}{\mathrm{d}r}(\vec{l}\cdot\vec{s}) \quad (1.9)$$

with

$$f(r) = \frac{1}{1 + \exp\left(\frac{r-R}{a}\right)}, \quad (1.10)$$

where $R = 1.1(A-1)^{1/3}$ fm, $a = 0.6$ fm, $V_0^\Lambda = -30$ MeV, $V_{ls}^\Lambda = 2.0$ MeV. The item $\vec{l}\cdot\vec{s}$ is the contribution of the spin-orbit coupling. Taking this coupling into account, the fine structures in the measured excitation spectra of Λ hypernuclei can be satisfactorily described.

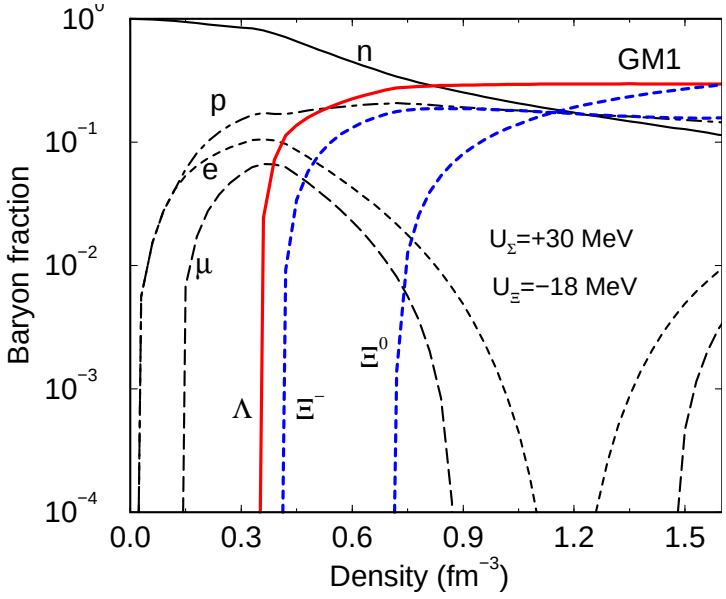

Figure 1.9: Possible composition of neutron star matter as a function of baryon density. The hyperon appears above density $2\rho_0$ with a repulsive Σ potential. The figure is taken from [45].

The Λ binding energies of hypernuclei measured by K^-, π^+ induced reactions and early emulsion experiments versus $A^{-2/3}$ are shown in Fig. 1.8, where A is the mass number of the core nucleus [38] (the data points were updated in [39]). The curves are the solution obtained for a pure Woods-Saxon well with a depth of 28 MeV and a radius parameter $r_0 = 1.128 + 0.439A^{-2/3}$. The determined hypernuclear potential depth is close to 30 MeV, which is about 2/3 of a normal nuclear potential by extrapolating the binding energies to nuclear matter.

Hypernuclei and neutron stars

The neutron star is a type of stellar remnant that results from the gravitational collapse of a massive star. Neutron stars are the densest objects in existence in the universe with typical radii of about 10 km and masses of about 1-2 solar mass. The density of the neutron star increases from outer crust to the inner layers. The density in the center of a neutron star is expected to be several times higher than the normal nuclear density ($\rho_0 = 0.17$ fm^{-3}). The pressure caused by gravity is balanced by the Fermi pressure originating from the Pauli exclusion principle and the short-range repulsion between the nucleons. The maximum mass of a neutron star is constrained by the stiffness of the EOS. A stiffer EOS can sustain more gravitational force, which allows a neutron star to have a larger mass. Thus, the masses of observed neutron stars provide a stringent constraint on the EOS.

By increasing the nuclear density, various forms of matter are predicted to appear in the interior of a neutron star, such as hyperonic matter [40], kaon condensation [41, 42], and color superconductor [43, 44]. These new degrees of freedom would soften the EOS, and reduce the maximum mass of a compact star. The particle composition in the core of a neutron star is not known precisely. A possible composition of neutron star matter as a function of baryon density is shown in Fig. 1.9 [45]. The red line represents the fraction

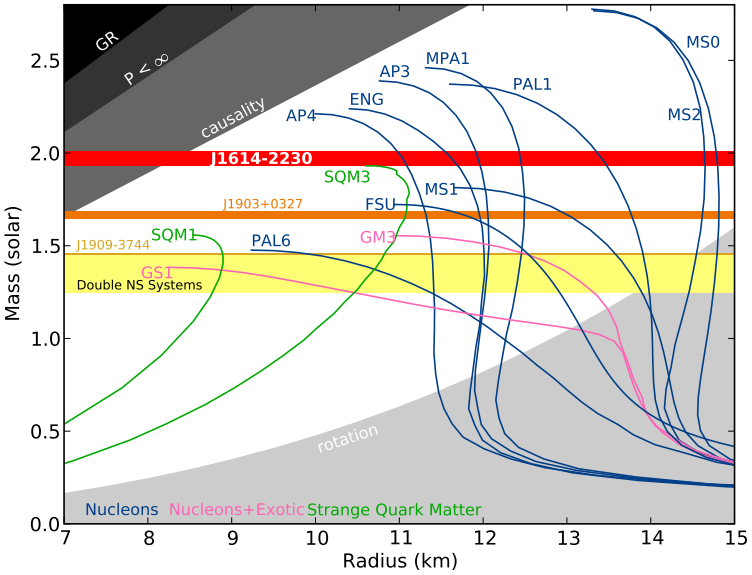

Figure 1.10: Mass-radius diagram of the neutron star. The horizontal bands are the observed neutron star masses. The lines are giving the mass as a function of radius under several EOS assumptions. The figure is taken form [46].

of the Λ hyperon. The Λ hyperon is predicted to appear at nuclear densities exceeding $2\rho_0$. The fraction of hyperonic matter is governed by the strength of the YN interaction in the nuclear medium.

Recently, the mass of the binary millisecond pulsar J1614-2230 was measured to be 1.97 ± 0.04 solar masses [46]. The mass-radius diagram of neutron stars is depicted in Fig. 1.10, the horizontal bands are the observed neutron star masses. The curves are giving the mass as a function of the radius under various EOS assumptions. The authors conclude that non-nucleonic components in the neutron star are unlikely.

This result is rather puzzling. On the one hand, the theory predicts that the Λ hyperon would appear at baryon density exceeding $2\rho_0$, which is consistent with hypernuclear data. On the other hand, the presence of Λ hyperons would soften the EOS, and it reduces the maximum mass of a neutron star to be about $1.5M_\odot$ [47]. So far, the role of the Λ hyperon in the neutron star is still an open question.

One possible underlying reason is the missing three-body force for nucleons and hyperons (NNN, YNN, YYB and YYY), which gives an additional repulsive contribution. This kind of information can be extracted by investigating the properties of double hypernuclei [45, 47]. In-medium YN interaction would play an important role for the composition and structure of the neutron stars [48, 49]. Since no such data is available at this moment, the results strongly depend on the theoretical models.

Hypernuclei production in HICs

The Λ hyperon and other mesons like $\pi^{\pm}, \rho, K^{+}$ are abundantly produced in the fireball of HICs at intermediate energies. A particular feature of non-central HICs at such energies is that the fireball matter strongly interacts with the spectator matter, which has been described in section 1.1.3. In the course of these interactions, hypernuclei could be formed by following processes:

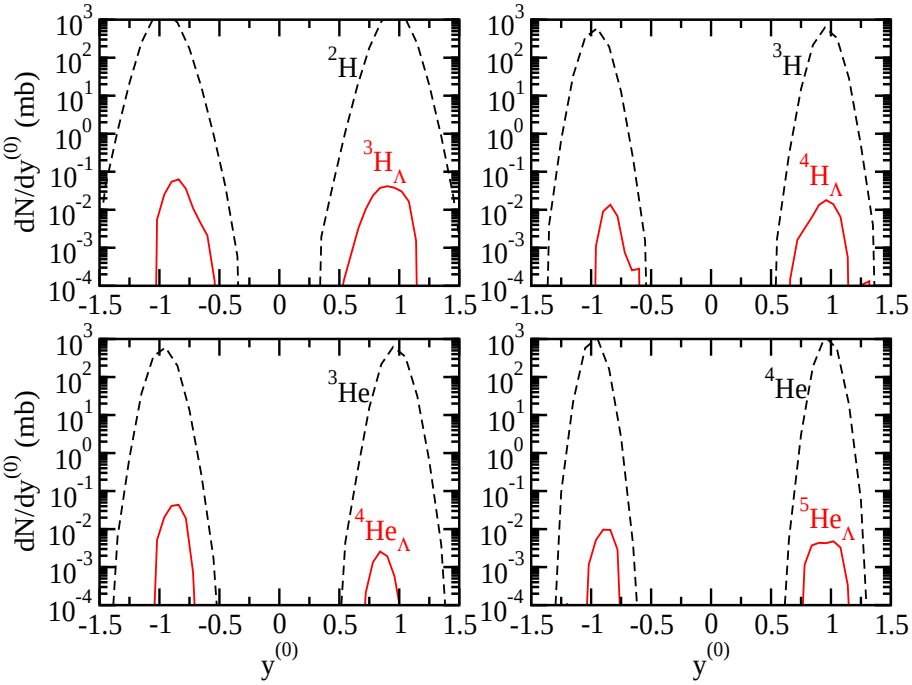

Figure 1.11: Predicted differential cross section of ${}^{3}_{\Lambda}$H (upper left), ${}^{4}_{\Lambda}$H (upper right), ${}^{4}_{\Lambda}$He (low left) and ${}^{5}_{\Lambda}$He (low right) (solid red line) and their core nucleus (dashed black line) as a function of scaled rapidity distribution in ^{12}C+^{12}C at 2A GeV. The figure is taken from [13].

- **Coalescence process:** a Λ hyperon produced in the fireball may stick with a cluster from the surrounding medium, especially those from the spectator matter.
- **Meson-induced reaction:** mesons like pions and kaons produced in the fireball may interact with the spectator matter. The hypernuclei can be formed by the strangeness exchange reaction (K, π) or the associated pion-induced reaction (π, K).

- **Direct reaction:** the produced Λ hyperon may directly react with the spectator matter to form a hypernucleus, such as the strangeness exchange reaction and the knock-out reaction. The knock-out reaction has been used to probe the rare isotopes of conventional hadronic matter [50, 51], one or more nucleons in a nucleus can be replaced by an injected Λ hyperon.

The coalescence picture was first proposed by Kerman and Weiss [52] theoretically in the 1970's. Later, more sophisticated coalescence models [53, 54, 55] were developed. Recently, the combined transport model GiBUU [56] and statistical multi-fragmentation model (SMM) [57, 58] are used to predict the yield of light hypernuclei, by taking the contributions from both Λ-fragment coalescence and meson induced reaction into account. Basically, the produced Λ hyperon and other fragments are propagated in momentum and coordinate space. The hypernuclei production probability depends on two coalescence parameters: the momentum radius p_C and the spatial radius r_C, which are correlated by the relation $r_C = \hbar/p_C$ [59]. The strength of p_C depends on the strength of the YN

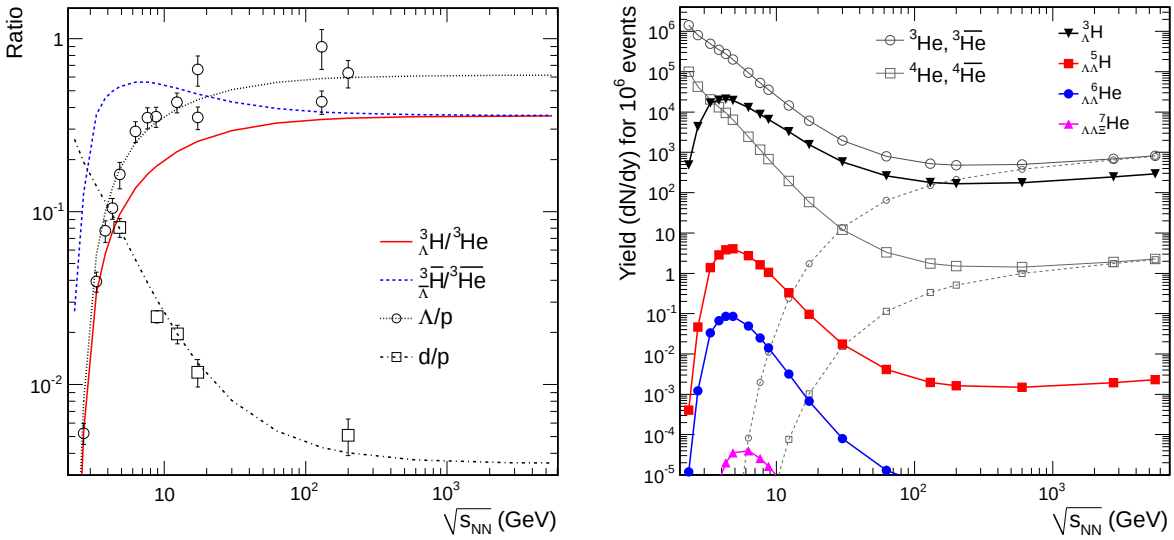

Figure 1.12: Predicted hypernuclei yields as a function of energy (left). Energy dependence of various yield ratios (right). Lines are the predictions and symbols in the left panel are the measured data. The figures are taken from [65].

interaction. Typically this is fitted from the measured experimental data. Due to the shortage of hypernuclear production data from HICs and the poor knowledge about the YN and YY interactions, the parameter p_C is not well constrained so far.

Fig. 1.11 shows the differential cross section of $^3_\Lambda$H (upper left), $^4_\Lambda$H (upper right), $^4_\Lambda$He (low left) and $^5_\Lambda$He (low right) (solid red line) and their core nucleus (dashed black line) as a function of scaled rapidity y^0 (defined by $(y_{lab}-y_{cm})/y_{cm}$, where y_{cm} is the rapidity of the collision system in laboratory frame) in ^{12}C+^{12}C collisions at 2A GeV, predicted by the GiBUU+SMM model [13]. The estimated hyperfragment production is about 5∼6 orders of magnitude lower than its core nucleus production. For the $^4_\Lambda$H yield prediction, the π-induced reaction contributes about 12% of the total $^4_\Lambda$H production, while the contribution from anti-kaon-induced reaction is neglected in the prediction. The third production scenario has not been discussed at all, since no Λ hyperon beam is available to investigate such reactions.

The spectator-like clusters are involved in all the above mentioned processes, properly describing the phase space distribution of light spectator-like fragments is as important as describing the one for particles produced in the fireball. An obstacle that should be mentioned is that the fraction and the phase space distribution of spectator-like fragments in HICs at energy E >1A GeV can not be properly described by transport models. However the velocity distribution of heavy fragments from the HICs with energies E<1A GeV [60,61] can be reasonably described by the SSM model [13] and the empirical formula [62].

Another model considered is the thermal model [63, 64]. This model can successfully reproduce the particle yield ratios in central relativistic HICs by only two parameters, i.e. the temperature T and the baryon chemical potential μ_b. The thermal model is one of

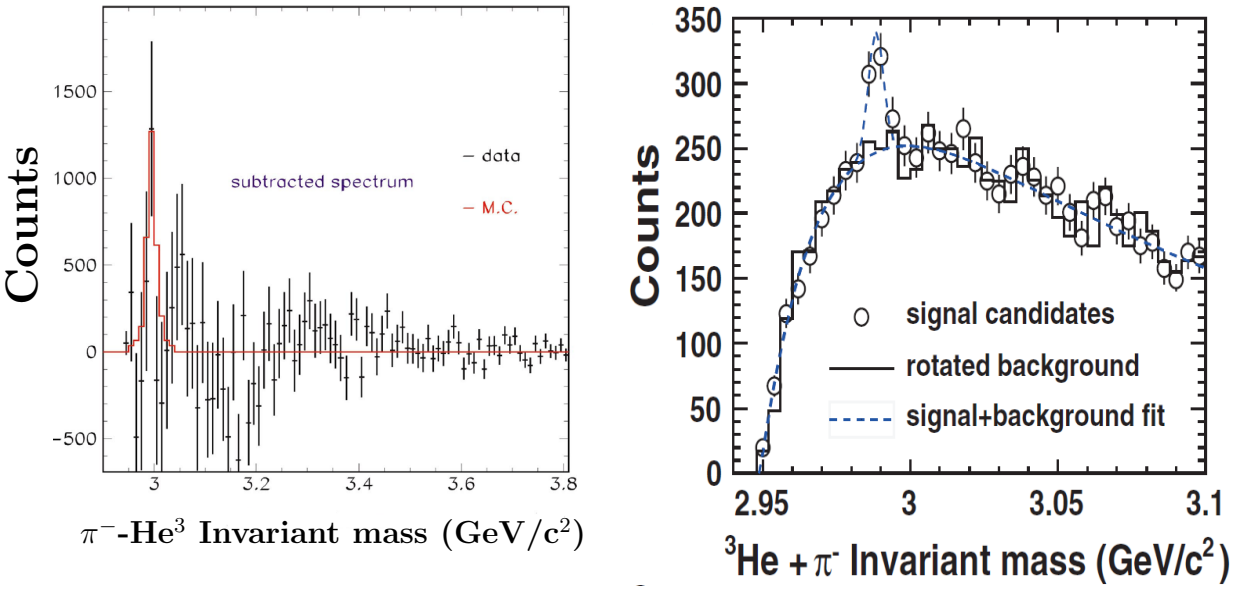

Figure 1.13: Invariant mass spectrum of measured (π^-,^{3}He) pairs (black dots) from Au+Pt at 11.5A GeV and MC simulation (solid red line) (left), the figure is taken from [69]. Invariant mass distribution of (π^-,^{3}He) pairs in Au+Au at 200A GeV (right). The open circles are the measured data, the solid line is the background. The dashed line is the summed result of fitted Gaussian (signal) and double-exponential (background) function. The figure is taken from [70]

the most direct approaches to investigate the hadron production in HICs, assuming that the whole system reaches a thermal and chemical equilibrium.

The left panel of Fig. 1.12 shows the yield ratios of baryons predicted by the thermal model as a function of the center of mass energy [65]. The lines are the predictions and the symbols are the measured data. The yield ratio of Λ/p and d/p is well reproduced by the model. The right panel of Fig. 1.12 shows the predicted yields of various particles at mid-rapidity per million central collisions as a function of the center of mass energy [65]. From this model, not only the single strangeness hypernuclei are predicted, but also the multi-strangeness hypernuclei ${}^{5}_{\Lambda\Lambda}$H, ${}^{6}_{\Lambda\Lambda}$He, ${}^{7}_{\Lambda\Lambda\Xi}$He are predicted. It is interesting to compare the yield of ^{3}He and ${}^{3}_{\Lambda}$H, as they have comparable phase space distributions. At low center of mass energy ($\sqrt{s_{NN}} < 3$ GeV), the yield ratio of ${}^{3}_{\Lambda}$H/^{3}He drops rapidly. At $\sqrt{s_{NN}} > 10$ GeV, the yield ratio of ${}^{3}_{\Lambda}$H/^{3}He is almost a constant.

Experimental status of hypernuclei production in HICs

The hypernucleus productions in HICs have been measured by several experiments. The first attempt to produce the hypernucleus via HICs was implemented at LBL in the 1970's [66]. The ^{16}O beam at 2.1A GeV impinged on a polyethylene target. It was claimed that more than 20 ${}^{16}_{\Lambda}$H's were observed. Late the 80's, light hypernuclei were measured at the JINR [67, 68] with a streamer chamber. Light-ion beams (^{3}He,^{4} He,^{6} Li and ^{7}Li) impinged on a polyethylene target, the cross sections and the mean lifetimes of ${}^{3}_{\Lambda}$H and

${}^{4}_{\Lambda}$H were measured. Note that both above experiments have no particle identification. A 2.5σ level ${}^{3}_{\Lambda}$H signal and the upper limit of ${}^{4}_{\Lambda}$H production were measured by the E864 collaboration [69] from 1.3×10^{10} most central (10%) Au+Pt collisions at 11.5A GeV. The measured invariant mass spectrum of (π^-,^{3}He) pairs and Monte Carlo (MC) simulation result is shown in the left panel of Fig. 1.13. Recently, the signal of ${}^{3}_{\Lambda}$H and anti-${}^{3}_{\Lambda}$H were observed in Au+Au collisions at 200A GeV by the STAR collaboration [70]. About 157 ± 30 ${}^{3}_{\Lambda}$H and 70 ± 17 anti-${}^{3}_{\Lambda}$H were observed from about 89 million minimum-bias events. The invariant mass spectrum of (π^-,^{3}He) pairs from the measurement is shown in the right panel of Fig. 1.13. The open circles represent the measured data, the background spectrum (solid line) is obtained by a method in which the heavier daughter particle is rotated by 180^o in the azimuthal plane. The background and signal is fitted by a double-exponential function and a Gaussian function respectively. The dashed line is the summed result of both functions. The result of both the E864 and the STAR collaboration is interpreted as a coalescence result of Λ hyperons, protons and neutrons from the fireball. More recently, ${}^{3}_{\Lambda}$H and ${}^{4}_{\Lambda}$H signals were observed by the HypHI collaboration by colliding ^{6}Li beam at 2A GeV on a carbon target [71]. The invariant mass of the Λ hyperon, ${}^{3}_{\Lambda}$H and ${}^{4}_{\Lambda}$H was reconstructed, and their means were shifted, which was attributed to a poor quality in their track fitting process.

1.2.2 $\bar{K}$-bound states

An attractive $\bar{K}$-nucleus potential was derived from the scattering length of low energy K^- scattering experiments [72, 73, 74, 75] and the level shifts of kaonic hydrogen X-ray measurements at the KEK-PS [76], DEAR [77] and SIDDHARTA [78]. The theoretical prediction for the depth of the K^--nucleus potential at normal hadronic matter density can be classified as a deeply attractive potential of -Re$V_{opt}(\rho_0)$ ≈150-200 MeV [79,80] and a shallower attractive potential of -Re$V_{opt}(\rho_0)$ ≈50-70 MeV [81, 82, 83, 84]. Based on the strongly attractive potential in isospin $I = 0$ K^-N interaction, the proton-rich deeply bound kaonic states, such as $pK^-(\Lambda\ 1405)$, ppK^- and $ppnK^-$, are predicted by Akaishi and Yamazaki [85,86,87]. Fig. 1.14 depicts the calculated $\bar{K}N$ and $\bar{K}$-nucleus potentials and their bound levels. An interesting feature of the prediction is that the size of the $\bar{K}$-nucleus would shrink due to the strong attractive K^-N potential. In particular, the $\Lambda(1405)$ is assumed to be a bound state of a K^- and a proton, which is the fundamental building block for studying the property of $\bar{K}$ in various many-body systems. The two-pole structure of $\Lambda(1405)$ was predicted in [88], since the $\Lambda(1405)$ mass is located between the $\pi\Sigma$ and $\bar{K}N$ threshold with isospin I=0 and strangeness S=-1. One pole is located at higher energy around 1426 MeV with a narrower width of 32 MeV and mostly couples to $\bar{K}N$, another one sits at lower energy around 1390 MeV with a larger width 132 MeV and mostly couples to $\pi\Sigma$. The nominal $\Lambda(1405)$ is not a single resonance but a superposition of these two states with the same quantum numbers.

Experimentally, there are several measurements interpreted as evidence for deeply bound kaonic states. The first experimental evidence of a kaonic bound state was observed by the FINUDA collaboration [89]. The low momentum K^- from ϕ decay were stopped on ^{6}Li, ^{7}Li and ^{12}C nuclei. The back-to-back emitted (p, Λ) pairs in the lab frame are

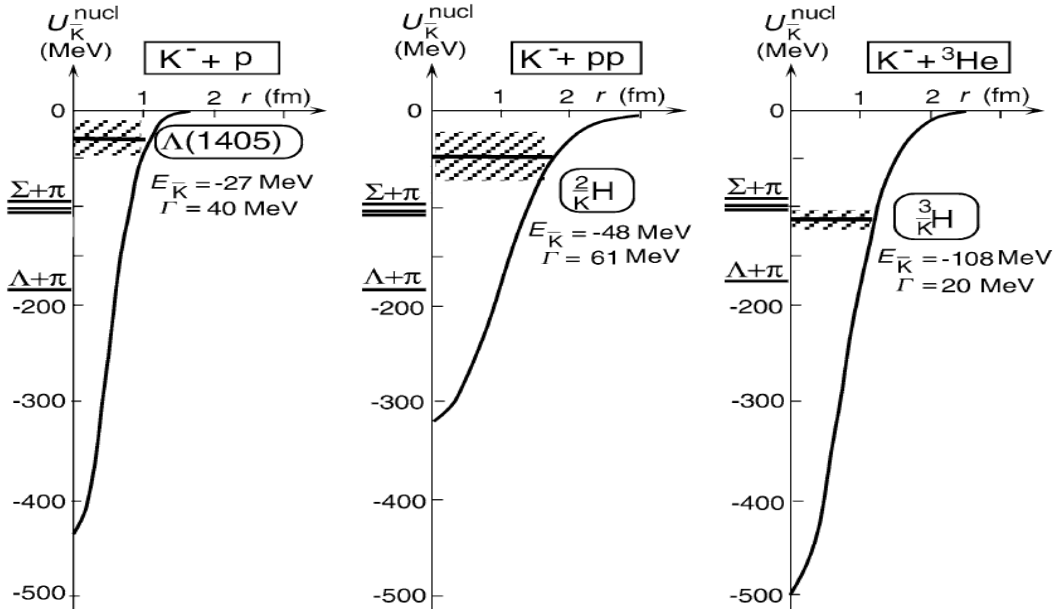

Figure 1.14: Theoretically predicted several deeply bound kaonic states in light nuclei by coupled-channel calculations. The figure is taken from [85].

selected and their invariant masses were reconstructed. The results are shown in the left panel of Fig. 1.15. The bump in the spectrum was interpreted as a bound state composed of a kaon and two protons, abbreviated as ppK^-. From the spectrum after acceptance correction (insert of Fig. 1.15), the binding energy and width of this hypothetical ppK^- bound state is $115^{+6}_{-5}(\text{stat})^{+3}_{-4}(\text{syst})$ MeV and $67^{+14}_{-11}(\text{stat})^{+2}_{-3}(\text{syst})$ MeV, respectively. This result was alternatively interpreted as final state interactions (FSI). The FSI effect on the proton and Λ hyperon after a quasi free absorption would reduce the invariant mass of the Λ-p system [90]. The FSI effect can not, however, explain the angle correlation of back-to-back emitted Λ hyperon and p. Another measurement in the $p+p \rightarrow K^+X$ reaction at 2.85 GeV was performed by the DISTO experiment [91]. The deviation of missing-mass spectra (DEV) of K^+ were achieved by selecting the large-angle proton ($|\cos\theta_{cm}(p)| < 0.6$) and the small-angle proton ($|\cos\theta_{cm}(p)| > 0.6$). In both cases, the polar angle of the K^+ was restricted to a range of $-0.2 < \cos\theta_{cm}(K^+) < 0.4$. The DEV is the ratio of the measured spectrum and the simulated spectrum, bin by bin. The simulation spectrum was calculated from a reference reaction, i.e. $pp \rightarrow pK^+\Lambda$, with a uniform phase space distribution. The DEV of K^+ with a large-angle proton cut is shown in the right panel of Fig. 1.15. The mean and width of the broad peak is $2267 \pm 3(\text{sta.}) \pm 5(\text{sys.})$ MeV/c^2 and $118 \pm 8(\text{sta.}) \pm 10(\text{sys.})$ MeV, respectively. This was claimed as being a K^-pp cluster with a large binding energy of B_K=103 MeV. More recently, in elementary pp reactions at 3.5 GeV, the feasibilities of $\Lambda(1405) \rightarrow \Sigma^{\pm}\pi^{\mp}$ have been demonstrated by the HADES collaboration [92].

Beside the elementary reactions, the information of the $\bar{K}N$ potential can be extracted from HICs as well. In HICs at energy larger than 2.5A GeV, K^- can be produced by direct reaction $NN \rightarrow NNK^+K^-$. The HICs at energies below the K^- production

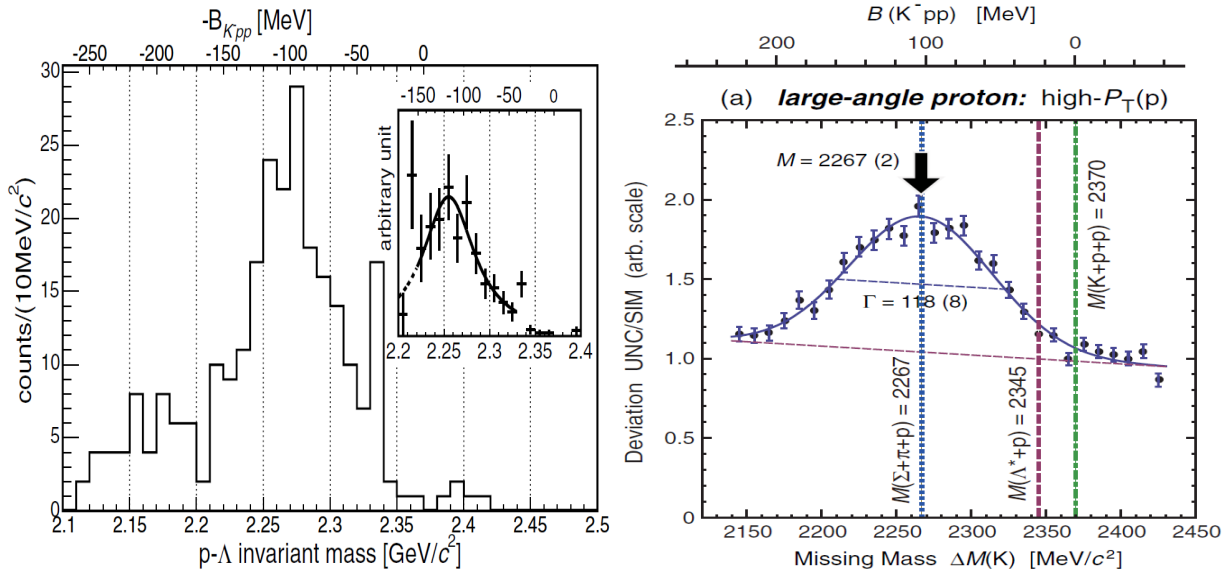

Figure 1.15: Invariant mass spectrum of the Λ-p pairs in the stopped K^- reacting on various nuclei measured by the FINUDA experiment (left), the figure is taken from [89]; K^+ missing mass spectrum in $pp \rightarrow p\Lambda K^+$ reaction at 2.85 GeV measured by the DISTO experiment (right), the figure is taken from [91].

threshold energy, K^- can be produced via multi-step reactions (mostly by $\pi Y \rightarrow NK^-$ [93]). At SIS18 energies, the measured K^- overall yield of Ni+Ni at 1.93A GeV is about 1×10^{-3} [94]. Due to the attractive $\bar{K}N$ potential, the K^- may be absorbed by the surrounding hadronic matter, especially by the cold spectator matter in non-central HICs at intermediate energies. In Al+Al collisions at 1.91A GeV and Ni+Ni collisions at 1.93A GeV measured by the FOPI detector, an excess was observed in the invariant mass spectrum of Λ-p pairs [95]. The invariant mass spectra of $\Lambda - p$ pairs from Al+Al system (left) and Ni+Ni system (right) are shown in Fig. 1.16. In the upper figure of each panel, the black solid spectrum and red-dashed histogram are the signal and the mixed-event background spectrum, respectively. The invariant mass spectrum after subtracting the background is shown in the lower figure of each panel. The excess was fitted by a Gaussian distribution. The fitted mean and width of the excess in the Al+Al system were 2121 ± 10 MeV/c^2 and 25 ± 5 MeV/c^2, respectively. For the Ni+Ni system, the fitted mean and width were 2140 ± 10 MeV/c^2 and 25 ± 5 MeV/c^2 respectively. In both cases, the significance of the signal is larger than 5σ. Note that the measured mean of the excesses is different from the Λ-p invariant mass located in 2.22-2.33 GeV/c^2 measured by the FINUDA [89] and the DISTO [91] collaborations. Similarly, in the analysis of Λ-d correlations in Ni+Ni collisions at 1.93A GeV measured by the FOPI apparatus, an excess is found at 3.137 GeV/c^2, which could be a bound state of $ppnK^-$ [96]. It is worth mentioning that the $\bar{K}N$ potential is predicted to change with the medium density [97, 98, 99]. The influence of this effect on the formation of deeply bound kaonic states is still unknown.

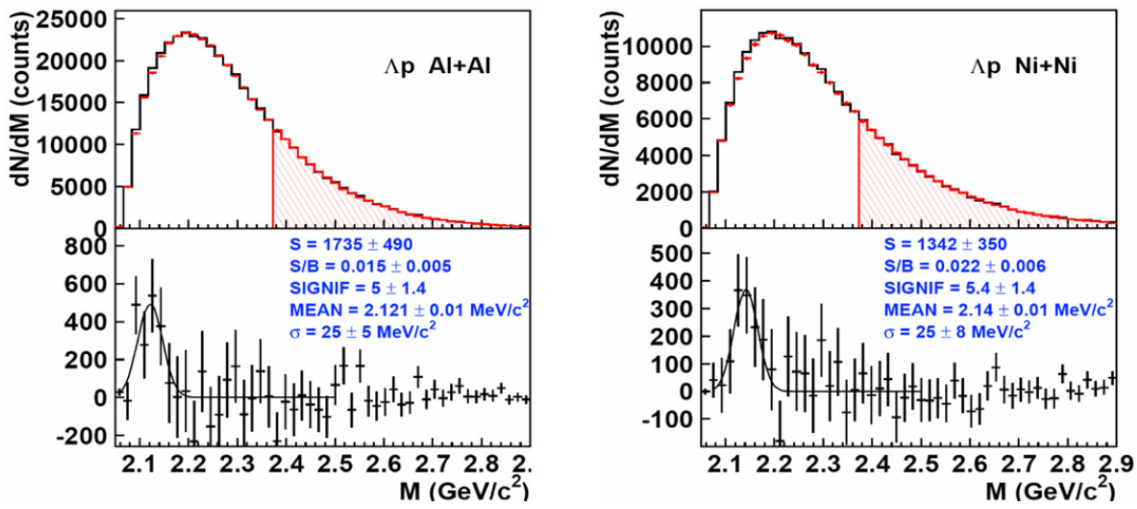

Figure 1.16: Invariant mass spectra of Λ-p pairs from Al+Al at 1.91A GeV (left) and Ni+Ni at 1.93A GeV (right), for detailed descriptions see the text. The figures are taken from [95].

1.3 Thesis objective

In order to explore the possible hypernuclei productions in HICs at SIS energies, we attempt to identify the light hypernuclei ${}^{3}_{\Lambda}$H and ${}^{4}_{\Lambda}$H via their two-body π^--decay channel, i.e. ${}^{3}_{\Lambda}\mathrm{H}\rightarrow\pi^- + {}^{3}\mathrm{He}$ and ${}^{4}_{\Lambda}\mathrm{H}\rightarrow\pi^- + {}^{4}\mathrm{He}$.

In the FOPI experiment, all of the decay products of the above reactions can be identified by a single or combined sub-detector(s). The CDC has a good transverse spatial resolution, which allows to constrain the quantities representing the distance measurements, for instance, the flight distance of the candidates, the transverse impact parameter of light charged particle and so on (for details see section 4.2), which can be used to suppress the background effectively.

The first goal of this work is to identify the ${}^{3}_{\Lambda}$H and ${}^{4}_{\Lambda}$H in Ni+Ni collisions at 1.91A GeV, by reconstructing their invariant masses and with the as large as possible statistical significances. Secondly, the yields, the phase space distribution and the lifetime are expected to be derived. Thirdly, by combining the yield of possible hypernuclei and the yield of hadrons like Λ, p, d, t, ^{3}He and ^{4}He, the possible hypernuclei production mechanism in HICs can be discussed. Finally, these results can be used to constrain the parameters in theoretical models, and contribute to the knowledge of YN interaction.

Chapter 2

The FOPI detector and the S325e experiment

2.1 Introduction

The FOPI detector, designed for fixed target experiments, is located at the 'Schwerionen-synchrotron' (SIS) of the 'Gesellschaft für Schwerionenforschung' (GSI) in Darmstadt, Germany. The FOPI detector covers a solid angle of almost 4π, as shown in Fig. 2.1. The charged particles (e.g. $\pi^{\pm}$, $K^{\pm}$, p, d, t,^{3}He and ^{4}He) produced in HICs can be identified. Since the complete information of charged particles from the collisions is measured, this makes the FOPI spectrometer an appropriate tool for investigating the properties of compressed nuclear matter formed by heavy-ion collisions at energies from 0.1A GeV to 2.0A GeV [100]. In the past twenty years, the FOPI spectrometer has been upgraded several times. A wide range of physics topics of HICs at SIS energies have been investigated, like the EOS [19], nuclear fragmentation [101, 102], meson production (pion, kaon and so on) [103, 104, 105] and the production of strange baryons (Λ, Σ) [106, 107] . In order to improve the particle identification (PID) capability for charged kaons, a new shell of Multi-strip Multi-gap Resistive-Plate Counter was added in 2008. This allows to study and verify the existence of the in-medium properties of charged kaons via the collective flow analyses.

In this chapter, the configuration and performance of the FOPI sub-detectors are described. The experimental conditions of the data sample relevant for this analysis are introduced at the end of this chapter.

2.2 The FOPI detector

The FOPI detector is composed of several azimuthally symmetrical sub-detectors. The central drift chamber (CDC) is located innermost of the FOPI detector. The CDC is surrounded by two Time-Of-Flight (TOF) detectors, i.e. the older plastic scintillator barrel (PLB) and the newly installed Multi-gap Multi-strip Resistive Plate Chamber

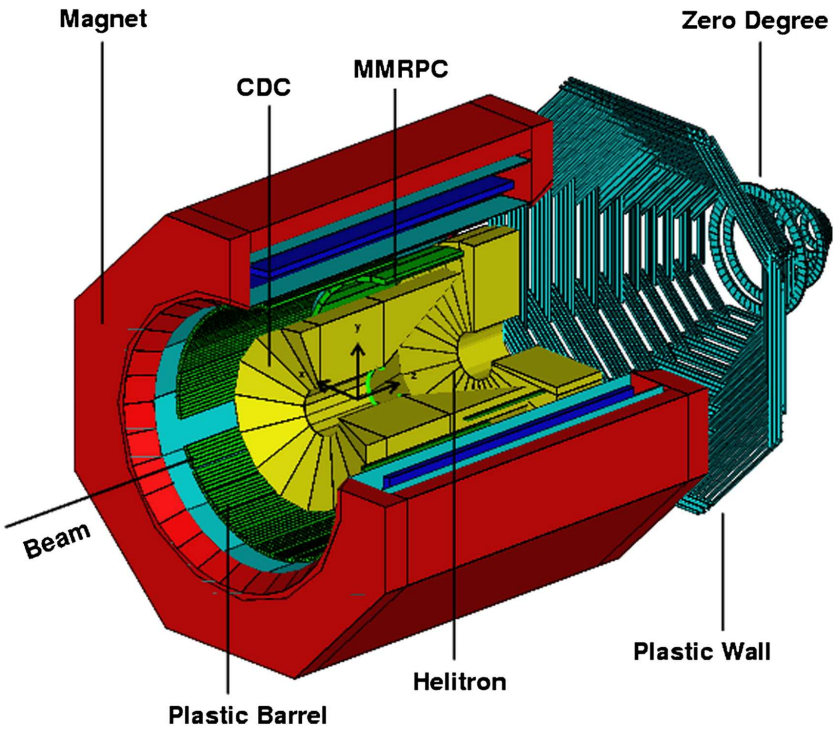

Figure 2.1: Schematic drawing of the FOPI detector.

(MMRPC, abbreviated as RPC). Another drift chamber called the HELITRON is located in front of the CDC. The CDC and the HELITRON are placed inside a super-conducting solenoid magnet. The plastic wall (PLW) and the zero degree detector (ZDD) are placed in front of the HELITRON. In the following subsections, the geometrical configuration and the performance of these sub-detectors are briefly described.

2.2.1 The magnet

The FOPI magnet is a superconducting solenoid magnet, which produces a homogeneous magnetic field parallel to the beam axis with a strength of 0.6 Tesla. The length and the diameter of the magnet are 3.3 m and 2.4 m, respectively. Two drift chambers (the CDC and the HELITRON) and the time-of-flight (TOF) detectors (the PLB and the RPC) are placed inside the magnet. The magnetic field is used to deflect the charged particles. The curvature of the helical trajectories in the transverse plane and the associated polar angle can be fitted from the hits recorded by the drift chambers. With the obtained curvature and polar angle, the momentum of the charged particles can be reconstructed.

2.2.2 The start counter and the veto detector

The start counter provides a time reference for all sub-detectors. In the S325e experiment (see section 2.3), the start detector was made out of poly-crystalline diamond, and was mounted in the vacuum of the beam pipe about 2 m in front of the target. The size of

the start detector was 2×2 cm^2 with an active area of 1 cm^2 and a thickness of 150 μm. The resolution of the start counter was $\sigma_t < 55$ ps [108].

In order to reject beam particles which were not focused on the target, two veto detectors, i.e. Halo 1 and Halo 2, were placed 200 cm and 10 cm in front of the target. The veto detectors were built by four scintillator bars and read out by the photomultipliers surrounding the beam pipe with a rectangular shape. The signals of Halo 1 and Halo 2 were put into an anti-coincidence with the one of the start counter.

2.2.3 The Central Drift Chamber (CDC)

The CDC is the main tracker of the FOPI detector and is responsible for the measurement of energy loss and the trajectory of the charged particles. The momenta of charged particles can be derived from the curvatures of the found arcs in the transverse plane and the associated polar angles fitted from the hits in the (r, z)-plane. The light charged particles can be identified by correlating the recorded energy losses by the CDC and the reconstructed momenta. In this sub-section, the geometrical configuration of the CDC and its observables are described.

Technical Details

The CDC is a jet-type drift chamber. This configuration was used by many experiments like JADE [109] and OPAL [110,111]. The CDC has conical end caps, the inner and outer radii are 0.2 m and 0.8 m from the beam axis, as shown in the left panel of Fig. 2.2. The polar angle acceptance of the CDC is in a range of 23^o to 113^o with respect to a new target position, which is shifted upstream by 40 cm with respect to the nominal target position. This aims to enlarge the acceptance of the CDC and the RPC barrel. The CDC covers the entire azimuthal angular range and is subdivided into 16 sectors in the transverse plane, shown in the right panel of Fig. 2.2. The sectors are delimited by the field wire planes, which are composed of 252 cathode wires each with 125 μm diameter spaced in 0.5 cm intervals. Each sector consists of 61 potential wires (with 125 μm diameter) and 60 sense wires (with 20 μm diameter) spaced 0.5 cm alternately. The sense, potential and cathode wires are parallel to the beam axis. In order to eliminate the mirror tracks, the cathode wire plane and sense wire plane are tilted by 8^o. Additionally, the sense wires are displaced alternately by 200 μm with respect to the anode plane (see the right panel of Fig. 2.2).

The drift voltage of -15 kV is distributed to the cathode wire via a voltage divider chain, which produces a homogeneous drift field of about 800 V/cm. The voltage applied on the potential wires is -1040 V. The sense wires are set to the ground potential. The operating gas of the CDC is a mixture of 88% Ar, 10% Isobutane, and 2% CH_4, which flows at one atmospheric pressure. The Isobutane and the CH_4 act as quenchers, which are used to absorb the feedback photons. Further details about the CDC are described in [100].

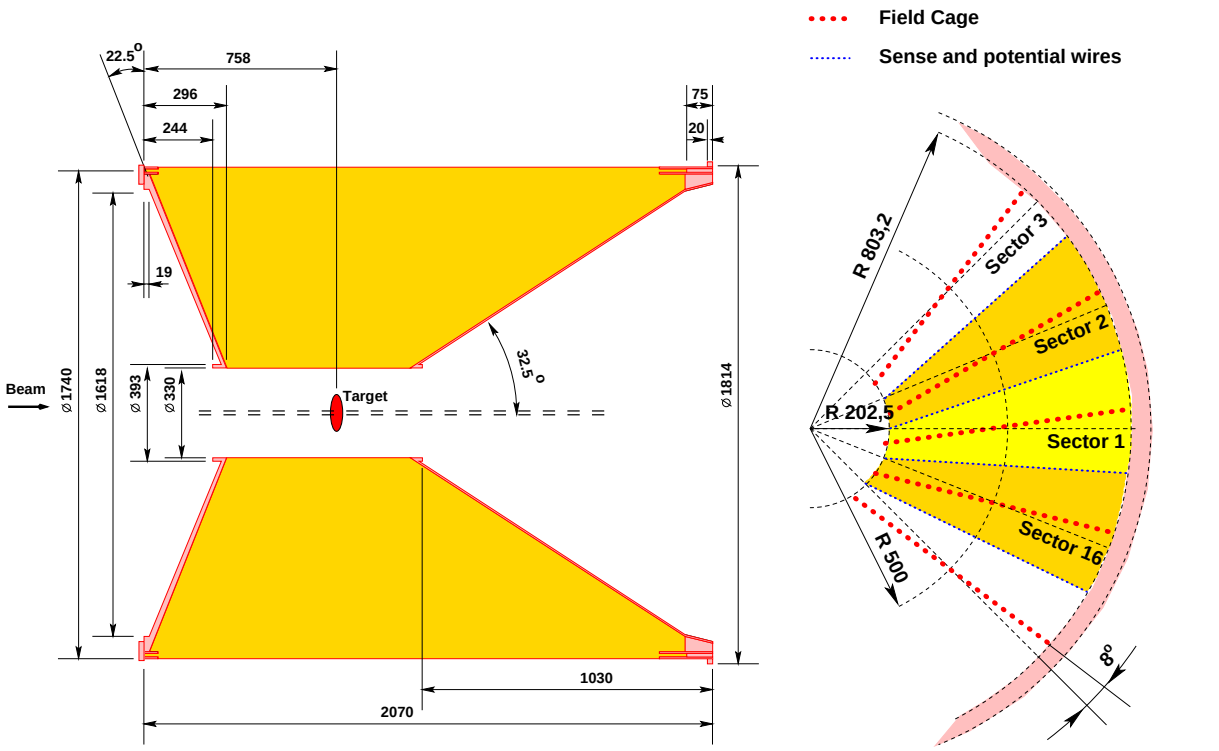

Figure 2.2: Longitudinal (left) and transversal (right) cross section drawings of the CDC. The target is shifted 40 cm upstream with respect to its nominal target position.

Observables measured by the CDC

The CDC is placed in a homogeneous magnetic field. When a charged particle passes through the CDC gas volume, it is bent by the field and leaves a helical trajectory in the space. The electron-ion pairs are created along the trajectory and they are separated by the electric field and drift to the sense wires and the field wires, respectively. The energy loss of a charged particle is described by the Bethe-Bloch formula (see appendix A). Due to the presence of the magnetic field perpendicular to the electric field, the accelerated electrons would be bent by the magnetic field. The electrons scatter on the atoms or the molecules of gas mixture and lose a part of their kinetic energy. Since the kinetic energy, gained by the electron between two successive collisions is not high enough to ionize the gas molecules, no additional electron is produced.

Finally, the drift path is no longer parallel to the electric field but has a tilt angle α_L, which is the so called Lorentz angle (illustrated in Fig. 2.3). An average drift velocity along the drift path is then acquired. For the CDC, the averaged drift velocity of the electrons is about 4.5 $cm/\mu m$. The average velocity of the ions is about 1000 times lower. The longest drift path in the drift cell is about 22 cm, which follows a maximum drift time of about 5 μs.

The strength of the electric field around the sense wires follows a $1/r$ behavior. When an electron is drifting close to the sense wire, this electron can accumulate enough energy to ionise atoms or molecules in a short distance. This process develops into an avalanche.

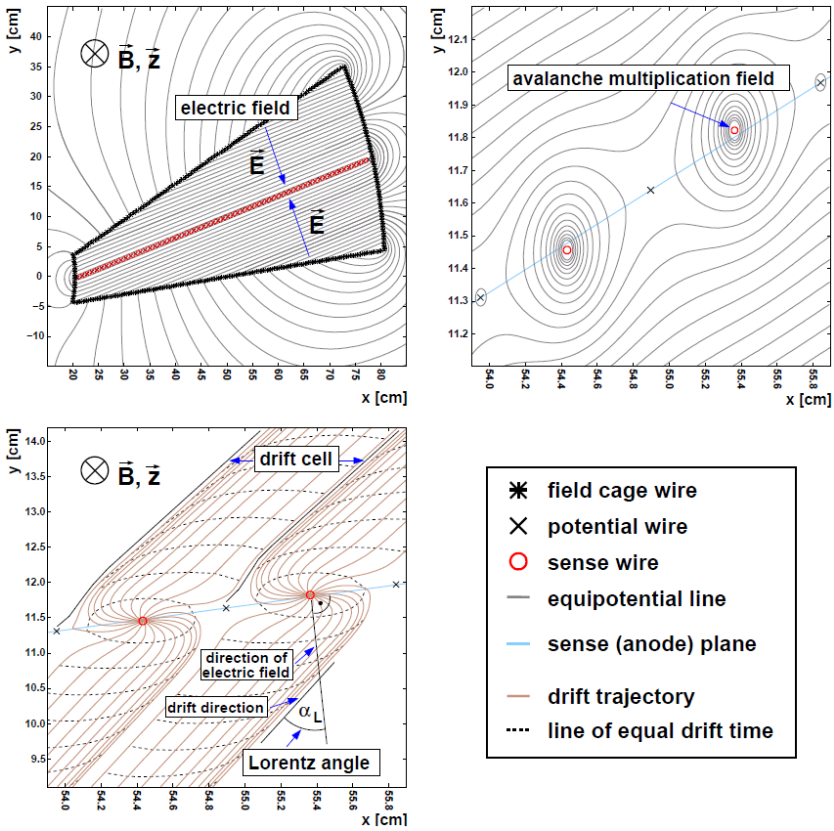

Figure 2.3: Illustration of the electric field (upper left), the avalanche multiplication field (upper right) and the drift trajectories of electrons (lower left) in a CDC sector. The figure is taken from [112] .

The charges which arrived initially are amplified about $10^3 - 10^4$ times. The amplified charges are picked up by the pre-amplifier at both ends of the sense wires. After the pre-amplifier, the signals are sampled by flash-ADC's (FADC) with a sampling frequency of 100 MHz.

In order to assign the hits in (x, y)-plane into the continuous arcs, the average drift velocity v_d, the Lorentz angle α_L and the time offset t_0 have to be calibrated. A detailed explanation can be found in [113]. The z-coordinate of the hits is reconstructed by the charge division method. The position resolution of hits is about 300 μm in the transverse plane and a few cm in the z-direction. After the calibration, the curvature ρ and the polar angle θ of the track are fitted by the track fitting procedures. Fig. 2.4 shows a typical event in Ni+Ni collisions at 1.91A GeV. The momentum of charged particles is derived from the following expressions,

$$p_t = 0.3 \cdot B \cdot \rho \cdot |z| \quad \text{(GeV/c)} \tag{2.1}$$

$$p = \frac{p_t}{\sin\theta} \quad \text{(GeV/c)} \tag{2.2}$$

where, B=0.6 T is the strength of magnetic field, ρ is the curvature of trajectory in the transverse plane and z is the charge number of the particle.

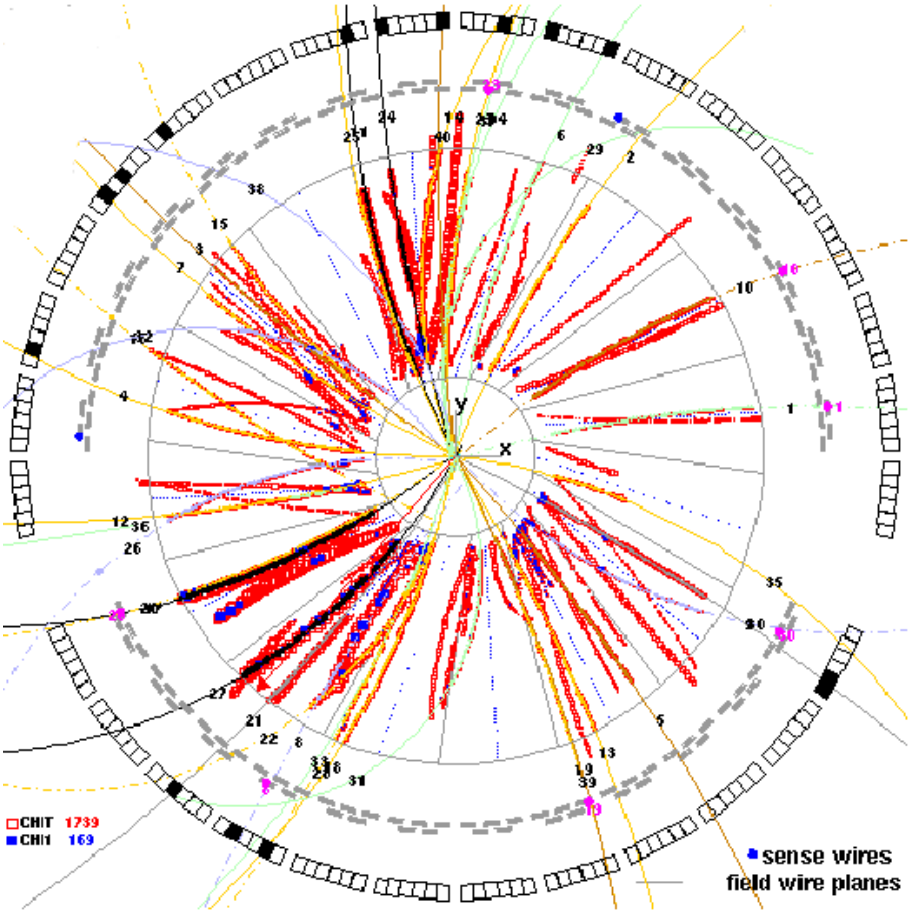

Figure 2.4: A typical event of Ni+Ni at 1.91A in the transverse plane. The inner part is the CDC. The RPC barrel is the layer outside of the CDC composed of 28 super modules. The outermost ring is the plastic barrel. The red points are the reconstructed hit positions in the CDC, the detected tracks are depicted by the solid arcs. The hits in the RPC and the PLB are labelled by the magenta circles and the filled squares, respectively.

2.2.4 The Plastic Barrel (PLB)

The plastic barrel is a time-of-flight (TOF) sub-detector, which measures the velocities of charged particles. The PLB is composed of 180 scintillator bars with a dimension of 150×4×3 cm^3, grouped in 30 modules with 6 bars each. The PLB surrounds the CDC, it covers about 80% of the full azimuthal angle and the polar angle from 54^o to 110^o. The scintillation light, produced by a charged particle, is read out by a photomultiplier (PMT) at both ends. At each end, the information of the arrival time t associated with a start time t_0 and the charge Q is recorded. The z-position of the hit z_{hit} and the flight time t_{tof} can be derived by following formulas,

$$t_{tof} = \frac{t_1 + t_2 - l/v_{propa}}{2}, \tag{2.3}$$

$$z_{hit} = \frac{t_1 - t_2}{c} \cdot v_{propa}, \tag{2.4}$$

where t_1 and t_2 are the measured arrival time of the upstream and downstream PMT with respect to t_0 respectively, $l(= 150\ cm)$ is the length of scintillator bars and v_{propa}(=16.5 cm/ns) is the propagation velocity of light inside the scintillator. Typical time resolution of the PLB is about 300 ps, corresponding to a position resolution of about 8 cm. The azimuthal angle resolution is about 2^o given by the dimension of the scintillator. The velocity of the charged particle can be derived from the following formula,

$$\beta = \frac{L}{t_{tof}} \tag{2.5}$$

where L is the total length of the helix in space and t_{tof} is the derived flight time. If two particles carry the same momentum with mass m_A and m_B, the difference of their flight time is calculated by the following expression [114],

$$\Delta t = |t_A - t_B| = \frac{L}{c} \left| \sqrt{1 + \left(\frac{m_A c}{p}\right)^2} - \sqrt{1 + \left(\frac{m_B c}{p}\right)^2} \right| \tag{2.6}$$

With the approximation $\sqrt{1 + (mc/p)^2} \approx 1 + (mc)^2/2p^2$, a separation power of the TOF detector can be defined as the following,

$$n_{\sigma_{TOF}} = \frac{|t_A - t_B|}{\sigma_{TOF}} = \frac{Lc}{2p^2 \sigma_{TOF}} |m_A^2 - m_B^2| \tag{2.7}$$

where σ_{TOF} is the time resolution of the TOF detector. In the high momenta range, particle misidentification would occur, as the difference of flight time becomes comparable to the time resolution of the detector.

2.2.5 The Multi-strip Multi-gap Resistive Plate Chamber (MMRPC) Barrel

The MMRPC barrel is another TOF sub-detector, abbreviated as RPC. Comparing to the existing scintillator barrel, the RPC has a superior time resolution and a higher granularity. The PID capability for charged kaons is improved significantly. This allows to study the in-medium properties of kaons and anti-kaons [97, 98] via their collective flow [115].

The MMRPC barrel contains 28 Super-Modules (SMs) (fully azimuthal coverage can accommodate 32 SMs, due to the existence of the CDC mechanical support, only 30 SMs can be mounted), which covers the polar angle from 30^o to 52^o. About 75% of the full azimuthal range is covered. 28 SMs surround the CDC with a radial distance of 94 cm to the beam axis. The single MMRPC counter is in a common double-stack configuration of 2×4 gaps with the anode in the center, the gaps are set by spacers of 220 μm diameter

fishing line. The stacks contain 1.1 mm and 0.55 mm thick window glass plates in an alternating array, as shown in the left panel of Fig. 2.5. Each SM is composed of 5 MMRPC counters, which share the same gas environment and high voltage. In order to cover the space in between the MMRPCs, the counters were arranged in a staggered configuration. A photo of a single super module with the readout electronics is shown in the right panel of Fig. 2.5.

The chambers operate with a gas mixture of 80% $C_2H_2F_4$, 15% SF_6 and 5% Iso-C_4H_{10}, which allows one to operate the counters at high fields without the problems related with streamers [116]. The HV is applied to the up and down copper foil. At moderate voltages of $U \leq 10$ kV, the strength of the electric field between the gaps reaches about $E \geq 100$ kV/cm. The readout electronics consist of the front-end electronics (FEE) followed by the Time-to-Amplitude Converter (TAC) based digitizer (TACQUILA). The FEE is an amplifier/discriminator card with high gain($\Delta G \sim 160$) at a high bandwidth($\delta f \sim 1.3$ GHz) and an excellent electronic time resolution ($\sigma_{FEE} \leq 18$ ps). The TACQUILA digitizer is operated in common stop mode with a free running 40 MHz clock as a stop signal. The total time resolution of the electronics is 25 ps. After the walk and wiggle (intrinsic non-linearity of the TAC chip) correction, the full-system resolution for the MMRPC barrel alone is $\sigma_{bar} \leq 70$ ps, including the time reference from our in-beam start counter, the total resolution is $\sigma_{Tof} \leq 90$ ps.

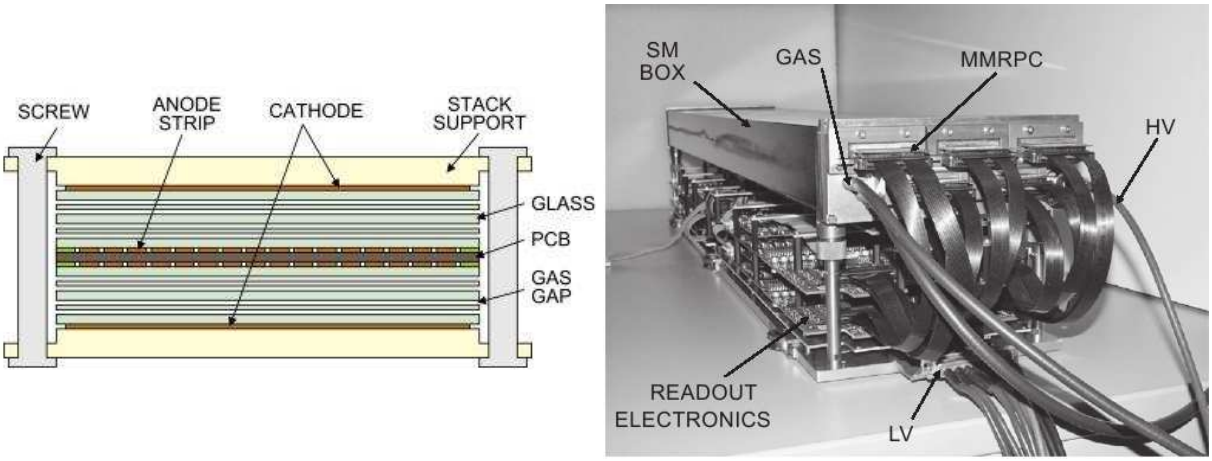

Figure 2.5: Cross-section view of an MMRPC counter (left), the read out electrodes sit in the middle of the counter and the glass layers are spaced by the fishing lines. A photo of a single super module with the readout electronics below (right). The figures are taken from [108].

2.2.6 The Plastic Wall (PLAWA)

The PLAWA covers the polar angle in a range of 7^o to 25^o, it is made of 512 plastic scintillator bars grouped into eight sectors. Each sector is composed of 64 strips. The scintillation light produced by a charged particle is read out by a photo multipliers at both ends. Like the PLB, each strip affords the two time parameters (t_L, t_R) and two

energy parameters (E_L, E_R). The time of flight and the hit position can be calculated from Eq. 2.3 and 2.4. The time resolution is linked to the active length of the scintillator strip, thus it varies from 80 ps for the innermost strips to 120 ps for the outermost strips. The corresponding position resolution varies from 1.2 cm to 2.0 cm along the strip.

2.2.7 The HELITRON

The HELITRON is a radial drift chamber which covers the full azimuthal angle and the polar angles from 10^o to 22^o. The HELITRON is subdivided into 24 sectors in the transverse plane. Each sector contains 54 sense and 53 potential wires, which extend radially from the inner radius to the outer radius of the chamber. When the charged particles pass through the chamber, the physics processes are same as these described in the case of the CDC. The HELITRON can provide information about the momenta and the energy losses of the charged particles. Typically, the chamber is operated with a gas mixture of 88% Argon, 10% Iso-C_4H_{10}, and 2% CH_4. The voltage applied on the drift wires is -12.5 kV and the voltage applied on the potential wires is -1600 V.

2.2.8 The Zero Degree Detector (ZDD)

The ZDD covers the polar angle from 1^o to 7^o, which contains 252 plastic scintillator strips grouped into 7 concentric rings. Each ring contains 36 trapezoidal shaped plastic scintillators. Every scintillator is read out by one photo-multiplier and delivers the energy loss and the time of flight information of charged particle. The time resolution of this detector is about 200 ps.

2.3 The S325 and S325e experiments

The experiments S325 and S325e were performed in September 2007 and in March 2008 respectively. According to the original experiment schedule, these two runs should be done in one time block. Due to a dysfunction of the accelerator, the experiment had to be separated into two parts. S325e means the extended part of the experiment S325. About 21.6×10^6 and 56×10^6 events were collected from the S325 and S325e experiments, respectively. The experimental results presented in the following chapters are from the data sample of the S325e experiment only.

2.3.1 The beam and target

A $^{58}_{28}$Ni beam at 1.91A GeV impinged on a 405 μm thick $^{58}_{28}$Ni enriched target (>95%) with a density of 360 mg/cm^2. In order to increase the geometrical acceptances of the CDC and the RPC, the target was shifted 40 cm upstream with respect to the nominal FOPI target position. The average beam intensity was about 3.5 $\times10^6$ ions/spill, the duration

time of a spill was about 10 s. Based on a sharp cut-off assumption, the interaction probability can be estimated by the following,

$$\begin{aligned} P_{rec} &= \rho \cdot d \cdot \frac{N_A}{A} \cdot \sigma_{tot} \\ &= \rho \cdot d \cdot \frac{N_A}{A} \cdot \pi r_0^2 (\sqrt[3]{A_p} + \sqrt[3]{A_t})^2 \\ &= 360\text{mg/cm}^2 \cdot \frac{6.022\times10^{23}/\text{mol}}{58\text{g/mol}} \cdot \pi (1.2\times2\times\sqrt[3]{58})^2 \\ &\approx 1\% \end{aligned} \tag{2.8}$$

where, ρ is the target density, $r_0(= 1.2$ fm) is an empirical constant to calculate the radius of the nucleus, N_A is Avogadro's constant, A is the mass number of the target and σ_{tot} is the geometrical cross section of reaction system.

2.3.2 The trigger

The trigger is the combined experiment conditions to mark the specific type of collisions. Typically, the fast detectors like the TOF detector are used to build the trigger conditions. In the FOPI experiment, the trigger conditions were built by combining the information from the start counter and the TOF detectors (PLB, RPC and PLW). In the S325e experiment, the bias trigger conditions were built by requiring the PLW hit multiplicity $PMUL\geq5$ and the PLB hit multiplicity $BMUL\geq1$. Under this trigger condition, most central collisions corresponding to the 60% of the total geometrical cross section were selected. The details are discussed in chapter 6 (section 6.4).

Chapter 3

Data analysis

The first step of the data analysis is to reconstruct the space location and the reaction geometry of the collision, which are characterized by the vertex and the reaction plane, respectively. The vertex and the reaction plane are the reference for the position and the azimuthal angle measurements. The locations of collisions are distributed in the area of the beam profile. The reaction geometry of the collisions is randomized in the azimuthal plane. These quantities can be reconstructed from the fitted tracks in each event. To identify the rare probes like ${}^{3}_{\Lambda}\mathrm{H}$ and ${}^{4}_{\Lambda}\mathrm{H}$ in HICs at SIS18 energies, the precision of the reconstruction vertex is crucial, because several key cuts used to suppress the background represent the measured lengths. The detailed selection and reconstruction method for identifying ${}^{3}_{\Lambda}\mathrm{H}$ and ${}^{4}_{\Lambda}\mathrm{H}$ from their two-body π^--decay channel is described in the next chapter.

In this chapter, the centrality of the S325e experiment is discussed first. Then the procedures for reconstructing the vertex and the reaction plane are described. In the following sections, the methods for identifying charged particles in the FOPI data are described. In the last part, the geometrical acceptance of the CDC and the TOF barrel is illustrated by the phase space distribution of π^- and ${}^{3}\mathrm{He}$, respectively.

3.1 Centrality selection

The impact parameter of a collision is the distance between the center of the two involved nuclei in the transverse plane. The centrality is a quantity inversely linked to the impact parameter. In collisions with a small impact parameter, more nucleons of the system are involved, and more products are expected. The number of emitted particles is called multiplicity, which is an experimentally measurable quantity. Due to the fluctuation of produced particles, the impact parameter can not be finely resolved. Therefore, experimentally, the centrality is characterized by the particle multiplicity instead of the impact parameter.

For the FOPI spectrometer, only the charged particles can be detected directly. In an event, the number of reconstructed tracks in the CDC is referred to as the track multi-

plicity $TMUL$. The number of registered hits in the PLW in one event is called $PMUL$. Fig. 3.1 depicts the distribution of the $TMUL$ (left) and the $PMUL$ (right) of the S325e experiment. For ${}^{3}_{\Lambda}\mathrm{H}$ and ${}^{4}_{\Lambda}\mathrm{H}$ reconstructions, the substantial constraints for $TMUL$ and $PMUL$ are introduced, which are described in the next chapter.

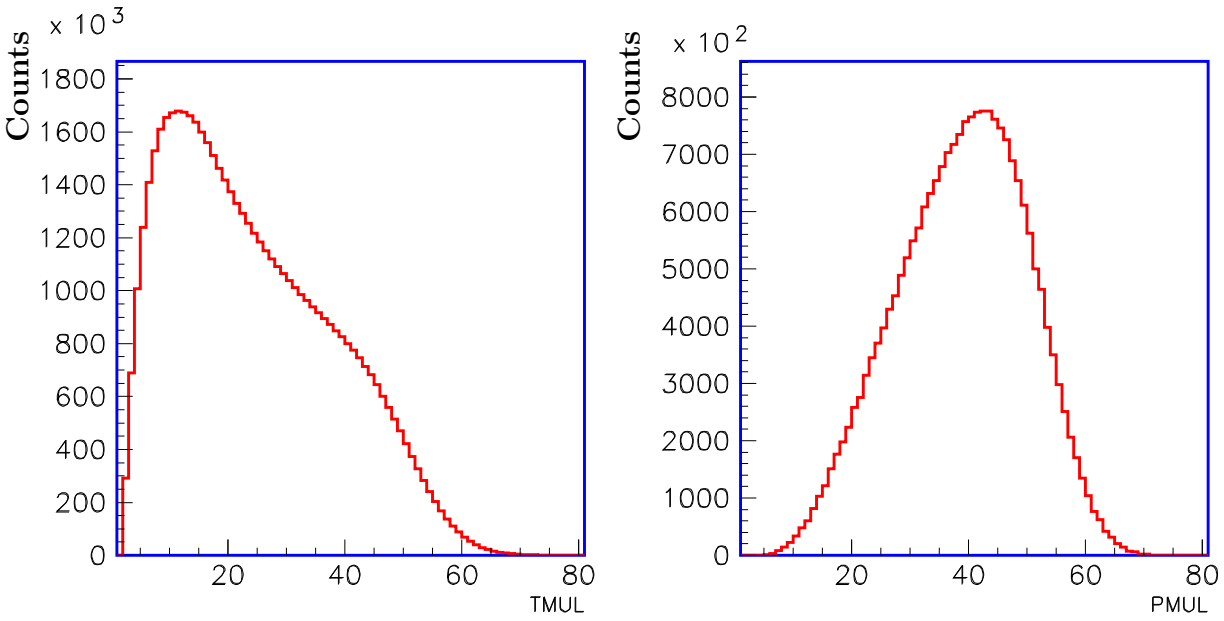

Figure 3.1: Distribution of the track multiplicity $TMUL$ (left) measured by the CDC and hit multiplicity $PMUL$ (right) measured by the PLW.

3.2 Vertex reconstruction

The primary vertex can be reconstructed by extrapolating the reconstructed tracks back to the target position or to the beam line. For the FOPI experiment data, each event only has one reaction location. The pile-up events are discarded by applying a cut on the charge information of the start counter. The detailed description of this step can be found in [112]. Imposing the constraints on the vertex, the off-target reactions can be discarded, they are the reactions of the beam particle with other material along the beam line, such as the start counter or gas molecules.

For the current analysis, the vertex is reconstructed by an iteration procedure. In the first interaction, the reconstruction is carried out in the FOPI detector frame with the origin at the target position. In the (x, y)-plane, the intersecting points of each two tracks are calculated. Since the primary vertex should be around the origin, the relevant points are those with the distance to the origin less than a transverse acceptance distance of 2.5 cm. The vertex coordinates in the transverse plane are the averaged coordinates of the accepted intersecting points. The standard deviation σ_t of the newly obtained vertex is calculated. In the (r, z)-plane, the intersect point between each track and the z-axis is calculated. The z-coordinate of the vertex is the averaged value of the intersecting distances in z-axis, while only the points with distance to the origin less than a longitudinal acceptance

distance of 4 cm are accepted. Similarly, a standard deviation σ_z of those points at the obtained z-coordinate is calculated. After this step, the beam profile can be reconstructed. The reconstructed beam profile of the S325e experiment in the transverse plane is shown in the left panel of Fig. 3.2, where O_x and O_y is the coordinate of the primary vertex in the x-axis and the y-axis, respectively. Afterward, the tracks are shifted into the frame with the origin at the newly obtained vertex coordinate. The characteristic parameters of each track, like transverse impact parameters d_0 (shortest distance from the fitted track to the primary vertex in the (x, y)-plane), intersecting distance in the z-axis z_0 and the coordinates of the circle's center in the transverse plane are recalculated.

In the next iteration, the whole procedure is repeated in the frame with the origin at the newly derived vertex. The transverse and longitudinal acceptance distance are updated to 1.5 times that of the obtained σ_t and σ_z, respectively. After several iterations, the vertex position in the (x, y)-plane and the (r, z)-plane can be localized. The coordinate distribution of the primary vertex in the y-axis under 1st-6th iteration is demonstrated in the right panel of Fig. 3.2. The iteration order is marked by a different color. The vertex distribution of the first iteration (red) is quite broad, as the width of the beam spot is included. After the second iteration, the reconstructed vertex coordinates show no significant change. The RMS of the reconstructed primary vertex is about few mm.

For the weakly decaying particles, like Λ hyperon and other single-Λ hypernuclei, the mean flight distance $\langle \beta\gamma c\tau \rangle$ (τ is the mean lifetime, c is the speed of light in vacuum) is in the order of a few centimeters when β is in order of $0.5c$. Therefore, the decay vertex of these particles can be well resolved from the primary vertex. The cuts on the distance between the secondary vertex and the primary vertex is an effective measure in suppressing the background particles coming from the primary vertex. For example, the transverse impact parameter of a track (see section 4.2.1) carries the information of its "birth history". If the impact parameter is a large value, it is highly probable that this particle originated from an off-vertex source, and vice versa. The longitudinal spatial resolution of the CDC is in the order of a few centimeters, thus the longitudinal impact parameter can not be used as a strong constraint. A detailed description of the selection criteria for Λ, ${}^{3}_{\Lambda}\mathrm{H}$ and ${}^{4}_{\Lambda}\mathrm{H}$ reconstruction is described in next chapter.

3.3 Reaction plane reconstruction

The reaction plane is spanned by the impact parameter ($\vec{b}$) and the beam direction, which can not be controlled experimentally and is randomly distributed over the azimuthal angle. The collective behavior of emitted particles in HICs can only be investigated with respect to the reaction plane of each event. The reaction plane can be reconstructed by the transverse momentum method proposed by Danielewicz and Odyniec [117]. Generally, a $\vec{Q}$ vector is constructed event by event by summing up the transverse momenta of the associated particles. The reaction plane is defined by the angle ϕ_R between the $\vec{Q}$ and

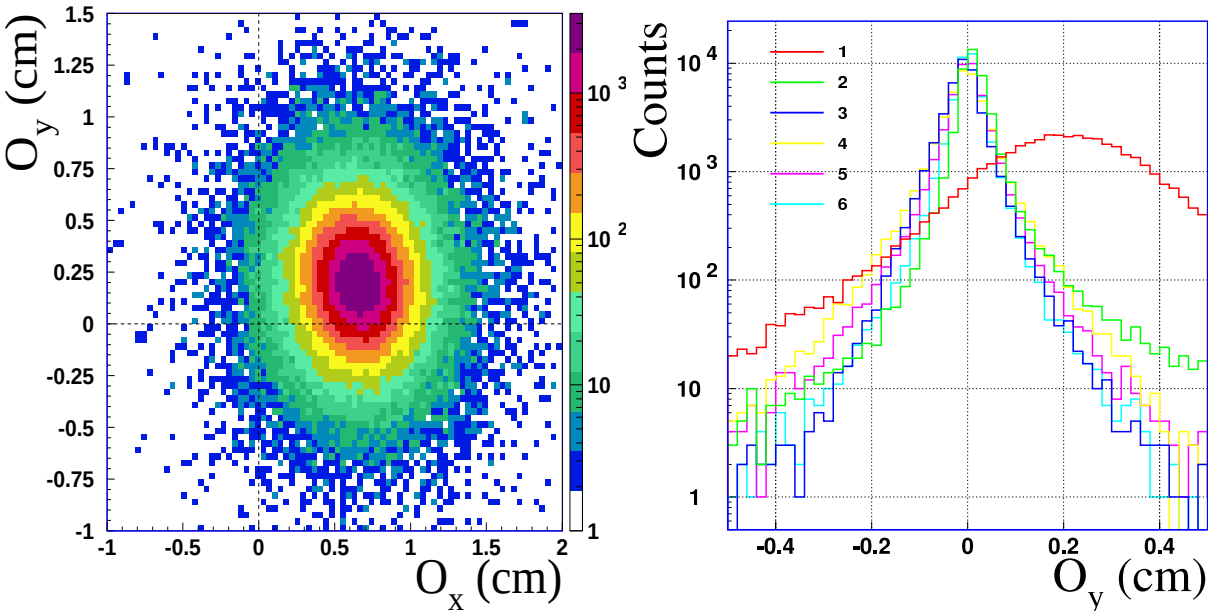

Figure 3.2: Reconstructed beam profile of the S325e experiment in the transverse plane (left). Vertex distributions in the y-axis (right) under the 1st-6th iteration.

the x-axis. The $\vec{Q}$ is calculated by,

$$\vec{Q} = \begin{pmatrix} Q\ \cos\phi_R \\ Q\ \sin\phi_R \end{pmatrix} = \sum_{k=1}^{N} \omega_k \cdot \vec{p}_k \tag{3.1}$$

where, ω_k is a weight factor and its value is defined by the following function,

$$\omega_k = \begin{cases} +1 & \text{for } y^0 > \Delta y \\ 0 & \text{for } |y^0| < \Delta y \\ -1 & \text{for } y^0 < -\Delta y \end{cases} \tag{3.2}$$

where y^0 is the scaled rapidity, defined by $(y_{lab} - y_{cm})/y_{cm}$, y_{cm} is the mid-rapidity in the laboratory frame. The particles located in region $-\Delta y < y^0 < \Delta y$ are excluded from the calculation, as they are not sensitive to the reaction plane. In this analysis, the Δy is set to be 0.3.

In the backward hemisphere of the collisions, covered by the CDC and the TOF barrels (RPC and PLB), only the baryons are used to calculate the reaction plane angle ϕ_R. The mesons which do not carry the information of the initial reaction geometry, like π, K, are excluded. In the forward hemisphere, all of the hits, recorded by the PLW, are taken into account. Fig. 3.3 shows the distribution of the reconstructed reaction plane angle ϕ_R. This distribution is not isotropic due to the fact that the detection efficiencies among the sectors of the CDC are not uniform. From the collective flow analysis, this effect has been investigated, and it turns out this effect would not impose a big influence on the final results, details thereof are presented in [115](p84).

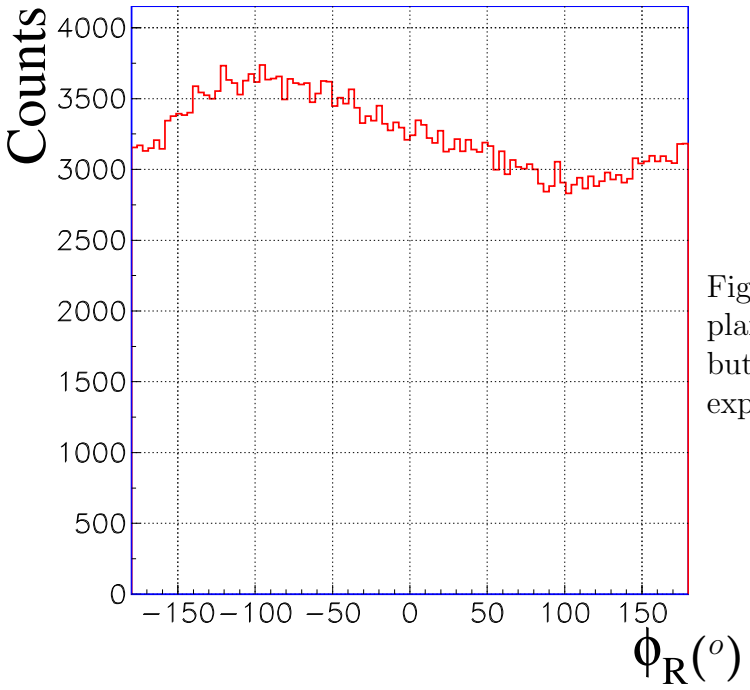

Figure 3.3: Reaction plane angle ϕ_R distribution of the S325e experiment.

Due to the high particle multiplicity in HICs, the candidates for the Λ hyperon and other single-Λ nuclei, can be formed by the uncorrected particles, which are called the combinatorial background. This background can be reproduced by a mixed event method (see section 4.2.3). Rotating each event into its reaction plane is necessary in order to obtain a mixed-event background spectrum, which can satisfactorily describe the shape of the combinatorial background. Ultimately, this background will be subtracted from the overall spectrum. The procedure for reconstructing the mixed event background is described in the next chapter.

3.4 Particle Identification (PID)

PID is one of the basic steps in data analysis. With the FOPI detector, the particles like $\pi^{\pm}$, $K^{\pm}$, p, d, t, ^{3}He and ^{4}He can be identified. The short-lived particles, like the ϕ meson, Λ hyperon, Σ hyperon etc., can be identified by reconstructing their invariant mass from the charged decay channel.

According to the Bethe-Bloch formula (see appendix A), the energy loss of a slow moving charged particle is proportional to $(z/\beta)^2$, where z is the charge number and β is the velocity. The total energy loss for charged particles inside the CDC is the sum of measured energy losses of all associated drift volumes. By correlating the total energy loss $\mathrm{d}E/\mathrm{d}x$ and the reconstructed momenta, the mass of the charged particles can be extracted. The left panel of Fig. 3.4 shows the correlation of $\log(\mathrm{d}E/\mathrm{d}x)$ and the charge number scaled momentum p/z. The different bands represent the different particle species. The solid lines are the parameterized Bethe-Bloch formula, i.e. the energy loss as a function of charge-scaled momentum. $|z| = 1$ particles, like $\pi^{\pm}$, p, d as well as t at high momenta,

are well separated from each other. However, for t, ^{3}He and ^{4}He identification, only the CDC information (m_{CDC}) is not sufficient any more, because the measured charge is not recorded properly, especially at the lower momentum region, due to the FADC being saturated by the huge signals. The mass spectrum extracted from this correlation is shown in the right panel of Fig. 3.4, the vertical lines indicate the nominal mass of $\pi^{\pm}$, p, d and t.

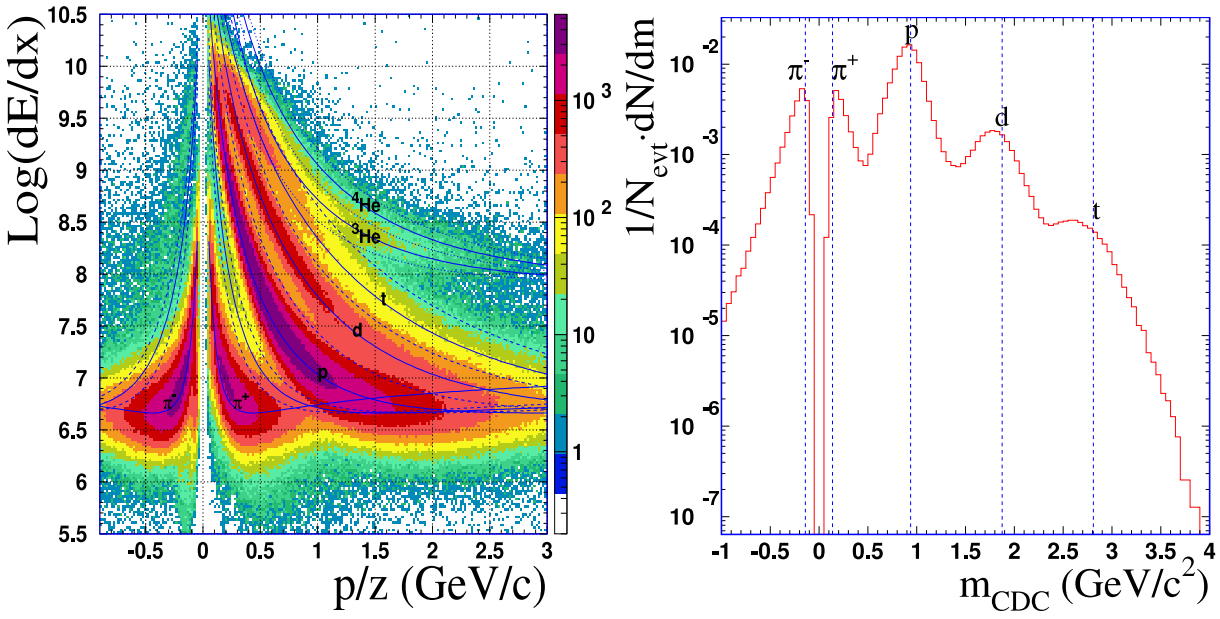

Figure 3.4: Correlation of $\log(dE/dx)$ and charge scaled momentum p/z (left). The curves are the parameterized Beta-Bloch formula for different particle species. Mass spectrum extracted from the left correlation (right), the vertical lines indicate the nominal mass of $\pi^{\pm}$, p, d and t.

The information of a particle's velocity can be derived from its flight time, measured by the TOF detectors. The hit(s) on the TOF barrel used to calculate the flight time is matched with the CDC track. By combining the velocities and the associated momenta, the mass of the particles can be uniquely determined by following formulas

$$p = mc^2 \cdot \beta \cdot \gamma, \quad \beta = v/c, \quad \gamma = \frac{1}{\sqrt{1-\beta^2}}, \tag{3.3}$$

where m is the mass of the charged particle, β is the normalized velocity, γ the Lorentz factor and c is the speed of light in vacuum. The correlation of charge number scaled momentum p/z and associated velocity is shown in Fig. 3.5. The different bands represent the different particle species. The solid lines are the first formula of Eq. 3.3 with different masses. The particles with the charge $|z| = 1$ are well separated from each other, the K^+ band is clearly visible due to the excellent time resolution of the RPC barrel. For charge $z = 2$ particles, ^{3}He band is located between the bands of p and d, the ^{4}He band overlaps with that of the deuteron. Therefore, in order to properly identify the charge $z = 2$ particles, the additional information of the charge is needed. The charge determination is presented in the next sub-section.

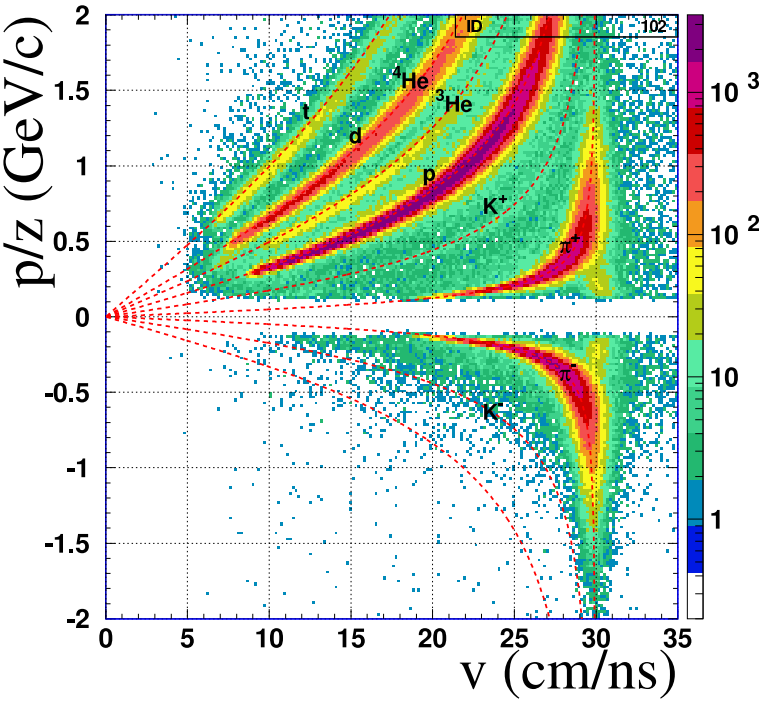

Figure 3.5: Correlation of the charge number scaled momentum, measured by the CDC, and the associated velocity, measured by the RPC. The curves are the momentum and velocity correlation assuming different particle masses.

3.5 Charge determination

The magnetic field is aligned with the beam direction. In the transverse plane, the positive particles are deflected in a clock-wise direction, the negative particles are bent in a counter-clock-wise direction. From the curling trend of the fitted arcs, the sign of their charge can be determined. For particles with low velocity, the energy loss in the medium is independent of the mass, but it is proportional to a z^2. With a given velocity, the energy loss of a $z = 2$ particle is about four times larger than the one of a $|Q| = 1$ particle.

The correlation of the energy loss measured by the CDC and the velocity measured by the RPC barrel after having applied PID selection cuts is shown in the left panel of Fig. 3.6. The lower band represents $|z| = 1$ particles, the upper band is for $|z| = 2$ particles. The profile of the lower band is fitted by a function with a form of $y = a{\cdot}x^{-1} + b{\cdot}x^{-2} + c{\cdot}x^{-3}$, where a, b and c are the fitting parameters. By comparing the energy loss with this fitting function at a given momentum, the charge number of particle can be determined. The determined charge number as a function of the RPC mass is shown in the right panel of Fig. 3.6. Clearly, all charged particle species are well separated.

3.6 Detector acceptance

The CDC is the only tracking detector used in this analysis, which covers the full azimuthal range and the polar angle from 23^o to 113^o. The light charged particles can be identified by the CDC alone, while for identifying the heavy charged particle like ^{3}He, ^{4}He, additional information from the velocity measurement by the TOF detector is required. The phase

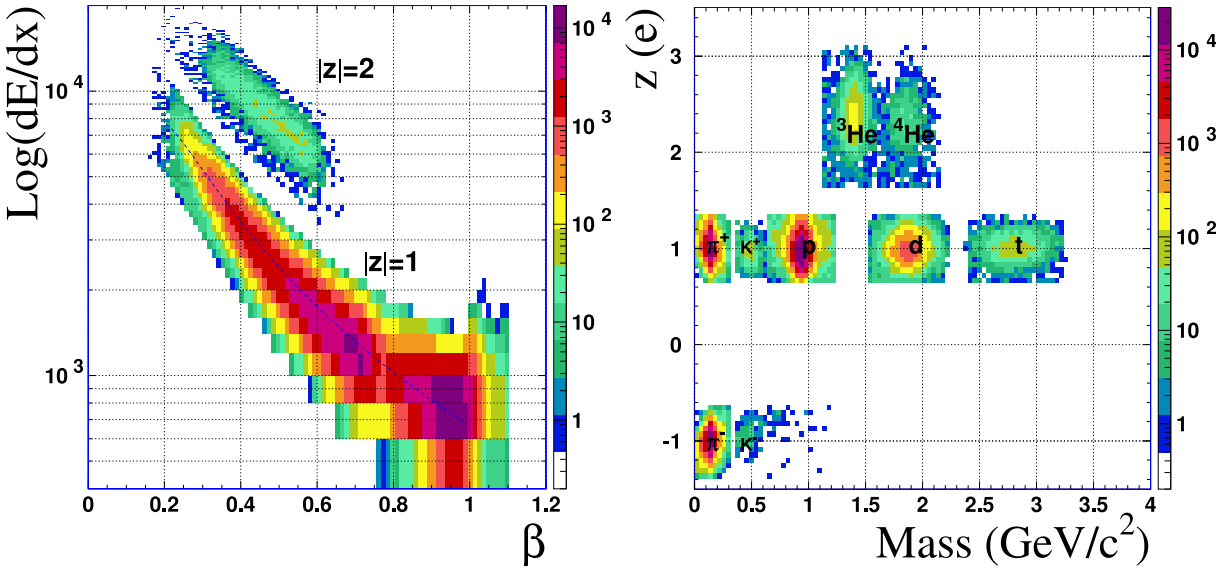

Figure 3.6: Correlation of log(dE/dx) measured by the CDC and associated velocity β measured by the RPC (left). The lower band is for $|z| = 1$ particles. Correlation of the determined charge and RPC mass (right), after having applied PID selection cuts.

space distribution of the π^- in Ni+Ni at 1.91A GeV is shown in the left panel of Fig. 3.7, which is displayed in the plane of mass scaled transverse momentum p_t/m and rapidity in laboratory frame y_{lab} (see Appendix B). The dashed curves are the polar angle acceptance of the CDC, the horizontal line is a transverse momentum cut at $p_{t,\pi^-}^{min} = 0.06$ MeV/c, which is used to exclude tracks spiralling inside the CDC. The phase space distribution of ^{3}He is shown in Fig. 3.7. The dashed-dotted lines show the polar angle acceptance of the RPC ($30^o < \theta < 52^o$) and the PLB ($54^o < \theta < 110^o$). The gap between the RPC and the PLB is also visible from this distribution. The mid-rapidity y_{AA} is at 0.89 and marked by a black arrow.

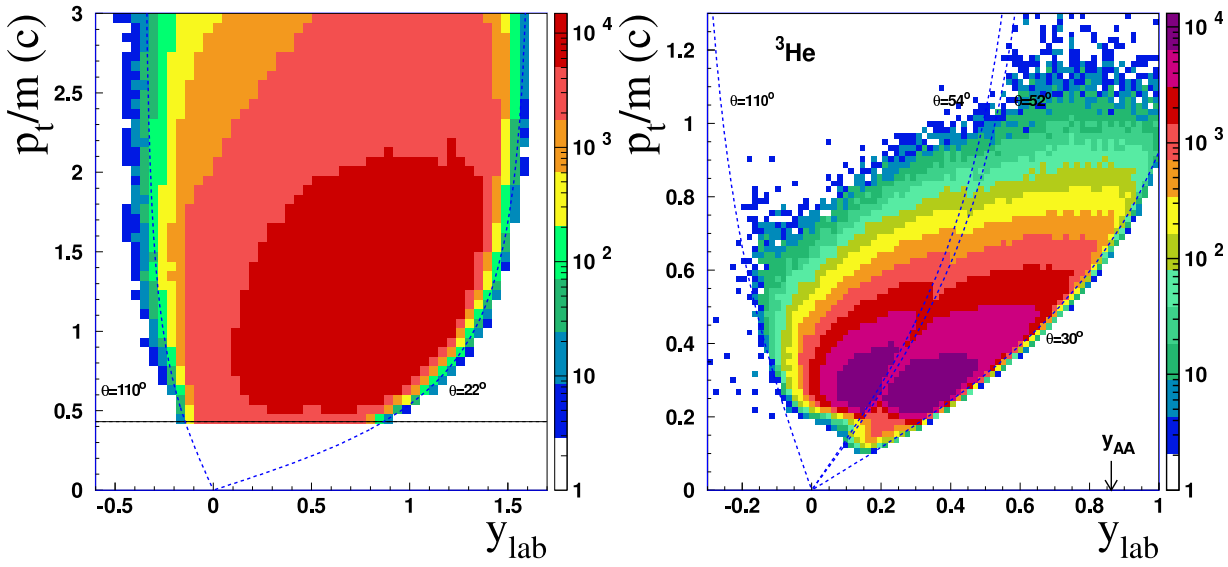

Figure 3.7: Phase space distribution of the π^- in the $p_t/m - y_{lab}$ plane (left). The dashed curves are the polar angle acceptance of the CDC ($22^o < \theta < 110^o$). The horizontal line is the minimum transverse momentum cut with $p_{t,\pi^-}^{min} = 0.06$ GeV/c. The phase space distribution of ^{3}He (right). The curves indicate the polar angle acceptance of the RPC ($30^o < \theta < 52^o$) and the PLB ($54^o < \theta < 110^o$). y_{AA} indicates the mid-rapidity of the collision.

Chapter 4

Particle reconstruction

The four-momenta of particles like $\pi^{\pm}$, $K^{\pm}$, p, d, t,^{3}He and ^{4}He can be directly measured by the FOPI detector. The short-lived particles, like Λ, Σ and so on, can be identified through their charged decay products. Due to the high particle multiplicity in HICs, a huge amount of randomly combined particles have similar features, such as the decay products of these short-lived particles. These kinds of particle pairs are referred to as the combinatorial background of a considered decay channel. In order to suppress the combinatorial background, a series of geometrical and kinematic selection conditions are designed according to the decay properties of the particles under consideration. Before extracting the physics results, the combinatorial background has to be eliminated.

In this chapter, the procedures for reconstructing the weakly decaying particles are described. A mixing event method, used to build the combinatorial background spectrum, is described. The procedures are demonstrated by reconstructing the Λ hyperon via its decay channel $\Lambda \rightarrow \pi^- + p$. Afterwards, the selection criteria for identifying ${}^3_{\Lambda}H$ and ${}^4_{\Lambda}H$ from their two-body π^--decay channel, and the obtained invariant mass spectra in various phase space regions are presented. The significance of the observed ${}^3_{\Lambda}H$ and ${}^4_{\Lambda}H$ signal is evaluated as well. In the last section, the detected yields of various particles in the concerned phase space regions are summarized.

4.1 Properties of ${}^3_{\Lambda}H$ and ${}^4_{\Lambda}H$

Identifying ${}^3_{\Lambda}H$ and ${}^4_{\Lambda}H$ via their two-body π^--decay channel is the first objective of this work. Before presenting the selection cuts, it is necessary to have a look at these properties of ${}^3_{\Lambda}H$ and ${}^4_{\Lambda}H$, as the selection cuts are tightly connected to the properties. The measurement status of the properties of ${}^3_{\Lambda}H$ and ${}^4_{\Lambda}H$ is compiled in table 4.1, where B_{Λ} is the binding energy between the Λ hyperon and the core nucleus, τ is the mean lifetime and η is the decay branching ratio of the two-body π^--decay among the total mesonic decay channels. The lifetime of ${}^3_{\Lambda}H$, ${}^4_{\Lambda}H$ and Λ is of the same order, corresponding to a mean flight distance $\langle \beta\gamma c\tau \rangle$ of a few centimeters when β is in order of 0.5c (c=3.0×10^8 m/s). The mass of the hypernuclei can be calculated according to Eq. 1.7, yielding

Table 4.1: Properties of ${}^{3}_{\Lambda}$H and ${}^{4}_{\Lambda}$H.

Particle	core	B_Λ (MeV)	τ (ps)	spin	η
${}^{3}_{\Lambda}$H	^{2}H	0.13±0.05 [21]	100-300 [70]	1/2 [118]	(0.3-0.41)±0.07 [119]
${}^{4}_{\Lambda}$H	^{3}H	2.08±0.08 [21, 120, 121, 122]	194^{+24}_{-26} [123]	0 [118]	0.69±0.02 [118]

$m_{{}^{3}_{\Lambda}\mathrm{H}}$ =2991.2±0.1 MeV/c^2 and $m_{{}^{4}_{\Lambda}\mathrm{H}}$ =3922.8±0.1 MeV/c^2.

4.2 Reconstruction method

First step of the reconstruction is to select the proper decay products. According to the properties of weakly decaying hypernuclei, the selected particle pairs have to fulfill geometrical and kinematic constraints. In this step, the selection criteria are called pre-selection cuts. These cuts are used to create a database, in which each event contains a particle pair fulfilling the selection conditions. This step aims to shorten the data scan time, since the size of the new database is significantly reduced compared to the one of the original data sample. Afterwards, the more restricted cuts are evaluated based on this new database.

In this section, the quantities used to select the decay products are presented first. In the second part, the geometrical constraints for decay products and candidates are described. In the third part, the mixed-event technique is introduced. In last part, the reconstruction procedure is demonstrated by reconstructing the invariant mass of the Λ hyperon via its decay channel $\Lambda \rightarrow \pi^- + \mathrm{p}$.

4.2.1 Particle selection

The PID methods have been presented in section 3.4. The identity of the particles is determined by the derived mass and charge. The trajectory of the charged particles in space is decomposed into the (x, y)-plane and the (r, z)-plane. In the transverse plane ((x, y)-plane), the quantities, i.e. curvature r_c, azimuthal angle ϕ, coordinate of the arc's center and transverse impact parameter d_0, are defined for the reconstructed arcs, as sketched in the left panel of Fig. 4.1. In the (r, z)-plane, the defined quantities are the intersecting distance along the z-axis z_0 and the polar angle θ, sketched in the right panel of Fig. 4.1. For a particle, leaving a hit in the TOF barrel, additional information from the TOF detectors is available. This can substantially improve the selection and reconstruction quality. In the following, the used quantities and their role for the single particle selection are described individually:

- CDC mass m_{CDC}, extracted from the correlation of energy loss and momentum (see Fig. 3.4) measured by the CDC. The charged particles, like $\pi^{\pm}$, p, and d are mainly constrained by this quantity.
- Barrel mass m_{bar}, derived from the momentum-velocity correlation (see Fig. 3.5).

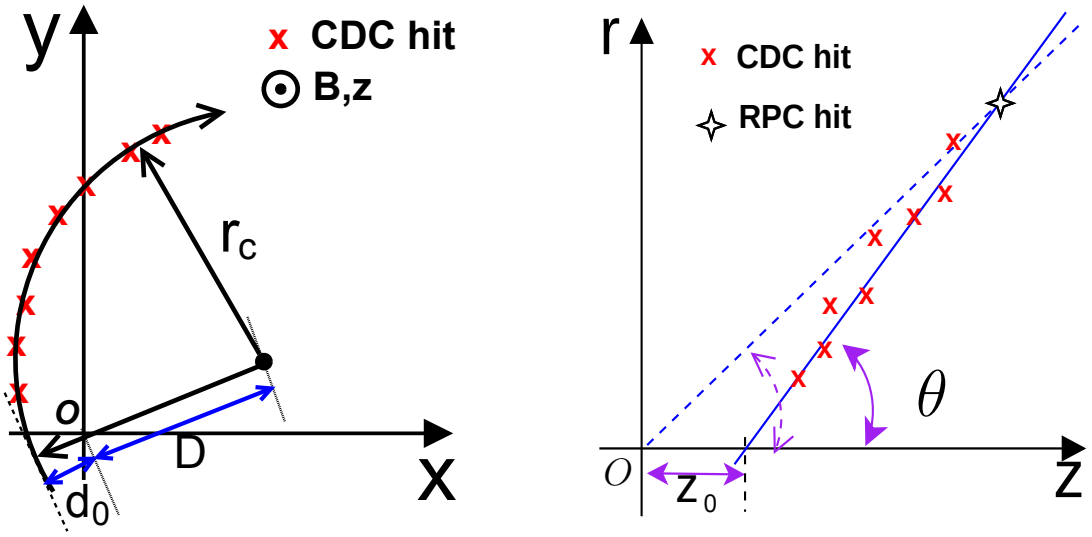

Figure 4.1: Schematic drawing of the track fitting in the transverse plane (left) and in the (r, z)-plane (right).

The heavy clusters like ^{3}He and ^{4}He are selected by m_{bar} combined with the determined charge information.

- The hit multiplicity $HMUL$, the number of fired CDC wires associated to a track. Typically, more hits means a longer lever arm, which would result in better fitting precision.

- Transverse impact parameter d_0, the shortest distance from the fitted track to the reconstructed primary vertex in the transverse plane (see left panel of Fig. 4.1). d_0 is calculated by $d_0 = r_c - D$, where r_c is the curvature of the arc and D is the distance from the center of the arc to the primary vertex. If d_0 has a large value, most probably this track is originated from an off-primary-vertex source, and vice versa.

- The intersecting distance of the track in the z-axis z_0, depicted in the right panel of Fig. 4.1. The resolution of z_0 is dominated by the spatial resolution of the CDC in the (r, z)-plane and the primary vertex resolution along the z-axis. Due to the spatial resolution of the CDC along the z-direction being in the order of a few cm (comparable to the mean flight distance of the hypernuclei), the quantity z_0 can not be used as an effective cut.

- The polar angle θ. For charge $|Q| = 1$ particles, the polar angle is fitted from the hits in the (r, z)-plane. For $Q = 2$ particles, due to the existence of the overflow effect in flash ADC (FADC), i.e. the amplitude of the signals (the charge information) above the upper limit of the FADC range were not recorded properly. This leads to an incorrect polar angle reconstruction. For the particles, leaving a hit in the TOF barrel, the polar angle can be recalculated from the hit in the TOF detector with respect to the primary vertex in the (r, z)-plane. As a comparison, the position

resolution of the RPC counter is given by $r_\sigma = v_{signal} \times \sigma_t = 16.5$ cm/ns$\times$80 ps $=$ 1.32 cm, where v_{signal} is the propagation velocity of the signal in the read-out strip of the RPC and σ_t is the time resolution of the RPC barrel. If one extrapolates this resolution to $r = r_s$, we have

$$\sigma_{z,r_s} = r_\sigma \times \frac{r_s}{r_{RPC}}, \tag{4.1}$$

where r_{RPC}=96 cm is the radius of the RPC barrel. At $r_s = 7.9$ cm (mean flight distance of the Λ hyperon), the corresponding position resolution is about 0.1 cm, which is far better than the spatial resolution of the CDC in the (r, z)-plane.

The pre-selection cuts for selecting the decay products of the Λ hyperon, ${}^{3}_{\Lambda}$H and ${}^{4}_{\Lambda}$H are listed in table 4.2. For the heavy clusters ^{3}He and ^{4}He, constraints on the RPC mass have to be introduced.

Table 4.2: Pre-selection cuts for the two-body π^--decay products of the Λ hyperon, ${}^{3}_{\Lambda}$H and ${}^{4}_{\Lambda}$H.

P	Dec.	$HMUL$ -	m_{CDC} [GeV/c^2]	m_{TOF} [GeV/c^2]	$\lvert d_0 \rvert$ [cm]	Q [e]
Λ	π^-	24	$0 < \cdots < 0.6$	—	$2 < \cdots < 20$	$\lvert Q+1 \rvert < 0.35$
	p	24	$0.54 < \cdots < 1.4$	—	$0.55 < \cdots < 20$	$\lvert Q-1 \rvert < 0.35$
${}^{3}_{\Lambda}$H	π^-	34	$0 < \cdots < 0.5$	—	$1 < \cdots < 20$	$\lvert Q+1 \rvert < 0.35$
	^{3}He	34	$1.7 < \cdots < 3.9$	$1 < \cdots < 1.8$	—	$Q > 1.5$
${}^{4}_{\Lambda}$H	π^-	34	$0 < \cdots < 0.5$	—	$1 < \cdots < 20$	$\lvert Q+1 \rvert < 0.35$
	^{4}He	34	$1.7 < \cdots < 4.7$	$2.1 < \cdots < 2.7$	—	$Q > 1.5$

4.2.2 Reconstruction topology

The decay products of the primary particle are emitted the spatial point, i.e. the secondary vertex. For the decay of ${}^{3}_{\Lambda}$H and ${}^{4}_{\Lambda}$H, the secondary vertex can be a few centimeters away from the primary vertex. As the primary vertex resolution in the transverse plane is in the order of a few mm, the secondary vertex can therefore be well resolved. Under the pre-selection cuts listed in table 4.2, the concerned particle pairs whose tracks intersect with each other, are sought in the transverse plane, and only those with the distance to the primary vertex larger than a certain value are taken into the next analysis step.

The search procedure is sketched in Fig. 4.2. The point $O(x_p, y_p)$ represents the primary vertex. The point $O_1(x_1, y_1)$ and $O_2(x_2, y_2)$ are the centers of the two tracks in the transverse plane, and r_1 and r_2 are their radii, respectively. P_1 and P_2 are their intersecting point. The distance D between the center of the two arcs is given by,

$$D = \sqrt{(x_1 - x_2)^2 + (y_1 - y_2)^2} \tag{4.2}$$

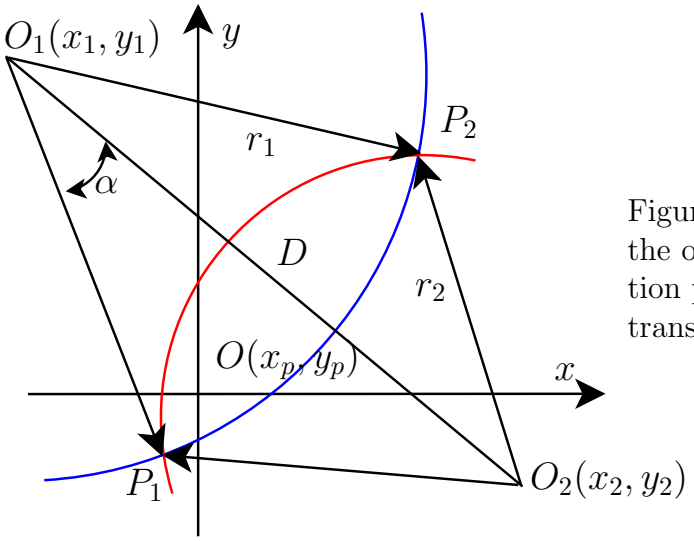

Figure 4.2: Schematic view of the obtainment of the intersection points of two tracks in the transverse plane.

If $D > r_1 + r_2$, means these two particles do not intersect with each other, those pairs are thus discarded. If $D \leq r_1 + r_2$, the coordinate of the intersecting points is calculated by

$$\begin{aligned} x_s &= x_1 + r_1 \cdot \cos(\pm\alpha) \\ y_s &= y_1 + r_1 \cdot \sin(\pm\alpha) \end{aligned} \tag{4.3}$$

where α is the angle defined by the line(O_1, O_2) and the line $(O_1, P1)$(see Fig. 4.2), which is calculated by

$$\alpha = \cos^{-1}\left(\frac{r_1^2 + D^2 - r_2^2}{2 \cdot r_1 \cdot D}\right). \tag{4.4}$$

At each intersecting point, several geometric and kinematic quantities are defined. These quantities are described in the following:

- r_s and ϕ_s, the distance from the intersecting point to the primary vertex in the transverse plane, and the azimuthal angle defined by the intersecting point and the primary vertex, calculated by

$$r_s = \sqrt{(x_p - x_s)^2 + (y_p - y_s)^2} \quad \text{and} \quad \phi_s = \tan^{-1}\left(\frac{y_p - y_s}{x_p - x_s}\right). \tag{4.5}$$

  In order to suppress the combinatorial background, a lower and an upper limit for r_s are introduced.

- Δz, the difference of the z-coordinate of particle 1 and particle 2 at $r = r_s$ in the (r, z)-plane (see the left panel of Fig. 4.3), defined by $\Delta z = z_1 - z_2$, which qualifies how far apart two tracks are from each other at $r = r_s$ in the (r, z)-plane.

- $p_{t,Hyp}$ and ϕ_{Hyp}, the transverse momentum of the hypernucleus candidate and its azimuthal angle, calculated by

$$p_{t,Hyp} = \vec{p}_{t,1} + \vec{p}_{t,2}, \qquad \phi_{Hyp} = \tan^{-1}\left(\frac{p_{y,1} + p_{y,2}}{p_{x,1} + p_{x,2}}\right), \tag{4.6}$$

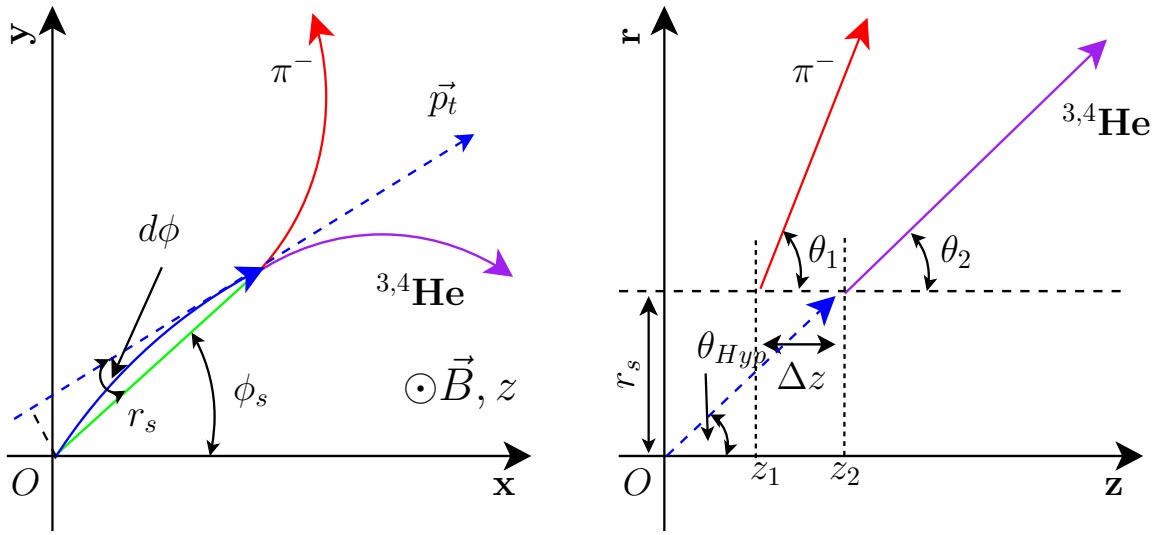

Figure 4.3: Schematic view of the reconstruction of the weakly two-body π^--decay particles in the (x, y) (left) and (r, z)-planes (right). The cut quantities used to constrain the particle pairs are illustrated. For detailed descriptions see the text.

where $\vec{p}_{t,1} = (p_{x,1}, p_{y,1})$ and $\vec{p}_{t,2} = (p_{x,2}, p_{y,2})$ are the transverse momentum vectors of the two involved particles at the intersecting point (see the left panel of Fig. 4.3).

- $p_{z,Hyp}$, the longitudinal momentum of the hypernucleus candidate, defined by $p_{z,Hyp} = p_{z,1} + p_{z,2}$, where $p_{z,1}, p_{z,2}$ are the longitudinal momenta of the decay products.

- dϕ, defined by d$\phi = \phi_{Hyp} - \phi_s$, which quantifies how well the momentum vector of candidate points to the primary vertex.

- θ_{Hyp} and z_s, the polar angle and the z-coordinate of the secondary vertex. For $\Lambda \to \pi^- + $p reconstruction, since the polar angles of decay products are measured by the CDC, these two quantities are calculated by the following expressions

$$\theta_{Hyp} = \tan^{-1}\left(\frac{p_{t,c}}{p_{z,c}}\right), \quad z_s = \frac{\sigma_1 \cdot z_{s1} + \sigma_2 \cdot z_{s2}}{z_{s1} + z_{s2}}, \tag{4.7}$$

where σ_1 and σ_2 are the fitting variance of track 1 and track 2 in the (r, z)-plane. For two-body π^--decay of ${}^3_\Lambda$H and ${}^4_\Lambda$H, the polar angle of π^- is measured by the CDC, but the polar angle of ^{3}He/^{4}He can not be directly calculated from the associated hit on the RPC with respect to the primary vertex, because the ^{3}He/^{4}He that decays from ${}^3_\Lambda$H/${}^4_\Lambda$H does not originate from the primary vertex. Since the mass difference of the two-body π^--decay products of ${}^3_\Lambda$H/${}^4_\Lambda$H is rather large ($m_{\pi^-}/m_{^3\mathrm{He}} \sim 5\%$), the momentum of ${}^3_\Lambda$H or ${}^4_\Lambda$H is mostly carried by the heavier decay product. Therefore, the polar angle of ^{3}He and ^{4}He calculated from the hit on the RPC barrel with respect to the primary vertex is a good approximation. In this case, the polar angle of ^{3}He/^{4}He can be approximately considered to be the polar angle of ${}^3_\Lambda$H/${}^4_\Lambda$H, i.e.

$$\theta_{Hyp} = \theta_{^{3,4}\mathrm{He}}, \quad z_s = r_s \cdot \cot\theta_{Hyp}. \tag{4.8}$$

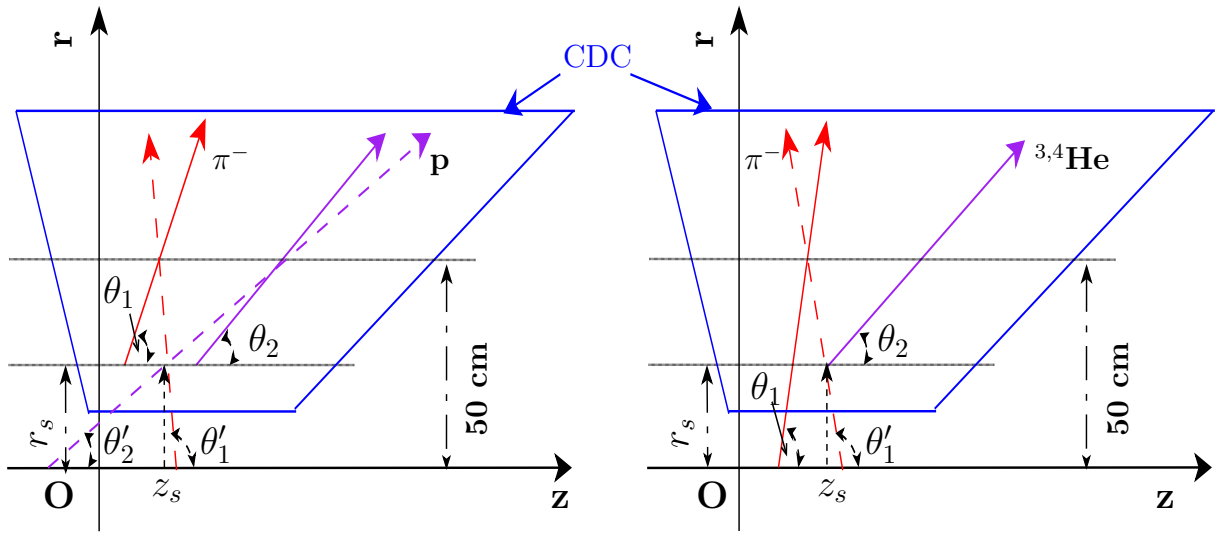

Figure 4.4: Schematic view of the track refitting procedure for Λ reconstruction (left) and ${}^{3,4}_{\Lambda}$H reconstruction (right). The blue arrows indicate the longitudinal profile of the CDC. The solid arrows denote the free-fit tracks and the dashed lines indicate the refitted tracks. For detailed description see the text.

The validity of this polar angle approximation is cross-checked in chapter 6.

- m_{inv}, the invariant mass of the particle pair, calculated by the following formula,

$$m_{inv}c^2 = \sqrt{E_{tot}^2 - (\overrightarrow{p}_{tot}c)^2} = \sqrt{(E_1+E_2)^2 - (\overrightarrow{p}_1 c + \overrightarrow{p}_2 c)^2} \tag{4.9}$$

  where $(E_1, \overrightarrow{p}_1 c)$, $(E_2, \overrightarrow{p}_2 c)$ are the four momenta of the two "daughter" particles.

- y_{Hyp}, the rapidity of the hypernucleus candidate in the laboratory frame (see Appendix B).

For Λ reconstruction, in the (r, z)-plane the polar angle of the involved particles is refitted by using the coordinate of the secondary vertex (r_s, z_s) and another point at $r = 50$ cm on the old track, sketched in the left panel of Fig. 4.4. The polar angles of the "daughter" particles can be recalculated, and their momenta in the z-direction are recalculated as well, e.g. $p_z = p_t \cdot \tan(\theta)$. After refitting the polar anlges, the width of the reconstructed Λ hyperon invariant mass is improved [112]. For ${}^{3}_{\Lambda}$H and ${}^{4}_{\Lambda}$H reconstruction, since z_s is calculated from the track of ^{3}He and ^{4}He, only the polar angle of π^- is refitted. This is sketched in the right panel of Fig. 4.4.

In order to discard the pairs which are not likely to be the decay products of a primary particle, the pre-selection cuts for a few quantities of candidates are introduced. The pre-selection cuts for the candidate selections of the Λ hyperon, ${}^{3}_{\Lambda}$H and ${}^{4}_{\Lambda}$H are listed in table 4.3.

Table 4.3: Pre-selection cuts for the candidates of the Λ hyperon, ${}^{3}_{\Lambda}$H and ${}^{4}_{\Lambda}$H.

P	r_s [cm]	Δz [cm]	$d\phi$ [^{o}]
Λ	$2. < \cdots < 30$	$-28 < \cdots < 28$	$-10 < \cdots < 10$
${}^{3}_{\Lambda}$H	$1. < \cdots < 30$	$-38 < \cdots < 38$	$-10 < \cdots < 10$
${}^{4}_{\Lambda}$H	$1. < \cdots < 30$	$-38 < \cdots < 38$	$-10 < \cdots < 10$

4.2.3 Combinatorial background

Due to the high particle multiplicity in HICs, not all of the selected pairs are the real decay products of the primary particle. Before extracting the physics results, the contributions from the combinatorial background have to be eliminated.

The combinatorial background is composed by the uncorrelated particles, which fulfil the geometric and kinematic constraints. Via transplantation of one particle (π^- in this work) of the selected pairs to another similar event, the results of random combination would be the same. This kind of method is called the mixed-event method [124, 125]. Since the particle pairs, found under such an operation, are taken from the different events, the possible correlation is destroyed explicitly. In order to ensure that the random combination probability is at a similar level, the events used for mixing are belonged the same $PMUL$ class ($PMUL$ distribution, i.e. Fig 3.1(b), is sorted into five classes). One thing that should be mentioned is that the tracks of an event are rotated into its particular reaction plane before the mixing, which keeps the angular correlation between the single particle and the reaction plane. This step is necessary to obtain a proper mixed-event spectrum, which can describe the shape of the combinatorial background.

In the analysis, the centrality class is defined by the PLW hit multiplicity. The events belonging to the same class are stored in a database. In order to increase the statistics of mixed-events, each event in the database is used 20 times. Finally, the number of mixed events is about 20 times more than the one of combinatorial background. Therefore, the number of mixed events has to be downscaled to a proper level of the combinatorial background. This step is demonstrated in the following sections in more detail.

4.3 Λ reconstruction

Λ hyperons are abundantly produced in HICs at SIS18 energies. The Λ reconstruction is of great importance for investigating ${}^{3}_{\Lambda}$H and ${}^{4}_{\Lambda}$H production: (a) as the decay kinematics of $\Lambda \rightarrow \pi^- + \mathrm{p}$ is quite similar to the two-body π^--decay of ${}^{3}_{\Lambda}$H and ${}^{4}_{\Lambda}$H, reconstructing the Λ hyperon is a good reference to understand the detector behavior and the reconstruction method; (b) the lifetime of the Λ hyperon is well measured, which can be used as a benchmark to verify the consistency between the experimental data and the MC simulation; (c) as discussed in chapter 1, hypernuclei can be produced by the Λ hyperon induced reaction in HICs. Therefore, it is necessary to reconstruct the Λ hyperons first.

In this section, the selection criteria for reconstructing the Λ hyperon via its two-body π^- decay are described first, then the invariant mass of the Λ hyperon is reconstructed.

4.3.1 Selection criteria

As with the procedures described in the previous sections, all of the geometrically correlated (π^-,p) pairs are sought in each real and mixed event by applying the pre-selection cuts. Then the more restricted selection criteria are applied to the candidates for the Λ hyperon. The cut quantities and their constraints for π^-, p, and Λ hyperon candidacy are listed in table 4.4.

Table 4.4: Selection cuts for π^-, p and candidates of the Λ hyperon.

Particle	quantity	unit	cut	meaning
π^-	$\|d_0\|$	cm	1.5< $\cdots$ <20	transverse impact parameter
	m_{CDC}	GeV/c^2	0.05< $\cdots$ <0.7	CDC mass
	HMUL	-	> 24	hit multiplicity
	Q	e	-1.5< $\cdots$ <-0.5	charge
	p_t	GeV/c	> 0.05	transverse momentum
p	$\|d_0\|$	cm	0.55< $\cdots$ <20	transverse impact parameter
	m_{CDC}	GeV/c^2	0.7< $\cdots$ <1.5	CDC mass
	HMUL	-	> 24	hit multiplicity
	Q	e	0.5< $\cdots$ <1.5	charge
	p_t	GeV/c	> 0.1	transverse momentum
Λ	r_s	cm	3< $\cdots$ <30	dis. of V1,2 in the (x, y)-plane
	$\|d\phi\|$	[^{o}]	< 10	$\phi_{Hyp} - \phi_s$
	$\|d_0\|$	cm	< 0.5	transverse impact parameter
	Δz	cm	<70.	$\|z_1 - z_2\|$
	p_t	GeV/c	> 0.2	transverse momentum
	m_{inv}	GeV/c	< 1.27	maximum invariant mass

4.3.2 Λ invariant mass reconstruction

Applying the selection cuts listed in table 4.4, the invariant mass of selected (π^-,p) pairs is calculated according to Eq. 4.9. In Fig. 4.5(a), the invariant mass spectrum of the Λ candidates is depicted, a clear peak is visible on top of a continuous background spectrum. The invariant mass spectrum of (π^-,p) pairs from the mixed events is shown in Fig. 4.5(b). Since all of the combined π^- and p are from different events, no peak is present. Because each event is used 20 times, the mixed-event invariant mass spectrum has to be normalized to the one of Λ hyperon candidate in the non-signal region. The normalization (downscale) factor is a ratio of the integrated counts in the signal spectrum and the one in the mixed-event spectrum in the same normalization region(s). For Λ reconstruction, the normalization regions are shown by the hatched areas in both upper panels. The

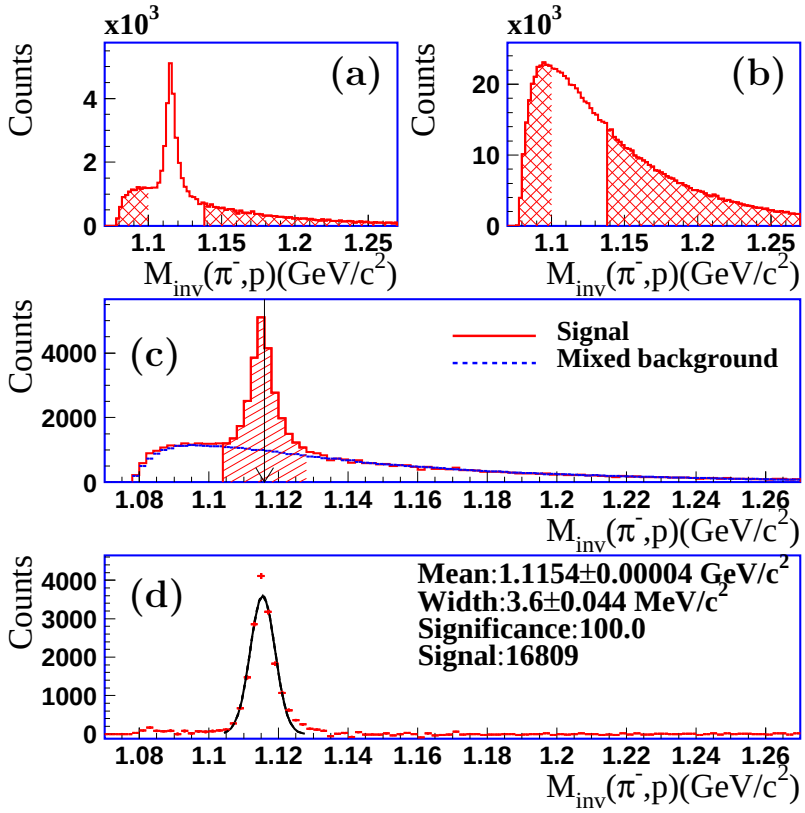

Figure 4.5: (a) Invariant mass distribution of correlated (π^-,p) pairs. (b) Invariant mass distribution of (π^-,p) pairs from mixed-events, the hatched regions are the chosen normalization regions. (c) Superposition of the signal spectrum (solid red line) and the normalized background spectrum (dashed blue curve). (d) Invariant mass spectrum after subtracting the background, the peak is fitted by a Gaussian distribution.

invariant mass spectrum of the Λ candidates (solid red line) and the normalized mixed-event background spectrum (dashed blue curve) are shown in Fig. 4.5(c). Fig. 4.5(d) is the invariant mass spectrum after subtracting the background spectrum. A clear peak is present around the nominal mass of the Λ hyperon, while the remaining counts in other parts of the spectrum are almost zero. This implies that the mixed-event method works reasonably well. The peak is fitted by a Gaussian function, with a mean and a width of 1.1154 GeV/c^2 and 3.6 MeV/c^2, respectively. The obtained Λ mass is in a good agreement with the PDG value.

4.4 $^{3}_{\Lambda}$H reconstruction

The procedure for finding the $^{3}_{\Lambda}$H candidate from its two-body π^--decay channel, i.e. $^{3}_{\Lambda}\mathrm{H}\rightarrow\pi^- +^3$ He, is the same as the one of the Λ hyperon reconstruction described in last section. $^{3}_{\Lambda}$H and $^{4}_{\Lambda}$H are very rare probes, in order to find a significant signal from a huge combinatorial background, more stringent selection cuts are necessary. The π^- populate the full geometrical acceptance of the CDC, while the phase space of the heavier decay product ^{3}He, is much more limited. The detectable phase space of $^{3}_{\Lambda}$H is constrained by the one of its heavier decaying product ^{3}He, thus before going into any details of the $^{3}_{\Lambda}$H reconstruction, it is instructive to inspect the phase space distribution of ^{3}He.

In this section, the phase space distribution of ^{3}He is discussed first. Then the selection criteria for $^{3}_{\Lambda}$H reconstruction are described. Afterwards, the invariant mass spectrum of

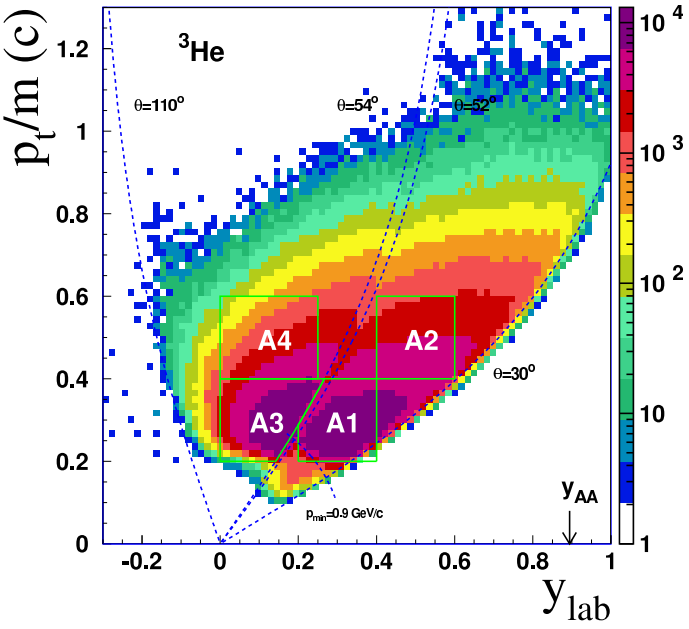

Figure 4.6: ^{3}He phase space distribution from the S325e experiment in the plane of $p_t/m - y_{lab}$. y_{AA} indicates the mid-rapidity of Ni+Ni collision at 1.91A GeV.

${}^{3}_{\Lambda}$H and the mixed-event background spectrum are presented. In last part, the significance of the obtained signal is evaluated in terms of different production options.

4.4.1 Phase space distribution of ^{3}He

The phase space distribution of ^{3}He in the p_t/m (the mass scaled transverse momentum) and y_{lab} (rapidity in laboratory frame) plane is depicted in Fig. 4.6, where $y_{AA} = 0.894$ is the mid-rapidity of Ni+Ni collisions at 1.91A GeV and $y_{lab} = 0$ is the target rapidity. The blue dashed curves indicate the polar angle acceptance of the RPC barrel ($30^o < \theta < 52^o$) and the PLB ($54^o < \theta < 110^o$). As described in section 3.4, ^{3}He can only be identified by combining the information measured by the CDC and the TOF detector. This causes several detection limitations on its phase space distribution, which are listed below.

(a) The lowest transverse momentum of ^{3}He is constrained by the radial distance of the TOF barrels, it has a value of 0.17 GeV/c according to Eq. 2.1.

(b) The RPC barrel and the plastic barrel do not cover the full azimuthal angle. For the RPC barrel, beside the vacancy of the 4 super-modules, there are gaps between the installed super modules. The RPC barrel covers about 70% of the full azimuthal angle. Gaps also exist in between the strips of the PLB. The PLB covers about 80% of the total azimuthal angle. There is also a gap between the RPC barrel and the plastic barrel. It spans from about 52^o to 54^o, which is visible in Fig. 4.6.

(c) In the RPC acceptance, the ^{3}He with low momenta are stopped in a certain glass layer of the RPC counter. In this case, only a weak signal or even no signal is induced on the RPC readout electrodes. Even the induced weak signal may be cut away by the threshold of pre-amplifiers, which are designed to suppress the low amplitude noise. In Fig. 4.6, the population of ^{3}He dramatically decreases in the

low momentum region of the RPC acceptance, and a clear edge is visible from the high population region to the low population region. The edge is described by the black dotted line, which corresponds to a fixed momentum of p=0.9 GeV/c. As the detection efficiency of these low momenta particles is not straightforward, in the current analysis, only those ^{3}He with a total momenta larger than 0.9 GeV/c are taken into account.

For the convenience of presenting ${}^3_\Lambda$H results, four phase space regions need to be introduced, depicted by the green lines in Fig. 4.6. These phase space regions are called A1, A2, A3 and A4, respectively. Their boundary conditions are listed in table 4.5. The reason for defining these regions is because the signal of ${}^3_\Lambda$H is only observed in the phase space region A1, while in the other regions there is no significant signal observed. Detailed results are presented in the following sections.

Table 4.5: Boundaries of the phase space region A1, A2, A3 and A4.

	A1	A2	A3	A4
y_{lab}	0.2-0.4	0.4-0.6	0.0-0.25	0.0-0.25
p_t/m	0.2-0.4	0.4-0.6	0.2-0.4	0.4-0.6
θ	$30^o < \theta < 54^o$	$30^o < \theta < 54^o$	$56^o < \theta < 110^o$	$56^o < \theta < 110^o$

4.4.2 Selection criteria for ${}^3_\Lambda$H reconstruction

π^--mesons are registered in the CDC. In order to discard the π^-'s with low momenta spiraling inside the CDC, the minimum transverse momentum of the accepted π^- is 0.06 GeV/c. In order to discard the bulk π^-'s originating from the primary vertex, the transverse impact parameter is an effective quantity in achieving this goal. The measured mean of the transverse impact parameter of π^- in the S325e experiment is about -0.4 cm, this is caused by the imperfect azimuthal angle reconstruction. A modified transverse impact parameter $d_0' = d_0 - 0.4$ is used to select the off-vertex π^-.

The hit multiplicity ($HMUL$) of π^- and ^{3}He is required to be larger than 34. This ensures the precision of the extracted curvatures. The polar angle of ^{3}He is given by the hit on the TOF barrel with respect to the primary vertex, which is limited in the polar angle acceptance of the TOF detectors. A hit in the TOF detector is matched with the extrapolated CDC track in the transverse plane. Unlike the selected proton in the Λ reconstruction, the transverse impact parameter d_0 of ^{3}He does not provide any useful information, thus its range is rather open. The minimum momentum of ^{3}He is $p_{min} = 0.9$ GeV/c, for the reason discussed in the last sub-section.

For the ${}^3_\Lambda$H candidates, the quantity r_s is constrained in a range from 1.5 cm to 15 cm. Since the mean lifetime of ${}^3_\Lambda$H is similar to the mean lifetime of the Λ hyperon, about 96% of the Λ hyperon would decay in a flight distance of 15 cm assuming they have a mean velocity of $\beta = 0.5c$, c is the speed of light in vacuum. The quantity $ccnt$ is the number of intersection points between two tracks inside the drift volume of the CDC. The tracking inefficiencies for crossing and neighbouring tracks are reduced, this effect is not present in mixed events [126], therefore, pairs crossing each other inside the CDC are excluded

from the reconstruction. The quantity $\Delta\phi_{12}$, the azimuthal angle difference of π^- and ^{3}He, is required to be larger than 20 degrees. In the analysis, the (π^-,^{3} He) pairs with the invariant mass larger than 4.2 GeV/c^2 are excluded, as it is much larger than an nominal mass of ${}^{3}_{\Lambda}$H. All constraints discussed above, and the meaning of the cut quantities are listed in table 4.5.

During the evaluation of the invariant mass of ${}^{3}_{\Lambda}$H candidates, we found that it is not enough to obtain a significant signal by only applying the cuts described above. The constraints for the phase space of candidates are necessary to observe a clear signal. The phase space region A1-A4 are defined in table 4.5 (also depicted in Fig. 4.6). The signal of ${}^{3}_{\Lambda}$H is only observed in the phase space region A1. The variables used to define the region A1 are listed in table 4.6 as well. Noting that in calculating the variable p_t/m, p_t is the transverse momentum of the ${}^{3}_{\Lambda}$H candidate and m is the nominal mass of ${}^{3}_{\Lambda}$H, i.e. $m_{{}^{3}_{\Lambda}H}$=2.9913 GeV/c^2. And additional multiplicity cuts, i.e. $20 < T_{MUL} < 60$ and $50 < P_{MUL} < 45$, are necessary to obtain a significant signal of ${}^{3}_{\Lambda}$H, which are listed in the lowest columns of table 4.6. The corresponding impact parameter range of these centrality constraints is further discussed in chapter 6.

4.4.3 Invariant mass of ${}^{3}_{\Lambda}$H

By applying the cuts listed in table 4.6, the invariant mass spectrum of the ${}^{3}_{\Lambda}$H candidates (open circles) and the normalised mixed-event background spectrum (solid curve) are obtained, as shown in Fig. 4.7(A1.a). The normalization region is depicted by a horizontal arrow, which goes from 3.2 to 4.2 GeV/c^2. The invariant mass spectrum, after subtracting the mixed-event background, is shown in Fig. 4.7(A1.b), in which an excess is present around the nominal mass of ${}^{3}_{\Lambda}$H. The excess is fitted by a Gaussian distribution, with a mean of 2.9927 ± 0.0017 GeV/c^2 and a width of 5.6 ± 1.0 MeV/c^2. The fitted mean is compatible with the nominal mass of ${}^{3}_{\Lambda}$H.

By just replacing the constraints of the phase space A1 to these of the phase space A2, A3 and A4, as given in table 4.5, the invariant mass spectrum of the ${}^{3}_{\Lambda}$H candidates (open circles) and the normalised mixed-event background distribution (solid curve) in the phase space region A2-A4 are obtained, depicted in the panel (A2.a), (A3.a) and (A4.a) of Fig. 4.7. The spectrum after subtracting the background is shown in the panel (A2.b), (A3.b) and (A4.b) of Fig. 4.7, respectively. Unlike in the region A1, in the other regions there is no clear excess visible in the final invariant mass spectrum. The error bars in the spectra represent the statistical error only.

As a reference, using the selection cuts listed in table 4.4 and the phase space constraints of phase space region A1, A2, A3 and A4, the invariant mass spectrum of the Λ hyperon candidates and the normalized mixed-event background are obtained, as shown in the panel (A1.a), (A2.a), (A3.a) and (A4.a) of Fig. 4.8. The spectrum after the background subtraction in each region is shown in the panel (A1.b), (A2.b), (A3.b) and (A4.b) of Fig. 4.8, respectively. In the final invariant mass spectra, the peak around the invariant mass of the Λ hyperon is fitted by a Gaussian distribution. The fitted mean in the region A1, A2, A3 and A4 is 1115.6±0.2 MeV/c^2, 1115.4±0.6 MeV/c^2, 1115.8±0.3 MeV/c^2

Table 4.6: ${}^{3}_{\Lambda}$H selection cuts in the phase space region A1.

Particle	quantity	unit	cut	meaning
π^-	p_t	GeV/c	> 0.06	transverse momentum
	m_{CDC}	GeV/c^2	0.05$< \cdots <$0.4	CDC mass
	$\|d_0 - 0.4\|$	cm	1.5$< \cdots <$10.	transverse impact parameter
	z_1	cm	-10.$< \cdots <$25.	z-coordinator at $r = r_s$
	θ	[^{o}]	40.$< \cdots <$130.	polar angle
	Q	e	-1.5$< \cdots <$-0.5	charge
	HMUL	-	> 34	hit multiplicity
^{3}He	m_{CDC}	GeV/c^2	1.8$< \cdots <$3.5	CDC mass
	$2\times m_{BAR}$	GeV/c^2	2.3$< \cdots <$3.2	barrel mass, Q=2
	$\|d_0\|$	cm	$<$1.	transverse impact parameter
	z_2	cm	2.$< \cdots <$25.	z-coordinator at $r = r_s$
	θ	[^{o}]	30.$< \cdots <$54.	polar angle
	Q	e	$>$1.5	charge
	HMUL	-	> 34	hit multiplicity
${}^{3}_{\Lambda}$H	ccnt	-	0	cross count in the CDC
	r_s	cm	1.5$< \cdots <$15.	dis of V1,2 in the (x, y)-plane
	z_s	cm	2.$< \cdots <$25.	dis of V1,2 in the (r, z)-plane
	$\|d_0\|$	cm	-1.$< \cdots <$1.	transverse impact parameter
	θ	[^{o}]	30.$< \cdots <$52.	polar angle
	Δz	cm	-30.$< \cdots <$20.	$z_1 - z_2$
	$\|d\phi\|$	[^{o}]	$<$10.	$\phi_{Hyp} - \phi_s$
	$\|\Delta\phi_{12}\|$	[^{o}]	$>$20.	$\|\phi_1 - \phi_2\|$
	m_{inv}	GeV/c^2	$<$4.	invariant mass
	p	GeV/c	$>$0.82	momentum
	$\mathbf{y_{lab}}$	-	0.15$< \cdots <$0.35	rapidity in lab frame
	$\mathbf{p_t/m_{hyp}}$	c	0.2$< \cdots <$0.4	mass scaled transverse momentum
	TMUL	-	20.$< \cdots <$60.	CDC track multiplicity
	PMUL	-	5.$< \cdots <$45.	PLW hit multiplicity

and 1116.3±0.2 MeV/c^2, respectively. The fitted widths are around 3 MeV/c^2. In the concerned phase space region A1 and A2, the combinatorial background is well described by the mixed-event distribution. This implies that the π^- and p are properly detected in these two phase space regions. In the phase space region A3 and A4, the invariant mass of the Λ hyperon is reasonably reconstructed, but a deviation between the invariant mass spectrum of the Λ candidates and that of the mixed events is observed at a lower mass region. The reason for this still needs to be understood.

The number of identified Λ hyperons in each phase space region is the integrated counts from the final spectrum in a range of mean±3σ, which are listed in table 4.10.

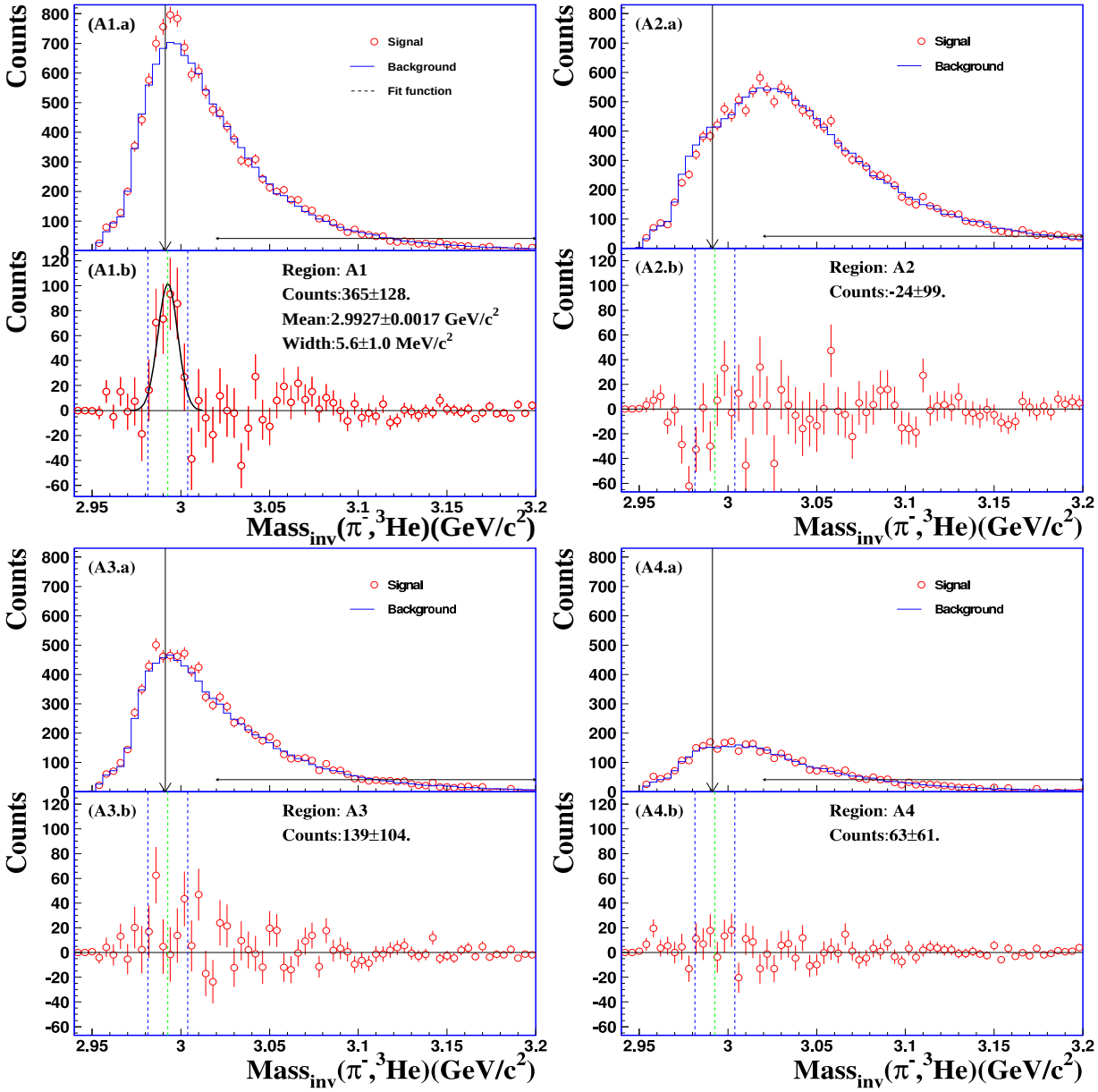

Figure 4.7: Invariant mass distribution of $\pi^{-}-^{3}$He pairs (open circles) and mixed-event background (solid curve) from region A1, A2, A3 and A4 are shown in the panel (A1.a), (A2.a), (A3.a) and (A4.a), the horizontal arrows depict the normalization region. Invariant mass distributions after subtracting the normalized mixed-event background are depicted in the panel (A1.b), (A2.b), (A3.b) and (A4.b), respectively. In the panel (A1.b), the excess is fitted by a Gaussian function.

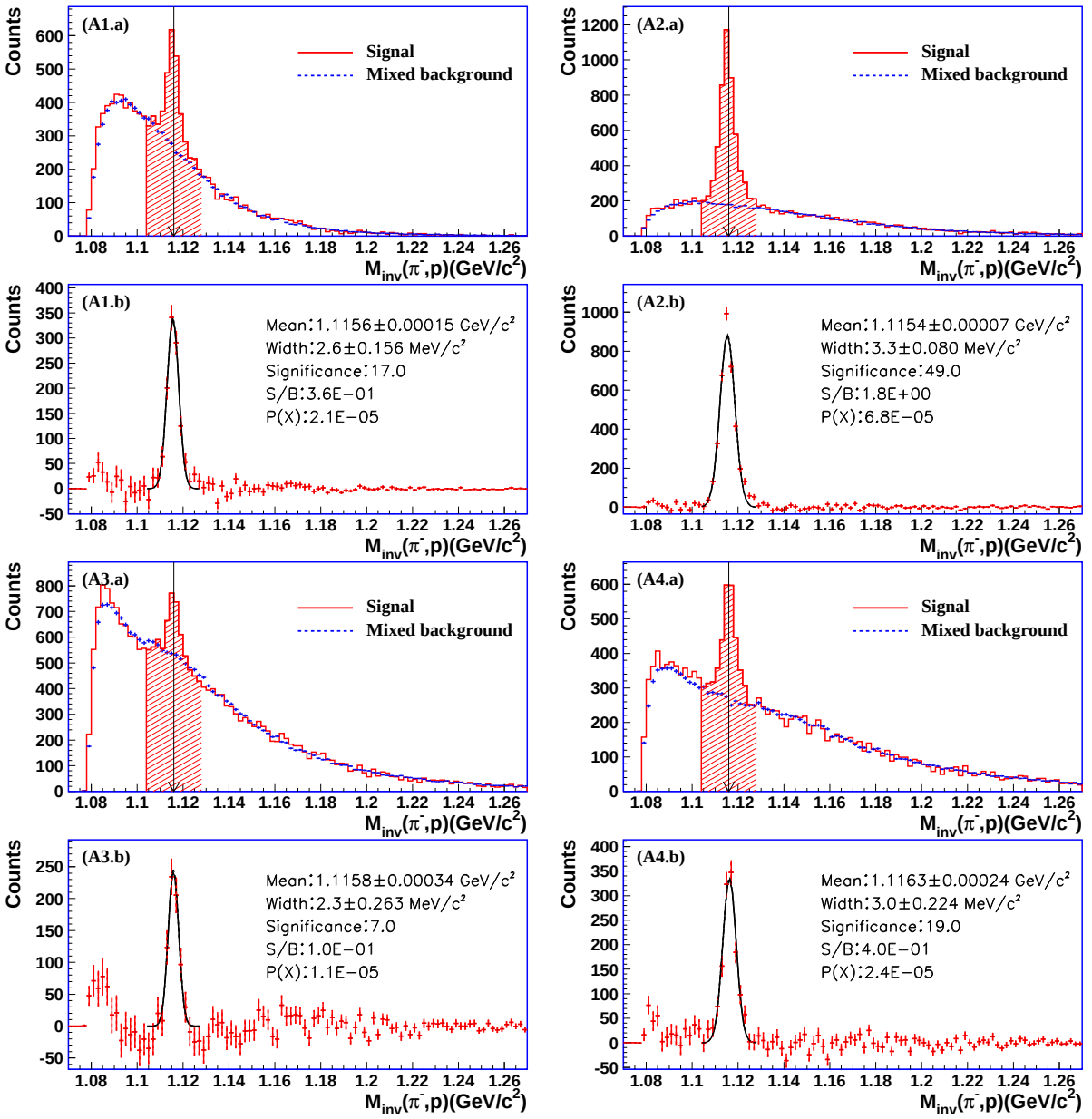

Figure 4.8: Invariant mass distribution of (π^--p) pairs (solid red curve) and normalized mixed-event background (dashed blue curve) in the phase space region A1, A2, A3 and A4 are shown in the panels of (A1.a), (A2.a), (A3.a) and (A4.a). Invariant mass distribution, after subtracting the corresponding normalized mixed-event background, is shown in the panel (A1.b), (A2.b), (A3.b) and (A4.b), respectively. In each panel, the excess is fitted by a Gaussian distribution.

4.4.4 Significance evaluation

The significance is a statistical quantity used to quantify the degree of confidence that the measured result is a new phenomenon or the known background. For a counting experiment, the significance can be calculated by the following formula [127]

$$\text{snf} = \frac{S}{\sqrt{S+B}}, \tag{4.10}$$

where S and B are the integrated signal and background counts in a given region. For ${}^{3}_{\Lambda}$H reconstruction, S is the signal counts integrated in a given region of the final invariant mass spectrum. B is the number of background counts, which is integrated from the normalized mixed-event spectrum in the same region. Formally they are given by the following expressions

$$S = \sum_{i\in\Omega}(S_i - B_i \times \eta), \qquad B = \sum_{i\in\Omega}(B_i \times \eta), \tag{4.11}$$

where Ω is the selected signal region, S_i is the number of counts in i-th bin, B_i is the number of counts of $i-$th bin in the original mixed-event spectrum and η is the normalization factor. The normalization factor η is a ratio of integrated counts from the signal and the mixed-event spectrum in a certain non-signal region. Obviously, the significance of the signal is influenced by the following factors: (a) the shape of the signal and the mixed-events spectrum; (b) the normalization factor η; (c) the range of the signal region. Under given production conditions, the spectrum of the signal and the mixed-event background is almost fixed, as the possible particle combinations are fixed by the total number of events. In the following, the dependence of the significance on the normalization factor and the range of the signal region are discussed.

Normalization factor optimization

The normalization factor is calculated by the following expressions

$$\eta = \frac{S'}{B'}, \quad S' = \sum_{i\in\Omega'} S_i, \quad B' = \sum_{i\in\Omega'} B_{i,mix}, \tag{4.12}$$

where Ω' is the chosen normalization region (non-signal region), S' and B' are the integrated counts from the final signal spectrum and the mixed-event spectrum in Ω'.

If the mixed-event background can describe the shape of the combinatorial background spectrum, by applying a proper normalization factor, the counts in the non-signal region of the background-subtracted spectrum should fluctuate around zero. As having demonstrated in the Λ reconstruction (see the lower panel of Fig. 4.5), the counts in the non-signal region fluctuate marginally around zero in the final invariant mass spectrum, except the invariant mass peak of the Λ hyperon.

In some cases, if choosing a different normalization region, the obtained normalization factor may be different. This effect can be caused by the large count fluctuation of some

bins or the mixed-event spectrum has a minor deviation from the combinatorial background spectrum. For the rare probe identification, this kind of effect becomes important because the combinatorial background is orders of magnitude larger than the signal, which may dramatically influence the significance of the signal. In order to obtain a most stable signal, an optimization of the normalization factor is necessary.

If the obtained normalization factor deviates from the optimal normalization factor, the counts in the non-signal region of the final spectrum would fluctuate around a non-zero value. Therefore, inspecting the counts in the non-signal region of the final spectrum can afford information about how well the normalized mixed-event spectrum describes the combinatorial background. Since one does not know in which non-signal range the obtained normalization factor is at its optimum, the optimization is done by an iteration procedure.

Fig. 4.9 is an example which demonstrates this procedure. In the first step, the initial normalization factor η is calculated in the normalization region from 3.02 to 3.2 GeV/c^2 (depicted by a horizontal arrow in the upper panel of Fig. 4.9). The invariant mass spectrum of ${}^{3}_{\Lambda}$H after the background subtraction is shown in the middle panel of Fig. 4.9. An excess in the spectrum is fitted by a Gaussian function, with a mean of 2.9927 GeV/c^2 and a variance of 5.6 MeV/c^2. Although the optimal normalization factor may differ from the current one, the mean and the width of the excess should not change significantly. Therefore, it is safe to choose the region of 3.5σ away from the fitted mean as the non-signal region, i.e. the region Ω_L and Ω_H in the middle panel of Fig. 4.9. While, only the counts in the non-signal Ω_H are used to evaluate the normalization factor. As in the region Ω_L, the counts may contain the (π^-,^{3}He) pairs which decayed from the other hypernucleus, such as ${}^{4}_{\Lambda}$H $\rightarrow \pi^- +$ p+^{3}He. The lower panel of Fig. 4.9 shows the count distribution in the non-signal region Ω_H. The mean and the RMS of the distribution are 0.86 and 12, respectively.

In the second step, in order to find out the optimal normalization factor, the normalized mixed-event spectrum of the first step is multiplied by a series of factors from -10% to 10% with a step of 0.25%. At each step, the newly obtained background spectrum is subtracted from the signal spectrum. The mean and the RMS of the counts in the non-signal region Ω_H are calculated. The extracted mean and the RMS as a function of the multiplication factor is plotted in the upper panel of Fig. 4.10, the RMS of each step is shown by the error bar. In order to find the optimised normalization factor with the minimum mean and the narrowest RMS, a score factor W is introduced as the following

$$W(i) = \sqrt{(\langle M \rangle_i)^2 + (RMS_i/10)^2}\ , \tag{4.13}$$

where, $W(i)$, $\langle M \rangle_i$ and RMS_i are the score, the mean and the RMS at i-th step. The weight of the RMS is taken into account only if $\langle M \rangle_i$ is in the region close to zero, therefore the RMS gains a scaled factor of 10, which is of the order of the RMS values. The correlation of the obtained score as a function of the multiplication factor is shown in the lower panel of Fig. 4.10. The minimum of the score i.e. the combined minimum of the mean and the RMS, is obtained. The corresponding multiplied factor is an optimal factor referring to the normalization factor obtained in the first iteration. The optimized factor $\eta_{opt} = 0.9975$, means that the mixed-event background should be about 0.25%

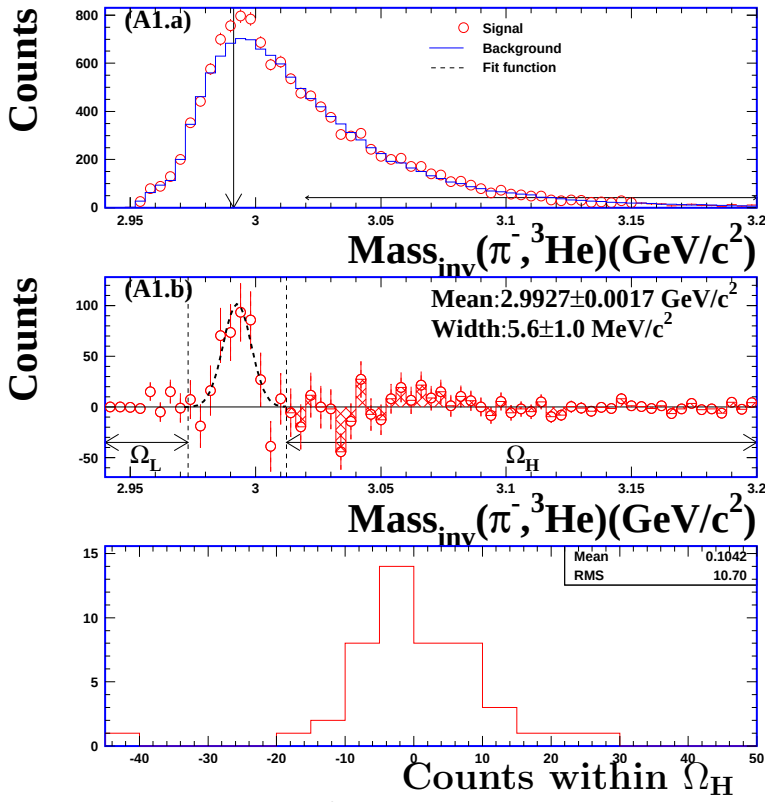

Figure 4.9: Invariant mass spectrum of $^{3}_{\Lambda}$H candidates (open circles) and the normalized mixed-event background spectrum (solid curve) of (π^-,^{3}He) pairs in the phase space region A1 (upper). The resulting spectrum after subtracting the background (middle), the excess is fitted by a Gaussian distribution. The region Ω_L and Ω_H are the non-signal regions. Distribution of counts in the non-signal region Ω_H (lower).

lower than the one obtained in the first step. All of the mixing-event spectra obtain in the first iteration e.g. the distributions of the decay time, the rapidity distribution and so on, are scaled by the optimal factor.

Signal range evaluation

Applying the optimised normalization factor, the invariant mass spectrum of the $^{3}_{\Lambda}$H candidates (open circles) and the mixed-event background distribution (solid curve) in the phase space region A1 are obtained, shown in the upper panel of Fig. 4.11. The invariant mass after subtracting the background is shown in the lower panel of Fig. 4.11. The excess is attributed to the decay of $^{3}_{\Lambda}$H, it is fitted by a Gaussian distribution with a mean of 2.9927 ± 0.0017 GeV/c^2 and a width of 5.6 ± 1.0 MeV/c^2. Within the error, the reconstructed invariant mass agrees with the nominal mass of $^{3}_{\Lambda}$H.

Since the number of signal and background counts depends on the range of the signal region, the significance depends on the range of the signal region as well. In order to investigate the dependence of the significance on the range of the signal region, the lower and upper boundary of the signal regions are symmetric around the fitted mean, which

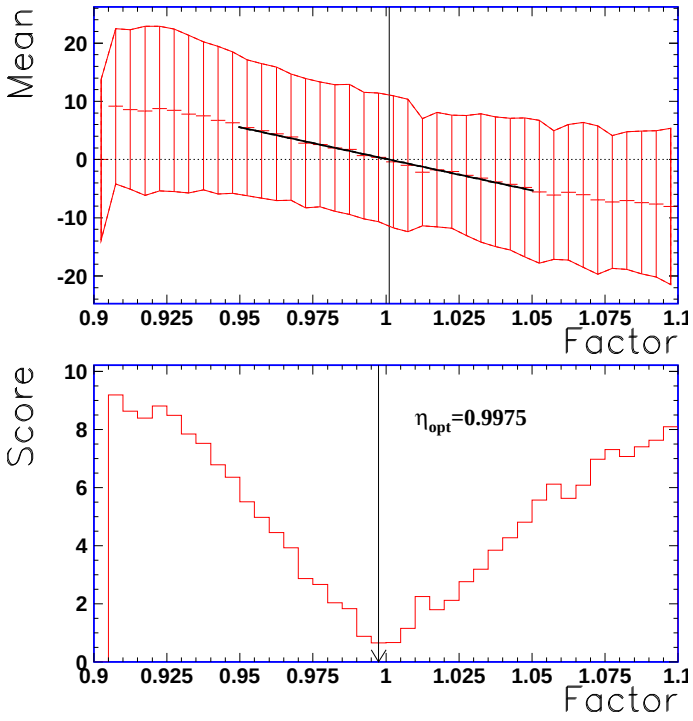

Figure 4.10: Mean of counts in the non-signal region as a function of the multiplication factor (upper). The error bars are the RMS of the counts in each step. Score factor as a function of the multiplication factor (lower).

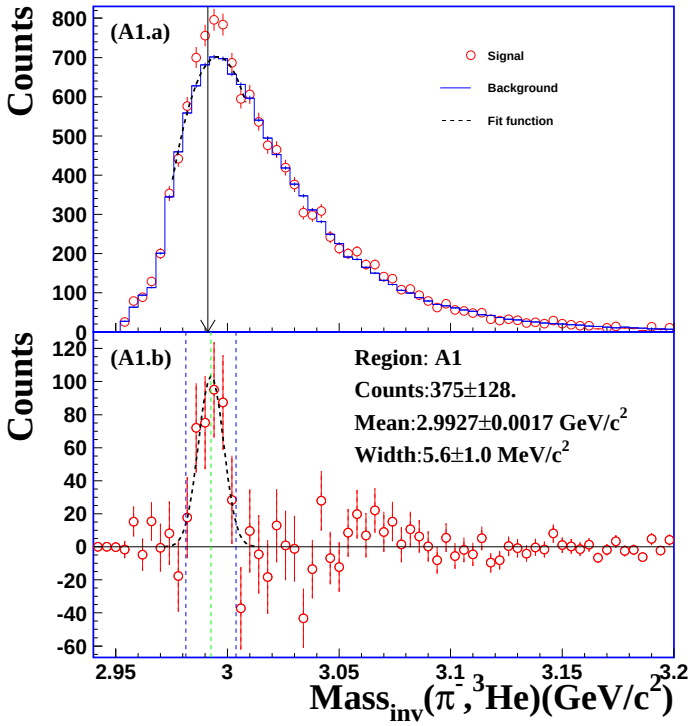

Figure 4.11: Invariant mass of ${}^{3}_{\Lambda}$H candidates (open circles) and the mixing-event spectrum after the normalization factor optimization (solid curve) (upper). Invariant mass spectrum after subtracting the background (lower).

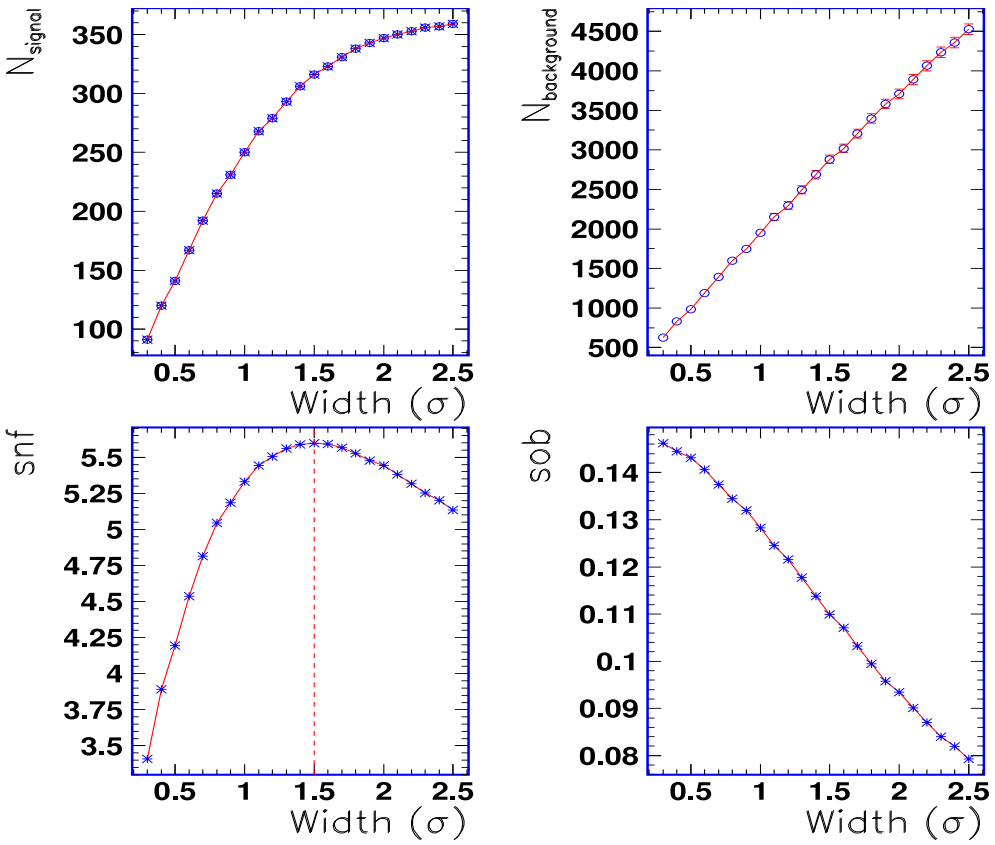

Figure 4.12: Number of integrated signal counts (upper left) and background counts (upper right), the significance (lower left) and the signal-to-background (SOB) (lower right) as a function of the width of signal region, which is in units of σ.

are expressed as $\bar{M} - i \times \sigma/N$ and $\bar{M} + i \times \sigma/N$, where $\bar{M}$ and σ is the fitted mean and the width of the excess, N is the bin number in one sigma range and i is the i-th signal region. In order to minimise the uncertainties from the different bin size, the final background spectrum is fitted by a third order polynomial function in a range of $\bar{M} \pm 3\sigma$. The signal counts S and the background counts B are integrated from the fitted Gaussian and polynomial function, respectively. In each range, the significance of the signal is calculated with Eq. 4.10.

The number of integrated signal counts (upper left) and the background counts (upper right), the significance (lower left) and the signal-over-background ratio (SOB) (lower right) as a function of the width of the signal region are shown in Fig. 4.12. The width of the signal region is in unit of σ. The integrated signal count saturates at about 363. The background counts increase by enlarging the range of the signal region. The significance increases by opening the range of the signal region. At about 1.5σ, the significance reaches a maximum value of about 5.6. The SOB is decreasing by opening the width of the signal region.

4.4.5 Production option dependence

As presented in Chapter 3, the vertex and the reaction plane are the reference for the position and the angle measurements, respectively. The vertex can be reconstructed by the different iteration time (see section 3.2). The reaction plane can be reconstructed from the quantities measured by the CDC and/or the PLW. The reconstruction processes are steered by the several production options. In order to ensure that the observed signal is a general effect rather than one triggered by a special combination, inspecting the dependence of the final results like mean, width and significance of the signal on those production options is necessary.

The primary vertex is reconstructed by an iteration procedure. The number of iterations is controlled by a production option called "shift", as described in chapter 3. The selected particle pairs are treated as the "decay" products from the secondary vertex. Additionally, one or more particles can be excluded from the primary vertex reconstruction, aiming to improve the precision of the primary vertex. The exclusive level is controlled by an option called "vi". The reaction plane can be reconstructed by the CDC and/or the PLW, which is controlled by an option "rp". The meaning and the possible value of the production options are summarised in table 4.7.

Table 4.7: Value and meaning of the production options.

Quantity	option	value	action
Vertex	shift	1-6	iteration times
	vi	0	no track is excluded
		1	π^- is excluded
		2	both π^- and ^{3}He are excluded
Reaction plane	rp	0	PLW
		1	CDC + PLW
		2	CDC

For each option combination, the quantities used to quantify the signal, like the mean, the width and the significance, are extracted. The fitted mean and width (error bar) of the excess (first column) and the significance (second column) as a function of the "shift" option are shown in Fig. 4.13. In the first column, a reference mean of 2.9926 GeV/c^2 and a reference width of 6 MeV/c^2 are shown by the red dashed line and the blue dashed lines, respectively. The significances are calculated within the signal region range of Mean$\pm$1.5σ, as the significance reaches the maximum value in this range. The figures in the upper, middle and lower row of Fig. 4.13 are obtained with the option rp=0, 1 and 2, respectively. In each panel, there are three histograms produced with option vi=0 (red), 1 (green) and 2 (blue).

Within all of the possible combinations of production options, the fitted mean and width of the excess are quite stable. Keeping the other options the same, the significance obtained with vi=1 is consistent with the one obtained with vi=2, while the significance obtained with vi=0 has a large difference to the results obtained with option vi=1 or vi=2. This is understandable, because for option vi=1 or vi=2, the π^- which belongs to

a $^{3}_{\Lambda}$H candidate is excluded from the primary vertex reconstruction. This π^- has a large impact on the position of the primary vertex, because it has a large impact parameter. The impact parameter of ^{3}He is rather small, therefore it has a minor influence on the position of primary vertex. From this exercise, we can conclude that under all kinds of production option combinations, similar results of the $^{3}_{\Lambda}$H signal can be derived. The results of $^{3}_{\Lambda}$H presented in this work are produced with the option combination of shift=2, vi=1 and rp=1.

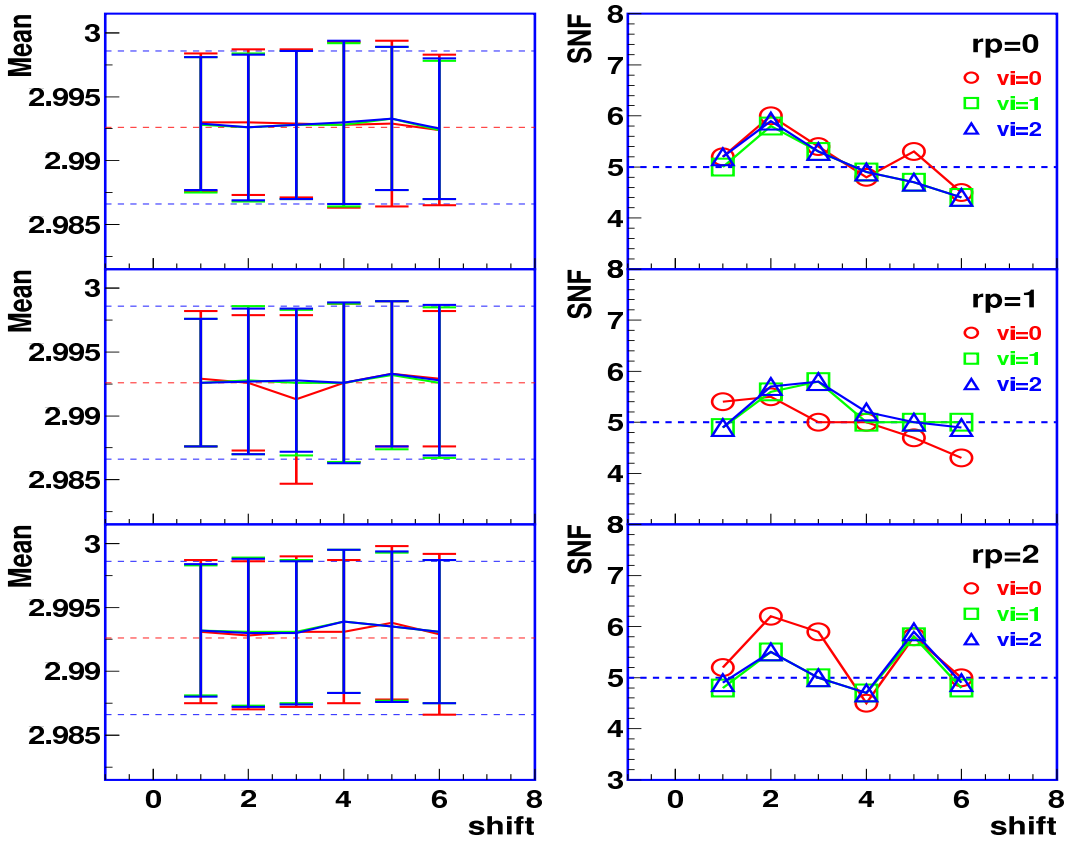

Figure 4.13: The fitted mean and the width (depicted by the error bar) of $^{3}_{\Lambda}$H signal (first column) and the significance (second column) as a function of the "shift" option. The significance is calculated within the signal region range of Mean$\pm 1.5\sigma$. The histograms in the upper, middle and lower row are produced under the "rp" options 0,1 and 2. In each sub-panel, the data points were produced under that "vi" equals to 0, 1 and 2 and are depicted by the red, green and solid curves (first column) or symbols (second column), respectively.

4.5 $^{4}_{\Lambda}$H reconstruction

The procedure for reconstructing $^{4}_{\Lambda}$H from its two-body π^--decay channel, i.e. $^{4}_{\Lambda}\mathrm{H}\rightarrow\pi^- +{}^4$He, is almost identical to the $^{3}_{\Lambda}$H reconstruction except for an exchange of the ^{3}He by ^{4}He. In this section, the phase distribution of ^{4}He is inspected first, then the selection criteria

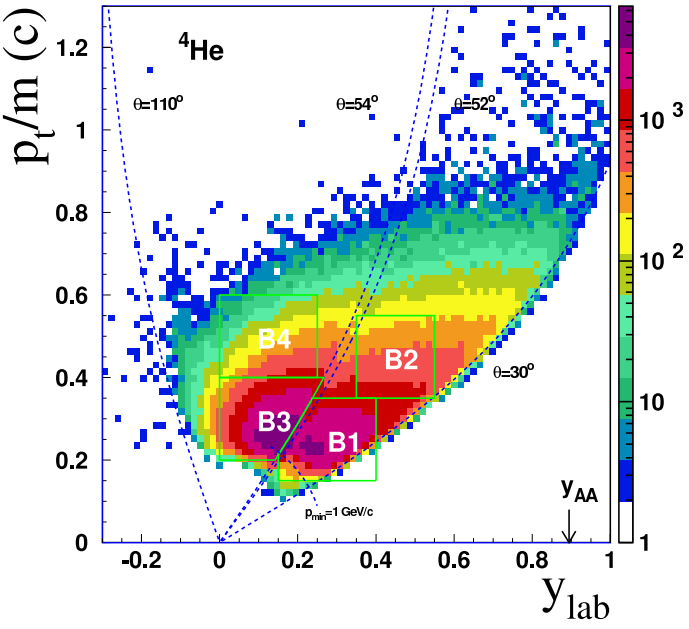

Figure 4.14: Phase space distribution of ^{4}He in the $p_t/m_\alpha - y_{lab}$ plane from the S325e experiment. The dashed lines show the polar angle acceptance of the RPC and the PLB.

of ${}^4_\Lambda$H are described. In the third part, the reconstructed invariant mass spectrum of ${}^4_\Lambda$H in various phase space regions is present in the spectrum. In the last part, the dependences of the significance of the signal on the production options are discussed.

4.5.1 Phase space distribution of ^{4}He

The phase space distribution of ^{4}He in the $p_t/m_\alpha - y_{lab}$ plane is shown Fig. 4.14, m_α is the mass of ^{4}He, the blue dashed lines show the polar angle acceptance of the RPC barrel ($30^o < \theta < 52^o$) and the PLB ($54^o < \theta < 110^o$). Quite similar to the phase space distribution of ^{3}He, the population of ^{4}He decreases dramatically in the low momentum region of the RPC acceptance. An edge between the high population and the low population is at a total momentum of $p_{lab} = 1$ GeV/c, indicted by the black curve in Fig. 4.14. This is because these ^{4}He with low momenta are stopped in a certain glass layer, a similar feature was discussed in the description of the ^{3}He phase space distribution. As the detection efficiencies of those stopped particles are hard to estimate, in the current ${}^4_\Lambda$H reconstruction, the momentum of ^{4}He is required to be larger than 1.0 GeV/c.

Like the ${}^3_\Lambda$H reconstruction, a significant signal of ${}^4_\Lambda$H is only observed in a certain region of the phase space. The boundaries of the concerned phase space region B1, B2, B3 and B4 are listed in table 4.8, as depicted by the solid curves in Fig. 4.14. During the invariant mass evaluation, a significant signal of ${}^4_\Lambda$H is only observed in the phase space region B1, the detailed results are presented in the following sections.

4.5.2 Selection criteria for ${}^4_\Lambda$H reconstruction

The selection criteria for the channel: ${}^4_\Lambda\text{H}\rightarrow\pi^- + {}^4$ He are quite similar to those used to reconstruct ${}^3_\Lambda$H from its two-body π^--decay channel. The constraints for π^- are the same

Table 4.8: Boundaries of the phase space region B1, B2, B3 and B4.

Region	B1	B2	B3	B4
y_{lab}	0.15-0.4	0.4-0.6	0.-0.25	0.-0.25
p_t/m	0.15-0.35	0.35-0.55	0.2-0.4	0.4-0.6
θ	$30^o < \theta < 54^o$	$30^o < \theta < 54^o$	$56^o < \theta < 110^o$	$56^o < \theta < 110^o$

as those used for ${}^{3}_{\Lambda}$H reconstruction. The cuts of π^-, ^{4}He and the ${}^{4}_{\Lambda}$H candidate, as well as the constraints for the phase space region B1 are listed in table 4.9. In deriving the quantity p_t/m, the $m_{{}^{4}_{\Lambda}\mathrm{H}}$ =3.9928 GeV/c^2 is used. The last two columns of table 4.9 are the centrality constraints for the track multiplicity in the CDC and the hit multiplicity in the PLW, i.e. $30 < TMUL < 50$ and $10 < PMUL < 35$.

Table 4.9: Selection criteria for ${}^{4}_{\Lambda}$H reconstruction.

particle	quantity	unit	cut	meaning
π^-	p_t	GeV/c	> 0.06	transverse momentum
	m_{CDC}	GeV/c^2	0.05< $\cdots$ <0.25	CDC mass
	$\lvert d_0 - 0.4\rvert$	cm	1.5< $\cdots$ <10.	transverse impact parameter
	z_1	cm	-5.< $\cdots$ <25.	z-coordinator at $r = r_s$
	θ	[^{o}]	40.< $\cdots$ <115.	polar angle
	Q	e	-1.5< $\cdots$ <-0.5	charge
	HMUL	-	> 34	Hit multiplicity
^{4}He	m_{CDC}	GeV/c^2	2.7< $\cdots$ <4.7	CDC mass
	$2\times m_{BAR}$	GeV/c^2	3.2< $\cdots$ <4.2	Barrel mass, Q=2
	$\lvert d_0\rvert$	cm	<1.	transverse impact parameter
	z_2	cm	1.< $\cdots$ <20.	z-coordinator $(z_1 + z_2)/2$
	θ	[^{o}]	30.< $\cdots$ <54.	polar angle
	Q	e	>1.5	charge
	HMUL	-	> 34	Hit multiplicity
${}^{4}_{\Lambda}$H	ccnt	-	0	cross count in the CDC
	r_s	cm	1.5< $\cdots$ <12.	dis of V1,2 in (x, y)-plane
	z_s	cm	1.< $\cdots$ <20.	dis of V1,2 in (r, z)-plane
	$\lvert d_0\rvert$	cm	-0.8< $\cdots$ <0.8	transverse impact parameter
	θ	[^{o}]	30.< $\cdots$ <52.	polar angle
	Δz	cm	-30.< $\cdots$ <15.	$z_1 - z_2$
	$d\phi$	[^{o}]	-7.< $\cdots$ <12.	$\phi_{Hyp} - \phi_s$
	$\lvert\Delta\phi_{12}\rvert$	[^{o}]	>10.	$\lvert\phi_1 - \phi_2\rvert$
	m_{inv}	GeV/c^2	<4.1	invariant mass
	p	GeV/c	>0.95	momentum
	$\mathbf{y_{lab}}$	-	0.15< $\cdots$ <0.35	rapidity in lab frame
	$\mathbf{p_t/m}$	c	0.15< $\cdots$ <0.4	mass scaled p_t
	TMUL	-	30.< $\cdots$ <50.	CDC track multiplicity
	PMUL	-	10.< $\cdots$ <35.	PLW hit multiplicity

4.5.3 Invariant mass of $^{4}_{\Lambda}$H

By applying the cuts listed in table 4.9, the invariant mass spectrum of the $^{4}_{\Lambda}$H candidates (open circles) and the normalized mixed-event background distribution (solid curve) in the phase space region B1 are obtained, see Fig. 4.15(B1.a). The normalization range is marked by a horizontal arrow in the range of 3.953 to 4.1 GeV/c^2. After subtracting the background, the spectrum is shown in Fig. 4.15(B1.b). The excess in the spectrum is fitted by a Gaussian distribution, the obtained mean and width are 3.9924 GeV/c^2 and 4.6 MeV/c^2, respectively. Replacing the phase space constraints of B1 by those of B2, B3 and B4, the invariant mass spectrum of the $^{4}_{\Lambda}$H candidates (open circles) and the normalized mixed-event spectrum (solid curve) are obtained, as shown in the panels (B2.a), (B3.a) and (B4.a) of Fig. 4.15. The spectra after the background subtraction are shown in the panels (B2.b), (B3.b) and (B4.b), respectively. The counts in the final invariant mass spectra, obtained in the region B2, B3 and B4, are comparable with the statistic fluctuations, no significant signal of $^{4}_{\Lambda}$H is observed.

In the phase space region B1, the normalization factor is optimised by the procedure presented in section 4.4.4. The non-signal regions are 3.5σ away from the fitted mean and only the high mass part is taken into account (like Ω_H in Fig. 4.9). In the first step, the normalization factor is calculated in a range of 3.953 to 4.1 GeV/c^2. In the second step, the normalized background is multiplied by a factor from -10% to 10% with a step of 0.25%. In each step, the mean and the RMS of the counts in the considered non-signal region are calculated. The obtained mean and RMS as a function of the multiplication factor is shown in the upper panel of Fig. 4.16, the RMS are indicated by the error bars. The score factor is calculated in each step according to Eq. 4.13. The score as a function of the multiplication factor is shown in the lower panel of Fig. 4.16. The minimum value of the score is located at $\eta_{opt} = 0.989$, which represents the combined minimum of the mean and the RMS. This means that all of the mixed-event spectra need to be downscaled by 1.1% with respect to the normalized mixed-event spectra in the first iteration.

By applying the optimized normalization factor, the invariant mass spectrum of the $^{4}_{\Lambda}$H candidates (open circles) and the final mixed-event background distribution (solid curve) are obtained, shown in the upper panel of Fig. 4.17. The invariant mass, after subtracting the background, is displayed in the lower panel of Fig. 4.17. The excess near the nominal mass of $^{4}_{\Lambda}$H, is attributed to the decay of the $^{4}_{\Lambda}$H. The excess is fitted by a Gaussian distribution, the mean and the width of Gaussian function are 3.9226 ± 0.0010 GeV/c^2 and 4.0 ± 1.6 MeV/c^2.

Like in case of $^{3}_{\Lambda}$H, the significance of the $^{4}_{\Lambda}$H signal is evaluated in a series of signal regions. The lower and upper boundaries of the i-th signal region are $\bar{M} - i\times\sigma/N$ and $\bar{M} + i\times\sigma/N$, where $\bar{M}$ and σ are the fitted mean and the width of the excess and N is the number of bins in one sigma range. In order to minimize the binning uncertainty, the final mixed-event background spectrum is fitted by a third order polynomial function in a range of $\bar{M}\pm3.0\sigma$. The signal counts S and the background counts B are integrated from the fitted Gaussian and polynomial function. In each signal range, a significance of the signal is calculated according to Eq. 4.10.

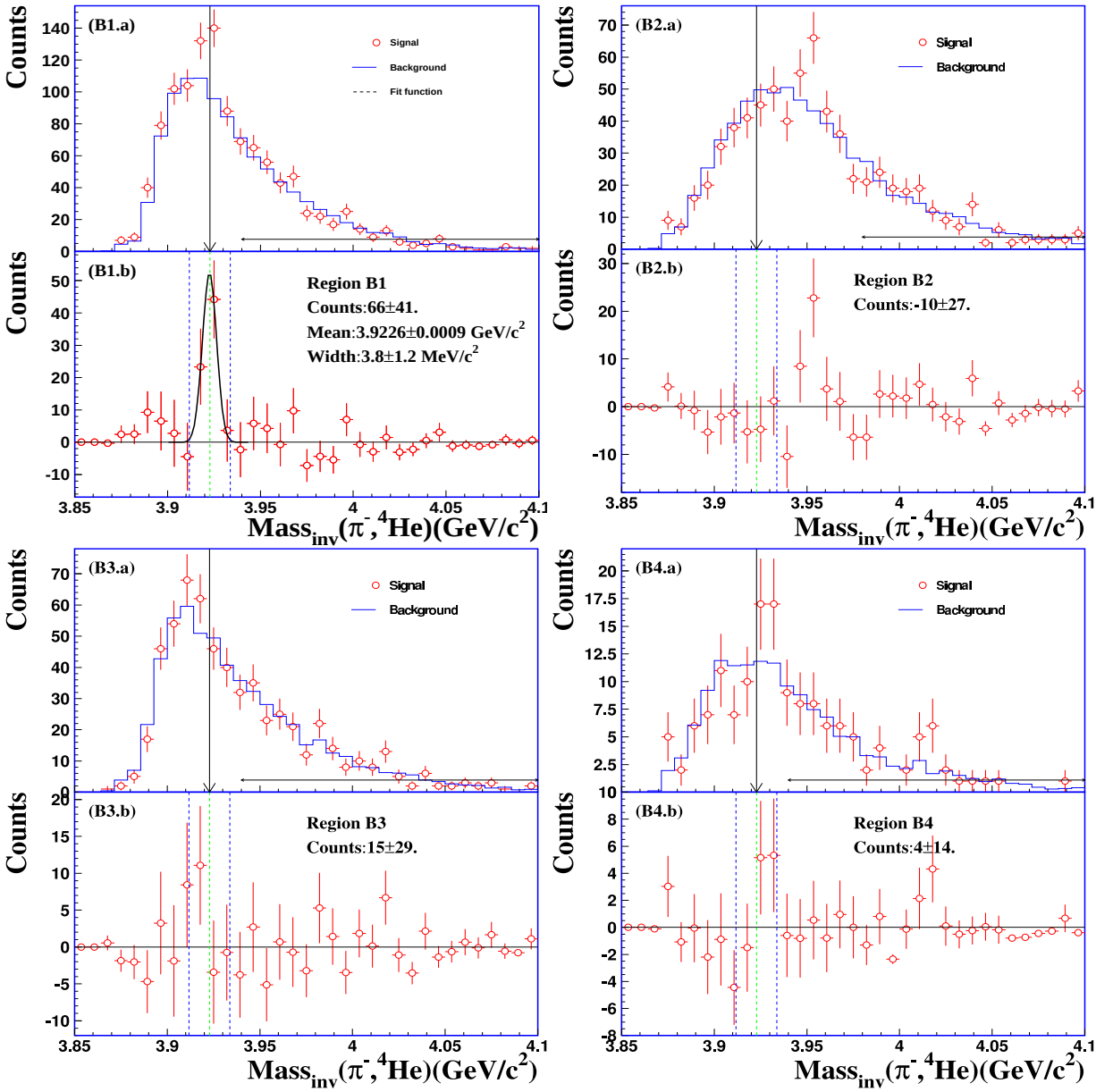

Figure 4.15: Invariant mass distribution of $\pi^- - ^4$He pairs (open circles) and the mixed-event background (solid curve) in the phase space region B1, B2, B3 and B4 are shown in the panels B1(a), B2(a), B3(a) and B4(a), the horizontal arrows depict the normalized regions. Invariant mass distribution after subtracting the normalized mixing-event background are shown in the panels B1(b), B2(b), B3(b) and B4(b), respectively. In the panel B1(b), the excess is fitted by a Gaussian function.

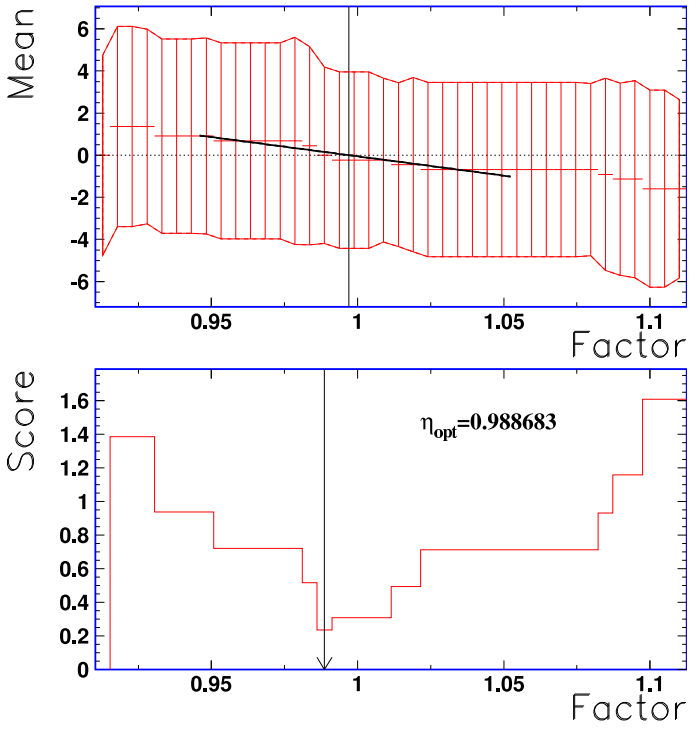

Figure 4.16: Mean and width (error bar) of the counts in the non-signal region as a function of the multiplication factor (upper). Dependence of the score on the multiplication factor (lower).

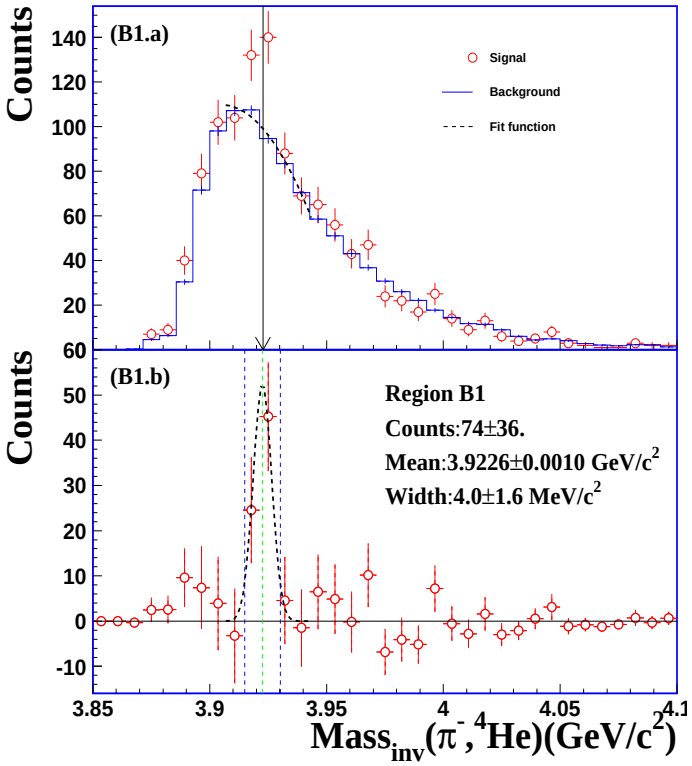

Figure 4.17: Invariant mass spectrum of (π^-,^{4}He) (open circles) and optimized mixed-event background (solid curve) (upper). Invariant mass spectrum after background subtraction (lower), the excess is fitted by a Gaussian function.

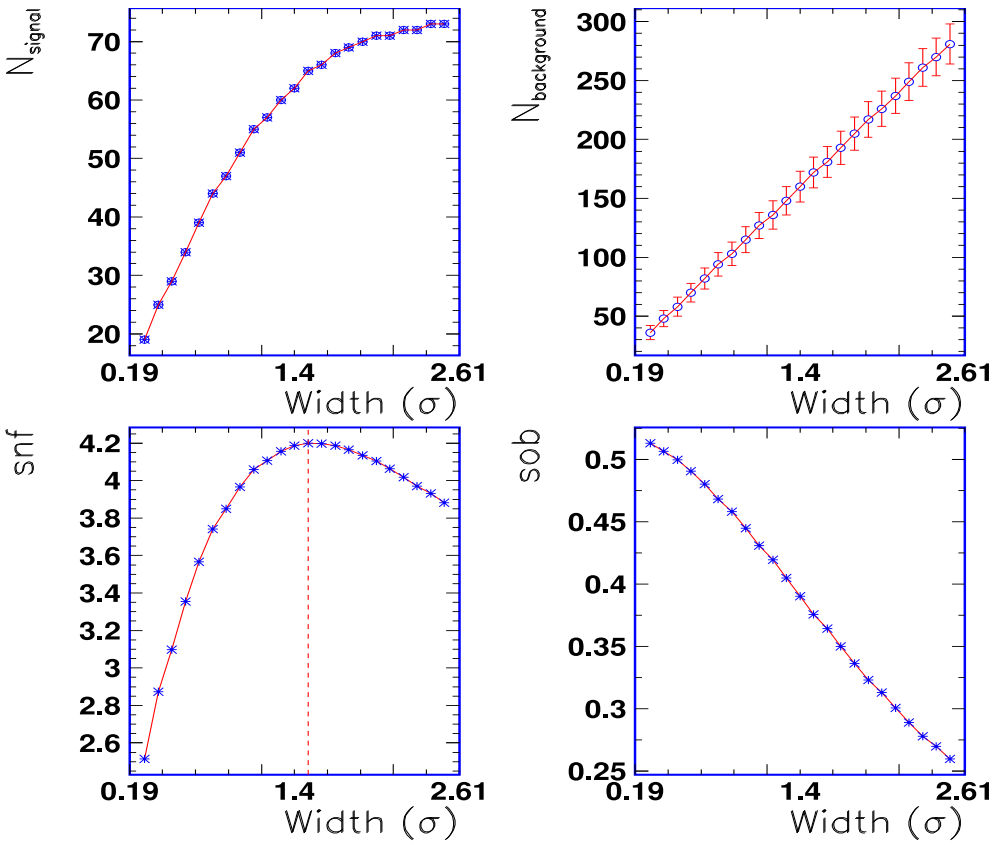

Figure 4.18: Counts of the $^{4}_{\Lambda}$H (upper left) and the background (upper right), significance (lower left) and signal-over-background ratio (SOB) (lower right) as a function of the width of the signal regions, the width is in units of the fitted standard deviation σ.

The integrated counts of $^{4}_{\Lambda}$H (upper left) and the counts of the background (upper right), the significance (lower left) and the signal-over-background (SOB) (lower right) as a function of the width of the signal region are shown in Fig. 4.18. The width of signal region is in units of σ. The number of identified $^{4}_{\Lambda}$H signals saturate at 73. The background counts increase by enlarging the range of the signal region. The significance increases for a small width of the signal regions and it reaches a maximum value of 4.2 for the signal region at $\bar{M}\pm1.5\sigma$. The signal-over-background ratio decreases by opening the signal region.

4.5.4 Production option dependence

The necessity of evaluating the dependence of the final results on the production options has been presented in section 4.4.5. A similar analysis for investigating the dependence of the $^{4}_{\Lambda}$H signal on the production options is made.

The mean and the width (shown by the error bar) of the $^{4}_{\Lambda}$H invariant mass peak (first column) and the significance (second column) as a function of the "shift" option are shown in Fig. 4.19. The significances are obtained within the range of the signal region $\bar{M}\pm1.5\sigma$. The first, second and third row of Fig. 4.19 are obtained with option "rp"=0, 1 and 2,

respectively. In each panel, there are three histograms obtained with the option "vi"=0 (red), 1 (green) and 2 (blue).

The mean and the width of the excesses are quite stable in all kinds of option combinations. The dependence of the significance on various production options is quite similar to the ${}^{3}_{\Lambda}$H case. The results of ${}^{4}_{\Lambda}$H presented in this work are produced under the option combination: "shift"=2,"vi"=1 and "rp"=1.

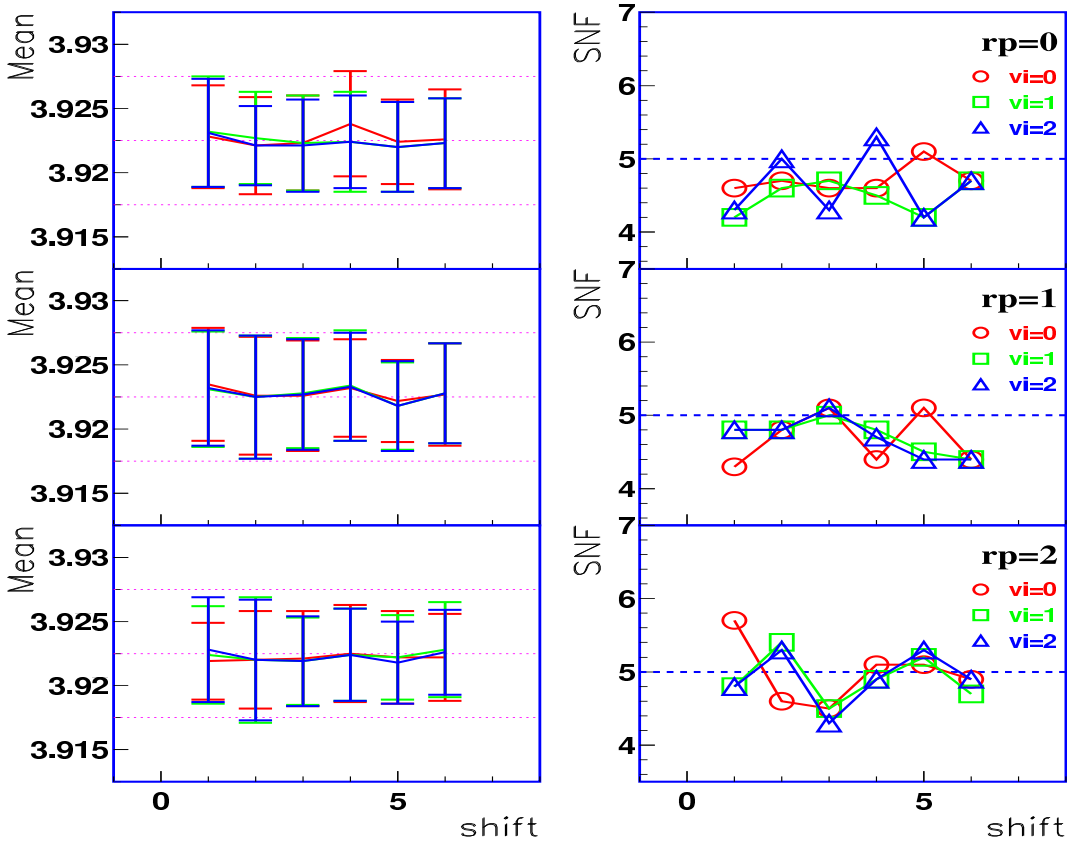

Figure 4.19: Mean and width of the ${}^{4}_{\Lambda}$H signal (first column) and significance (second column) as functions of the "shift" option, *rp*=0 (first raw), 1 (second raw) and 2 (third raw) and vi=0 (red), 1 (green), 2(blue).

4.6 Detected yields of charged particles

Investigating the yield of particles is the most direct way to study reaction and production mechanisms. In HICs, the hypernuclei are produced by secondary processes mostly, which has been discussed in chapter 1. Therefore, comparing the yields of ${}^{3}_{\Lambda}$H and ${}^{4}_{\Lambda}$H to the yields of other relevant particles may give information on how they are produced.

The detected yields of p, d, t, ^{3}He, ^{4}He, Λ hyperon, ${}^{3}_{\Lambda}$H and ${}^{4}_{\Lambda}$H in various phase space regions of the S325e data sample (about 56×10^{6} events) are listed in table 4.10. The signal number of ${}^{3}_{\Lambda}$H and ${}^{4}_{\Lambda}$H in the concerned phase space regions and its statistic error

are listed in the last two columns of table 4.10 as well. The phase space regions A1-A4 (B1-B4), relevant for ${}^{3}_{\Lambda}$H (${}^{4}_{\Lambda}$H) reconstruction, are defined in table 4.5 (4.8). These detected yields have to be corrected by the reconstruction efficiencies, which are obtained by the MC simulation and presented in the next chapter. After the efficiency correction, the yield ratios between the hypernuclei and the relevant particles can be derived. This is discussed in chapter 6.

Table 4.10: Detected yields of p, d, t, ^{3}He, ^{4}He, Λ hyperon, ${}^{3}_{\Lambda}$H and ${}^{4}_{\Lambda}$H in various phase space regions in the $p_t/m - y_{lab}$ plane.

P	Detected yield (phase space region)							
	A1	A2	A3	A4	B1	B2	B3	B4
p	3.8×10^{-1}	5.6×10^{-1}	4.1×10^{-1}	4.7×10^{-1}	3.1×10^{-1}	5.7×10^{-1}	4.1×10^{-1}	4.7×10^{-1}
d	1.4×10^{-1}	1.1×10^{-1}	1.8×10^{-1}	7.7×10^{-2}	1.4×10^{-1}	1.3×10^{-1}	1.8×10^{-1}	7.7×10^{-2}
t	2.3×10^{-2}	1.0×10^{-2}	3.9×10^{-2}	6.3×10^{-3}	3.1×10^{-2}	1.3×10^{-2}	3.9×10^{-2}	6.3×10^{-3}
^{3}He	1.7×10^{-2}	1.0×10^{-2}	1.6×10^{-2}	5.9×10^{-3}	1.5×10^{-2}	1.3×10^{-2}	1.6×10^{-2}	5.9×10^{-3}
^{4}He	4.5×10^{-3}	1.2×10^{-3}	5.4×10^{-3}	7.9×10^{-4}	5.0×10^{-3}	1.8×10^{-3}	5.4×10^{-3}	7.9×10^{-4}
Λ	2.1×10^{-5}	6.8×10^{-5}	1.1×10^{-5}	2.4×10^{-5}	1.6×10^{-5}	6.8×10^{-5}	1.1×10^{-5}	2.4×10^{-5}
${}^{3}_{\Lambda}$H	6.5×10^{-6}	-	-	-	-	-	-	-
${}^{4}_{\Lambda}$H	-	-	-	-	1.3×10^{-6}	-	-	-
${}^{3}_{\Lambda}$H	363±128	-5±79	139±104	63±61	-	-	-	-
${}^{4}_{\Lambda}$H	-	-	-	-	73±36	-22±27	14±29	3±14

Chapter 5

Monte Carlo (MC) simulation

Geant simulation is an indispensable tool in high-energy nuclear experiments to estimate the detection efficiency and to study the feasibility of the physics goals. It can be considered as a virtual experiment with controllable physics inputs and detector responses to correct or to predict the experimental results. The geometrical configuration and the material composition of detectors are described in the Geant environment. All kinds of physics processes like ionization, multiple scattering, hadronic interaction, particle decay and so on can be included. When a particle passes though the detector material, the interaction products entering the active volume of the detector are transformed into detectable signals according to its particular detection mechanism. In order to achieve realistic simulation results, the detector resolution needs be adjusted to a proper level, which is similar to the detector performance during the experiment.

As for the simulation of the FOPI detector, the geometry configuration and the detection response of all sub-detectors are implemented in Geant (version 3.12) [128], which is written in FORTRAN and maintained as a part of CERNLIB [129]. All sub-detectors are described in three dimensions, taking the perspective material composition into account. At the outset of of this chapter, the CDC and the RPC simulation are briefly presented. Following this, the event generator for background events is introduced and these events are analysed in terms of the PID, the Λ hyperon and the background of the channel ${}^{3}_{\Lambda}\mathrm{H} \rightarrow \pi^{-} + {}^{3}\mathrm{He}$. Afterwards, the reconstruction efficiency and the differential decay time efficiency of ${}^{3}_{\Lambda}\mathrm{H}$ and ${}^{4}_{\Lambda}\mathrm{H}$ in the concerned phase space regions are derived, respectively. In the last part, the reconstruction efficiencies of ordinary particles like p, d, t, ${}^{3}\mathrm{He}$ and ${}^{4}\mathrm{He}$ in various phase space regions are presented.

5.1 CDC performance alignment

In Geant, the particles propagate a small distance (call a step) each time until they vanish in the scope of detectors. All of the possible interactions within this "step" are calculated according to the cross section of the relevant physics processes. Technique design of the CDC has been described in section 2.2.3, the most relevant physics process for a drift

chamber is ionization. In each step, hit position and the deposited energy are calculated by Geant.

The CDC digitizer is used to model the processes starting from the ionized electrons in the drift volume up to the final recorded signal. With the hit position, the drift path can be calculated by taking the Lorentz angle into account. Since the mean drift velocity is known, the mean drift time can be determined. When the electrons, ionized from the gas molecules by charged particles, drift to the vicinity of a sense wire, they are amplified by an avalanche process. This amplification is realised by a gain factor in Geant. Pursuant to the z-position of the avalanche, the amplified charge is distributed to both ends of the sense wire. Subsequently, the signal is digitized by the flash-ADC (FADC) and written to a file with the same storage format used for experimental data. A detailed description about the CDC digitizer can be found in [113].

In order to obtain the proper corrections for the experimental results, several parameters used to characterize the CDC performance need to be smeared to a level, such that the physical performance of the CDC during the experiment is reasonably reflected. These parameters are the drift time resolution (equivalent to the position resolution in the transverse plane), the z-position resolution and the energy loss fluctuation. After tuning these parameters, the correlations between these characteristic quantities and a few measured CDC observables obtained from the measured (red) and simulated (blue) data are compared in Fig. 5.1. The distributions in the figure represent the profile of the energy loss resolution $\sigma_{dE/dx}$ (first column), the z-position resolution σ_z (second column) and the transverse position resolution σ_{xy} (third column) of the tracks against their total energy loss dE/dx (first row), polar angle θ (second row), azimuthal angle ϕ (third row), CDC hit multiplicity $HMUL$ (fourth row) and curvature r_c in the transverse plane (fifth row). All charged particles are included in the above correlations. A clear deviation of the σ_z at high hit multiplicity is found, other correlations from experimental data are satisfactorily reproduced by simulated data. This implies that most of the characteristic features of the CDC are well described by the MC software.

5.2 RPC simulation

The geometrical configuration of the RPC super-module and the layout of the single RPC counter have been described in section 2.2.5. The cross-sectional view of a RPC super-module realized in Geant is shown in Fig. 5.2, it contains five RPC counters. In each RPC counter, the red layer corresponds to the sensitive volume, the glass layers are indicated by the light blue boxes and the PVC supports are depicted by the green boxes.

When a charged particle passes through a RPC counter, it ionizes the gas molecules in between the glass layers. The ionised electrons are accelerated by the strong electric field, and they ionize other molecules. Eventually, this develops into an avalanche. The propagation of this electron cloud induces a current on the pickup electrode(s). Since the FOPI RPC counter has a multi-gap configuration, the induced signal is the joint effect from all gaps.

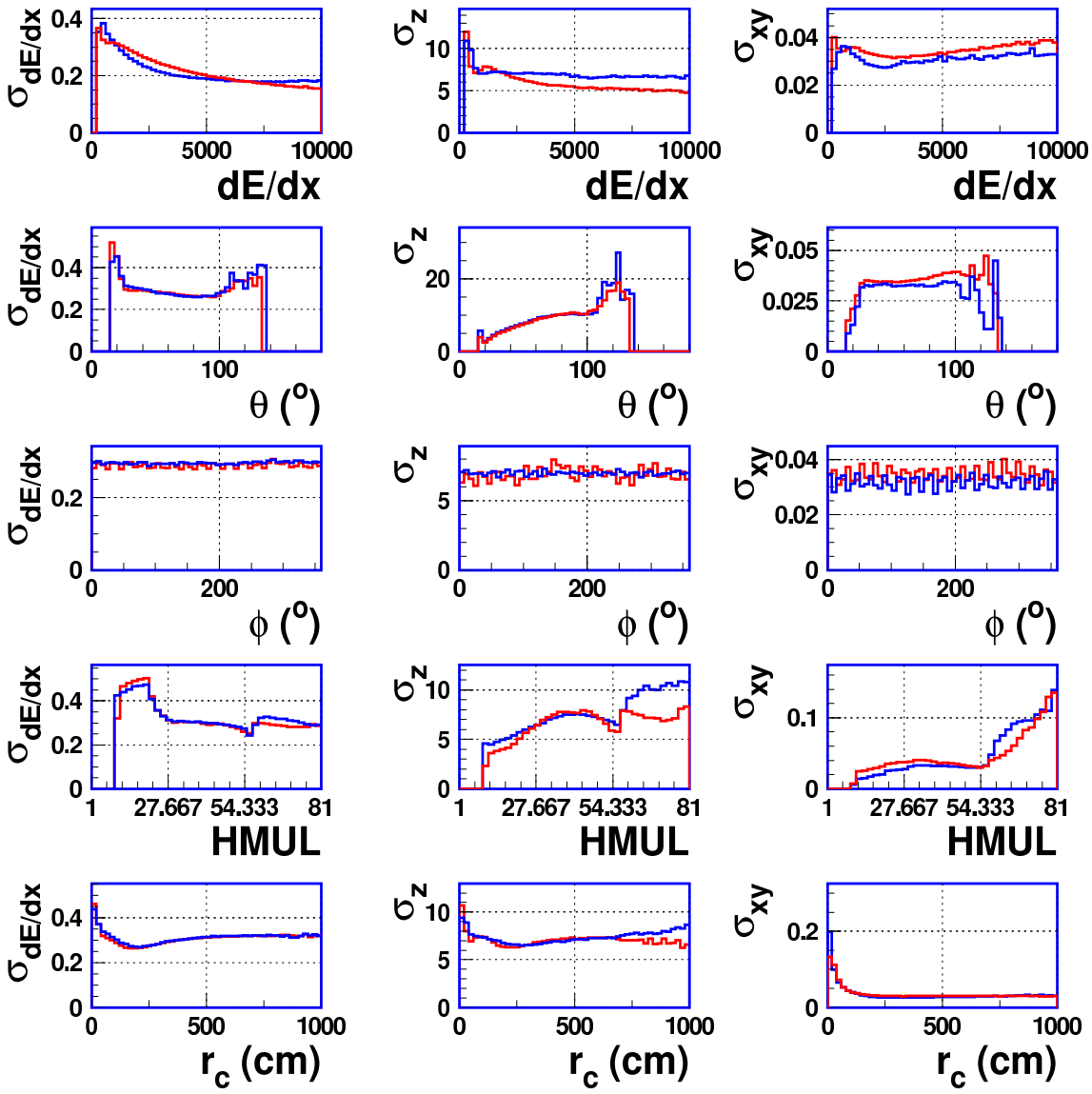

Figure 5.1: Correlations of the characteristic quantities of the CDC from the measured data (red) and simulated data (blue). For detailed descriptions see the text.

In the MC simulation, these complicated processes are simplified by using a scintillator-like layer in the middle of the counter (see Fig. 5.2). When a charged particle traverses this layer, the energy loss, the hit position and the flight time are provided by Geant precisely. The avalanche process is simply modeled by introducing a gain factor. Then, the flight time and the hit position are smeared by a Gaussian distribution with the typical time and position resolution, respectively. The typical time resolution is $\sigma_t = 90$ ps (including the time resolution of the start counter) and the position resolution is $\sigma_t \times v_{signal}$, where v_{signal}=16.5 cm/ns is the propagation velocity of signals in the strip.

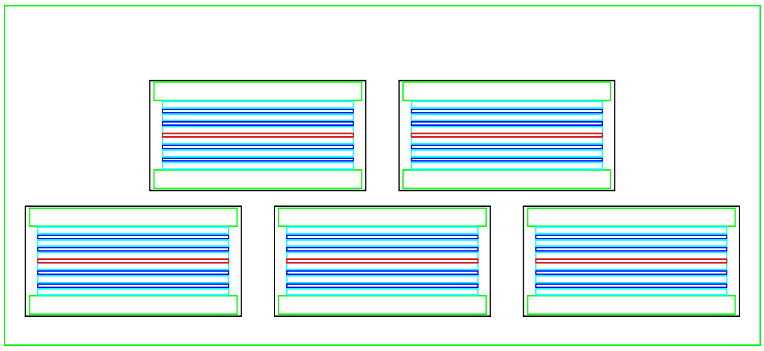

Figure 5.2: Configuration of a RPC super-module realized in Geant, which contains five RPC counters. For detailed descriptions see the text.

5.3 Background events simulation

For reconstructing rare probes like ${}^{3}_{\Lambda}$H and ${}^{4}_{\Lambda}$H, it is necessary to evaluate the selection criteria on the pure background events, because an unphysical resonance could be produced in a massive particle environment as created by HICs, if the selection cuts are over-biased.

In this section, first the components of the background events for the two-body π^--decay of ${}^{3}_{\Lambda}$H and ${}^{4}_{\Lambda}$H are introduced. Secondly, the correlations used for PID of the background events are illustrated. In order to further check the consistency between the experimental and simulated data, the lifetime of the Λ hyperon is extracted from its decay time distribution by applying the differential decay time efficiency obtained from the MC simulation. Afterwards, the selection cuts for ${}^{3}_{\Lambda}$H reconstruction are evaluated on these background events.

5.3.1 Background events generator

The combinatorial background events for the two-body π^--decay of ${}^{3}_{\Lambda}$H and ${}^{4}_{\Lambda}$H, are the accidentally combined π^- and ^{3,4}He produced in Ni+Ni collisions. For the background events, a proper description of the bulk properties of Ni+Ni collisions at 1.91A GeV and the phase space distribution of π^- and ^{3,4}He are essential requirements. Each background event is composed of three components. These are briefly introduced in the following

- An Isospin-dependent Quantum Molecular Dynamics (IQMD) [130] event of Ni+Ni collisions at 1.9A GeV. The IQMD model is one of the most commonly used models to study the reaction kinematics and the bulk properties of HICs, e.g. the collective motion, the particle yields and the phase space distribution of various particles. The version we use in this work contains only light particles, like $\pi^{\pm}$, p, d and a small fraction of t and ^{3}He. They form the body of background events, which provides a massive particle environment.

- A thermal Λ hyperon source. Since the mean lifetime of the Λ hyperon, ${}^{3}_{\Lambda}$H and ${}^{4}_{\Lambda}$H is of the same order, the Λ hyperon is an ideal source to provide the off-vertex π^-. Moreover, as the mean lifetime of the Λ hyperon has been measured to good precision, it can be used as a benchmark to verify how well the MC simulation mimics the experimental setup. Thus, a Λ hyperon, sampled from a Siemens-Rasmussen

distribution [131], is embedded into each IQMD event. The Siemens-Rasmussen distribution is an empirical formula to describe the momentum distribution of particles in a thermal system, which is expressed as

$$\frac{d\sigma}{dp} = (pc)^2 \exp\left(-\gamma\frac{E}{T}\right)\left[\left(\gamma+\frac{T}{E}\right)\frac{\sinh\alpha}{\alpha} - \frac{T}{E}\cosh\alpha\right] \tag{5.1}$$

$$E = \sqrt{(m_0c^2)^2 + (pc)^2}, \quad \gamma = \frac{1}{\sqrt{1-\beta^2}}, \quad \alpha = \frac{\beta\gamma pc}{T},$$

where T is the temperature, β is the expansion velocity, γ is the Lorentz factor associated with β, m_0 is the nominal mass of the Λ hyperon, p is the total momentum and c is the speed of light in vacuum. In this work, the temperature $T = 90$ MeV and the expansion velocity $\beta = 0.3$ are used, in conformity with the published data measured by the FOPI detector in Ni+Ni at 1.93A GeV [106].

- An external ^{3}He and ^{4}He source. As IQMD events do not contain adequate heavy clusters like ^{3}He and ^{4}He, a ^{3}He and a ^{4}He, sampled from a Siemens-Rasmussen-like distribution, are embedded into each IQMD event, separately. For ^{3}He, the chosen temperature and expansion velocity are T=110 MeV and β=0.35, respectively. For ^{4}He, we pick the temperature T=125 MeV and the expansion velocity $\beta = 0.35$. In both of the above distributions, the mean value of y_{lab} is shifted to $y_{lab} = 0.15$. The reason for selecting these parameter combinations is to make a phase space distribution of ^{3}He and ^{4}He, which are similar to the phase space distribution of ^{3}He and ^{4}He in the measured data. Fig. 5.3 shows the distributions of rapidity y_{lab} (left panel) and transverse momentum p_t (right panel) of ^{3}He from measured data (red curve) and simulated data (blue curve) within the RPC acceptance. Each

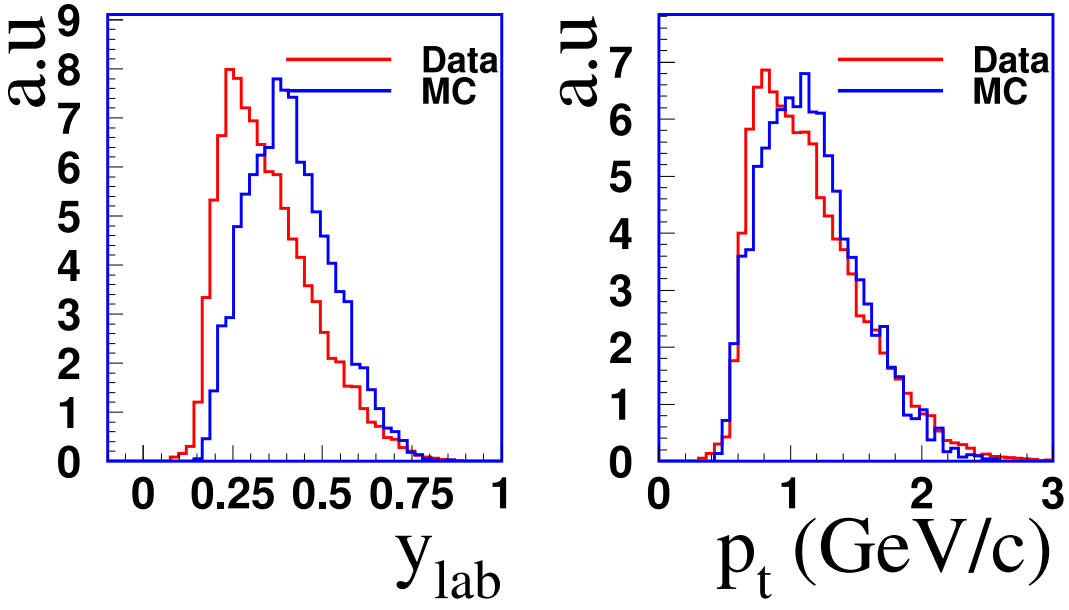

Figure 5.3: Comparisons of y_{lab} (left) and p_t (right) distributions between the measured (red curve) and simulated data (blue curve) within the RPC acceptance.

histogram is normalized by its entries. As shown in the figures, the distribution of rapidity and transverse momentum from measured data are similar to ones from MC data.

5.3.2 PID of simulated events

Filtering the above background events through the Geant package, the trajectories of charged particles are fitted based on the hits left inside the CDC. Like with experimental data, the total energy loss of a track inside the CDC corresponds to the summed dE/dx of all associated drift volumes. Light charged particles can be identified from the correlation of momentum and total energy loss, which is shown in the left panel of Fig. 5.4. The black curves show the parameterized Bethe-Bloch formula for different particle species. The used parameters are the same as those used for experimental data. Heavier particles like t, ^{3}He and ^{4}He can only be identified by combining the measured momentum and the associated velocity provided by the TOF detectors, which is shown in the right panel of Fig. 5.4. The curves represent the formula $p = m\beta\gamma$, where m is adjusted to the desired particle mass.

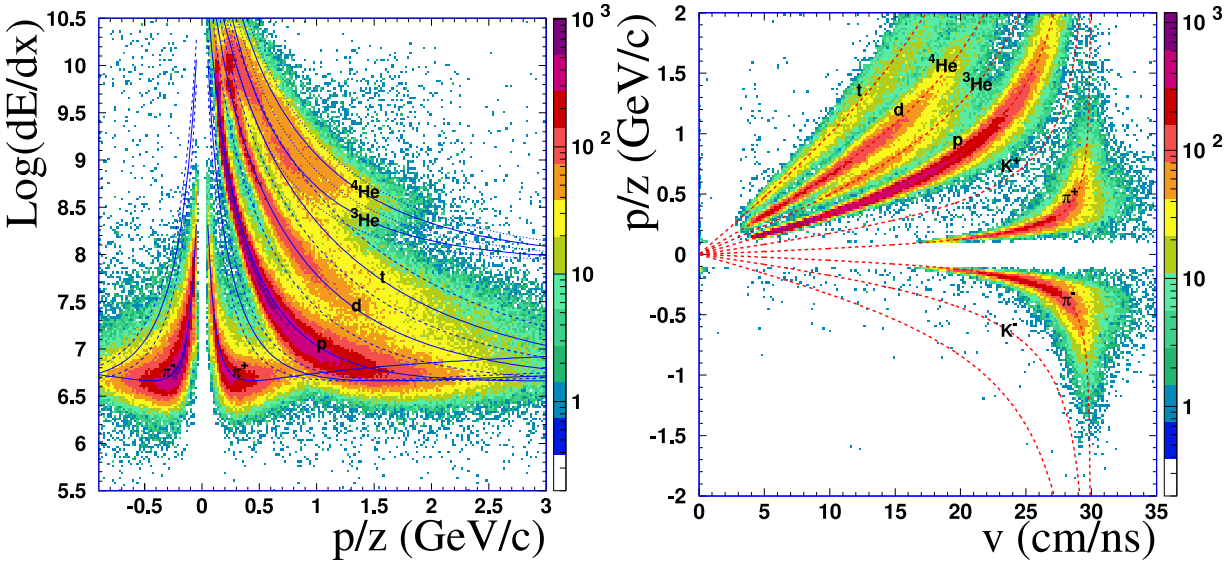

Figure 5.4: Correlation of energy loss and momentum from the MC events (left). Correlation of momentum and velocity (right). For detailed descriptions see the text.

5.3.3 Λ reconstruction

The yield of the Λ hyperon is important to understand the possible production mechanism of the single-Λ hypernuclei in HICs, since the coalescence scenario is one of possible processes to produce such particles. In order to obtain the total yield, the detected yield needs to be corrected, due to the efficiency of selection cuts and the detector acceptance.

In this subsection, first the invariant mass of the Λ hyperon is reconstructed, and its reconstruction efficiencies in various phase regions are obtained. Next, the procedure used to obtain the differential decay time efficiency is presented. By applying this differential efficiency, the mean lifetime of the Λ hyperon is extracted from the decay time distribution.

Λ invariant mass and reconstruction efficiency

The reconstruction procedure for the decay channel $\Lambda \rightarrow \pi^- + p$ has been described in section 4.3. All geometrically correlated (π^-, p) pairs are sought from the input events under the pre-selection cuts. From these events containing a Λ candidate, the mixed events are built with the mixed-event procedure. Applying the selection criteria listed in table 4.4, the invariant mass distribution of the Λ candidates (solid red curve) and the normalized mixed-event invariant mass spectrum (dashed blue curve) are obtained, as shown in the upper panel of Fig. 5.5. The invariant mass spectrum after subtracting the background is presented in the lower panel of Fig. 5.5. The Λ invariant mass peak is fitted by a Gaussian function, with a mean and a width of 1.1164 GeV/c^2 and 4.6 MeV/c^2, respectively. The invariant mass of the Λ hyperon is shifted to the high mass side by about 0.8 MeV/c^2, and the width of the peak is wider than the one from experimental data by about 1 MeV. These effects may be caused by an imperfect description of the azimuthal angle reconstruction in the experimental data by the MC simulation. Although the azimuthal angles in the experimental data are also not perfectly reconstructed, one piece of evidence is that the mean of d_0 distribution of π^- is shifted to the negative side.

The reconstruction efficiency of the Λ hyperon within the RPC acceptance is about 4.5%, which is a ratio between the number of input Λ hyperons within the RPC acceptance and the integrated counts from the final invariant mass spectrum within a 3σ range around the fitted mean. By adding the phase space constraints for the Λ candidates and the input Λ hyperons, the obtained Λ reconstruction efficiencies in the phase space region A1-A4 are 1.6%, 3.1%, 2.5% and 4.5%, and in the phase space region B1-B4 are 1.3%, 2.7%, 2.5% and 4.5%, respectively.

Differential decay time efficiency of Λ

The decay time distribution carries the lifetime information of a particle. The decay time t is calculated by the expression

$$t = \frac{l}{\gamma\beta c}, \qquad \gamma = \frac{1}{\sqrt{1-\beta^2}}, \tag{5.2}$$

where l is the flight distance, γ is the Lorentz factor, β is the particle's velocity in the lab frame and c is the speed of light in vacuum. Regarding the FOPI detector, the decay time can only be calculated from the directly measured quantities in the transverse plane, as only in this plane can one resolve the secondary vertex. Consequently, the decay time t is calculated by

$$t = \frac{r_s}{(\gamma\beta c)_t}, \quad \text{with} \quad (\gamma\beta c)_t = \frac{p_t}{m}. \tag{5.3}$$

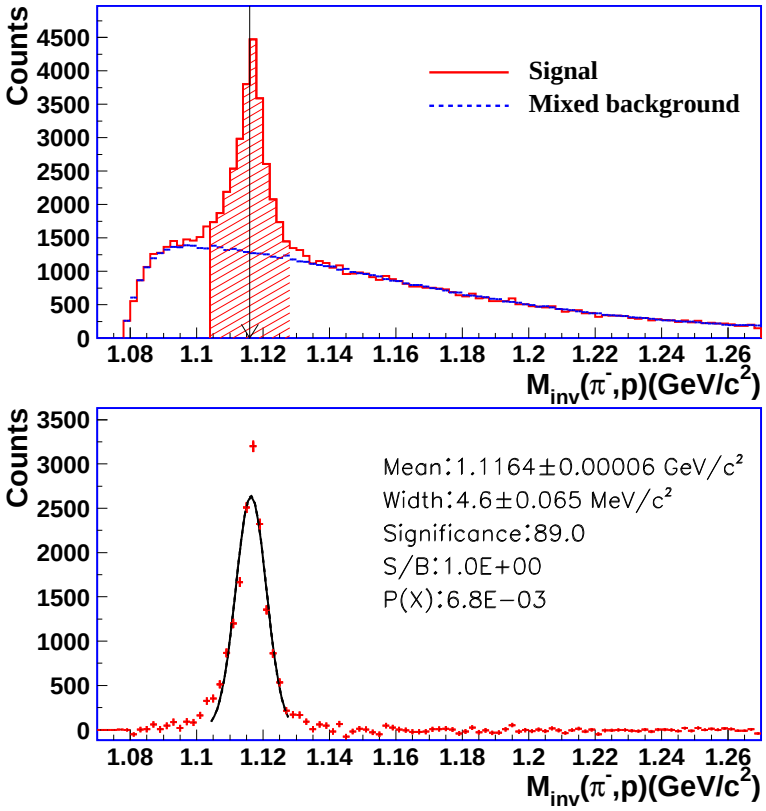

Figure 5.5: Invariant mass spectrum of the Λ hyperon candidates (solid red curve) and normalized mixed-event background (dashed blue curve) (upper). Invariant mass spectrum after background subtraction (lower). The peak is fitted by a Gaussian distribution.

In the above formula, r_s is the distance between the secondary vertex and the primary vertex in the transverse plane, β_t, γ_t, p_t and m are the transverse velocity, the transverse Lorentz factor, the transverse momentum and the nominal mass of the Λ hyperon. Particle decays follows an exponential law, expressed by

$$N(t) = N_0 \cdot \exp\left(-\frac{t}{\tau}\right), \tag{5.4}$$

where τ is the mean lifetime of the particle, N_0 the number of particles at $t = 0$ and $N(t)$ the number of intact particles at a given time t.

Applying the selection cuts listed in table 4.4, the decay time distribution of the Λ candidates (red curve) and the normalized decay time distribution from the mixed events (blue curve) are obtained and plotted in Fig. 5.6(a). After subtracting the background spectrum, the obtained result is shown in Fig. 5.6(b). Since the coordinate of the secondary vertex and the momentum vector of the input Λ hyperons are provided by Geant precisely, their decay time distribution can be obtained based on Eq. 5.3. The corresponding distribution is shown in Fig. 5.6(c). This spectrum is fitted by Eq. 5.4, where N_0 and τ are the free parameters. The exponential function is depicted by a straight black line. The fitted value of τ is 262.8 ± 0.2 ps, which agrees with the input mean lifetime of the Λ hyperon. The Fig. 5.6(d) shows the differential decay time efficiency, which is the ratio of the spectrum in Fig. 5.6(b) and the one in Fig. 5.6(c) bin by bin. The error bars present the statistical error only.

For the S325e experimental data, the spectrum of the decay time (solid red curve) of the

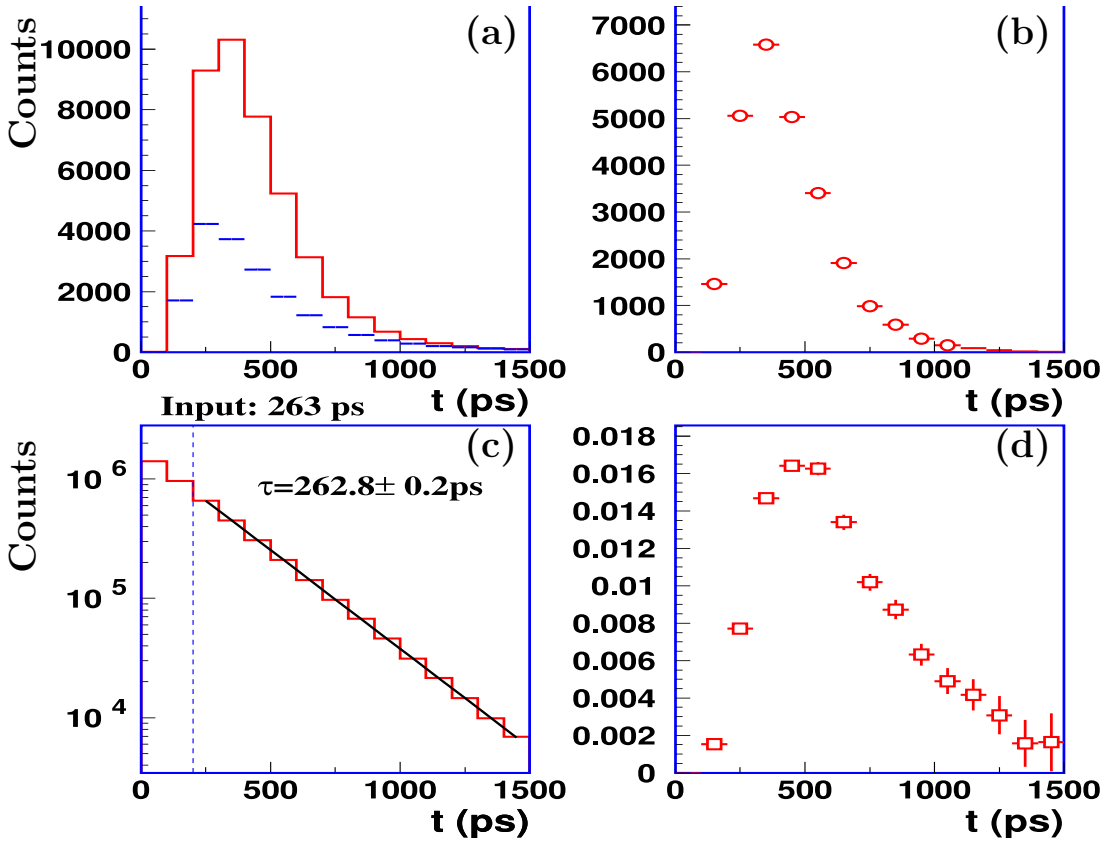

Figure 5.6: (a) Decay time distribution of the Λ candidates (solid red curve) and normalized mixed-event background (dashed blue curve) from MC data. (b) The decay time distribution after subtracting the background spectrum. (c) The decay time distribution of the input Λ hyperons. (d) The differential decay time efficiency.

Λ candidates and the normalized mixed-event background spectrum (dashed blue curve) are depicted in Fig. 5.7(a). The decay time distribution after background subtraction is shown in Fig. 5.7(b). Fig. 5.7(c) is the differential decay time efficiency obtained from the MC simulation, which is the same spectrum displayed in Fig. 5.6(d). The decay time distribution of the Λ hyperon after applying the differential decay time efficiency bin by bin, is shown in Fig. 5.7(d). The spectrum is fitted by Eq. 5.4, the exponential function is depicted by a straight black line. The fitting range is 200-1500 ps. The first nonzero point is excluded from the fit, this is because the ϕ reconstruction of the experimental case is not fully described by the MC simulation (ϕ has a large impact for the small r_s). The extracted slope parameter τ equals 262.3 ± 6 ps, which agrees with the mean lifetime of the Λ hyperon quoted by the PDG [132]. This result once again proves that the performance of the CDC is well described by the MC software.

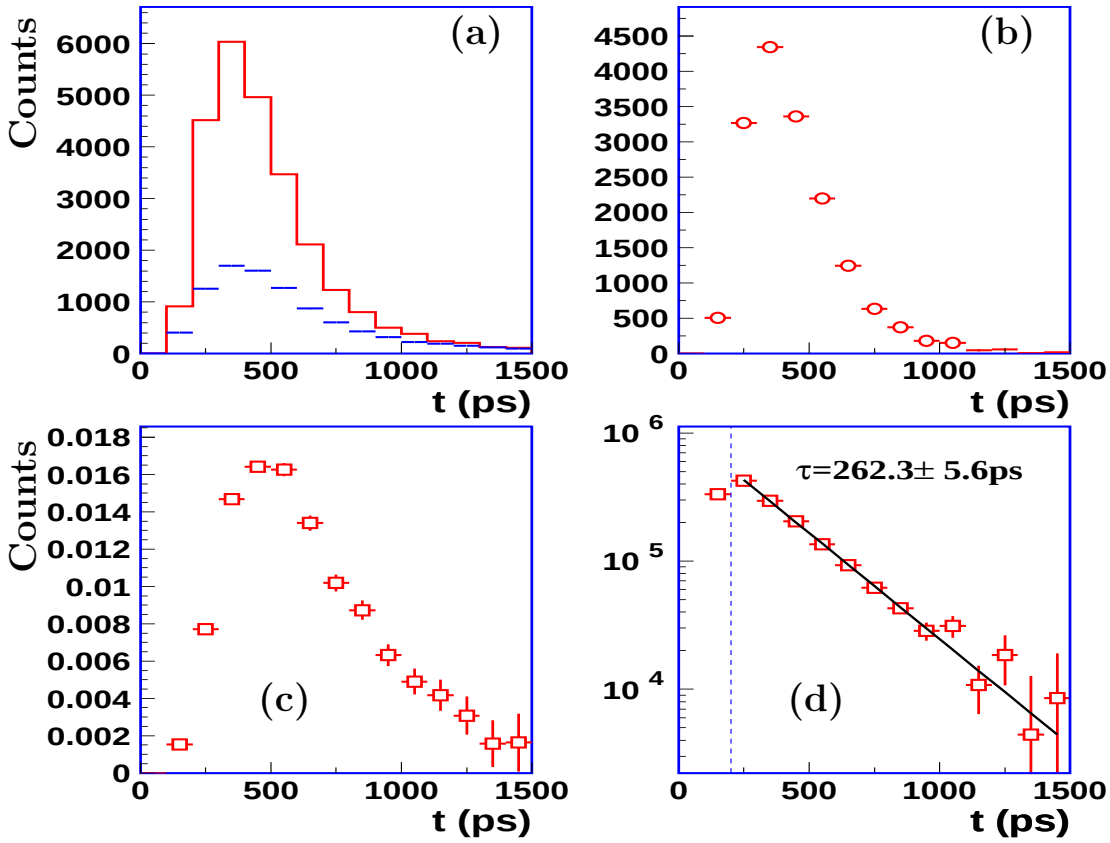

Figure 5.7: (a) Decay time distribution of the Λ candidates (solid red curve) and normalized decay time distribution from the mixed events (dashed blue curve) from the S325e experiment data. (b) Decay time distribution after subtracting the background spectrum. (c) Differential decay time efficiency. (d) The decay time distribution after applying the MC differential decay time efficiency. The straight line is the fitted exponential function, exhibiting a mean lifetime of the Λ hyperon of 262±6.0 ps.

5.3.4 Background simulation for ${}^{3}_{\Lambda}\mathrm{H}\rightarrow\pi^{-}+{}^{3}\mathrm{He}$

Since an unphysical resonance could be produced by over-biased selection cuts in HICs, it is necessary to inspect the outcome of pure background events by applying the very selection criteria used to reconstruct the rare probes like ${}^{3}_{\Lambda}\mathrm{H}$.

The procedures, used to reconstruct ${}^{3}_{\Lambda}\mathrm{H}$, have been presented in section 4.4. For simulated data, the very same analysis is carried out. The geometrically correlated (π^{-},^{3}He) pairs are sought from the input events as well as the mixed events. By applying the selection cuts listed in table 4.6 (in the phase space region A1), the invariant mass distribution of the ${}^{3}_{\Lambda}\mathrm{H}$ candidates (open circles) and the normalized invariant mass spectrum from the mixed events (solid blue line) are obtained and plotted in the upper panel of Fig. 5.8. The normalization region is indicated by a horizontal arrow. Note that a comparable amount of the ${}^{3}_{\Lambda}\mathrm{H}$ candidates are accumulated comparing to the spectrum from the experimental data (see Fig. 4.7(A1.a)). After the background subtraction, the resulting spectrum is

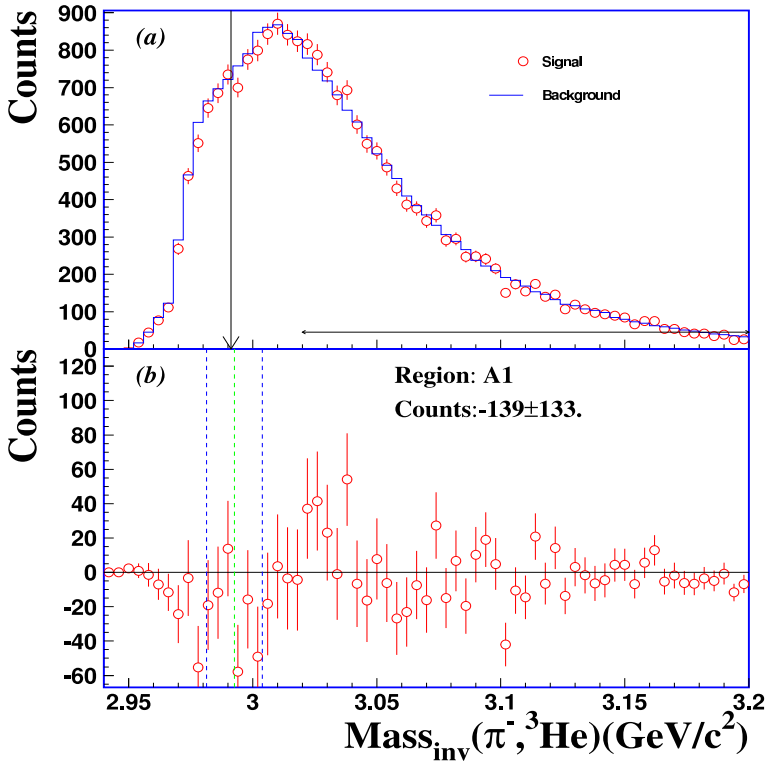

Figure 5.8: Invariant mass spectra of the ${}^{3}_{\Lambda}$H candidates from the background events (open circles) and mixed events (solid curve) in the phase space region A1. The normalization region is indicated by a horizontal arrow (upper). Invariant mass distribution after subtracting the background (lower). For detailed descriptions see the text.

shown in the lower panel of Fig. 5.8. The count in the signal region indicated by two blue vertical dot-dashed lines is -139±133(sta.). No excess is found around the nominal mass of ${}^{3}_{\Lambda}$H. At this level, we can conclude that the selection criteria for ${}^{3}_{\Lambda}$H reconstruction would not produce an unphysical resonance.

5.4 ${}^{3}_{\Lambda}$H→π^-+^{3}He simulation

${}^{3}_{\Lambda}$H is created in Geant with a mass of 2.9912 GeV/c^2 and a mean lifetime of 245 ps, which fully decays into π^- and ^{3}He. Such a ${}^{3}_{\Lambda}$H, sampled from a flat phase space distribution in p_t/m-$y_{\rm lab}$ plane, is embedded into each background event.

In this section, first the reconstruction efficiency of ${}^{3}_{\Lambda}$H in the various phase space regions is derived. Then, the distribution of cut quantities from the experimental data and simulated data are compared. Afterwards, the differential decay time efficiency of ${}^{3}_{\Lambda}$H in the phase space region A1 is obtained.

5.4.1 Reconstruction efficiency of ${}^{3}_{\Lambda}$H

In order to obtain the total yield of ${}^{3}_{\Lambda}$H, the detected yield needs to be corrected due to the detection and reconstruction efficiency. The geometrically correlated (π^-,^{3}He) pairs are sought in the input events and mixed events under the pre-selection cuts, which is the same procedure used to reconstruct ${}^{3}_{\Lambda}$H in the experimental data. By applying the selection criteria listed in table 4.6 (in the phase space region A1), the invariant mass distribution

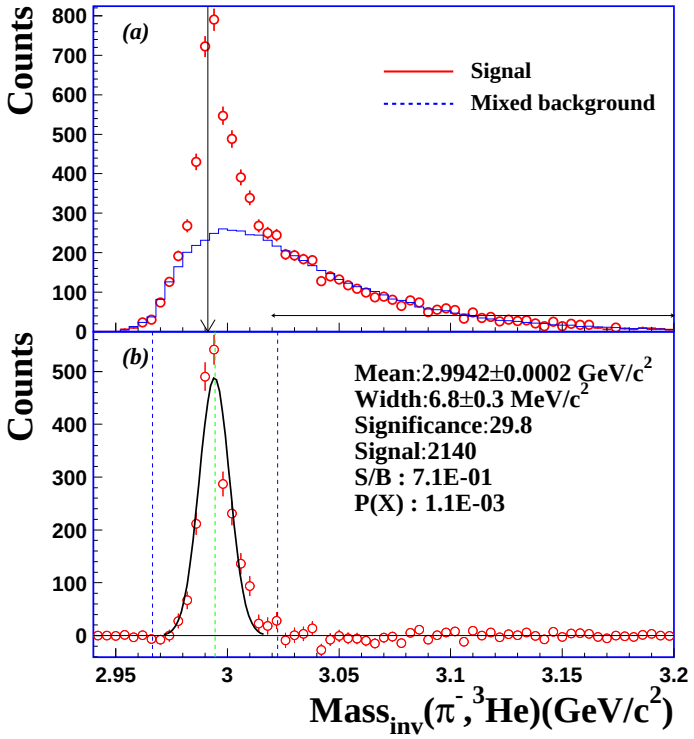

Figure 5.9: Invariant mass spectrum of ${}^{3}_{\Lambda}$H candidates (open circles) and the normalized mixed-event background (solid curve) (upper). The horizontal arrow indicates the normalization region. Invariant mass spectrum after background subtraction (lower), the peak is fitted by a Gaussian function.

of ${}^{3}_{\Lambda}$H candidates (red open circles) and the normalized mixed-event background spectrum (solid blue line) are obtained, drawn in the upper panel of Fig. 5.9. The normalization region is depicted by the horizontal arrow. After subtracting the background spectrum, the resulting spectrum is shown in the lower panel of Fig. 5.9. The peak, around the nominal mass of ${}^{3}_{\Lambda}$H, is fitted by a Gaussian distribution, with a mean of 2.9942 GeV/c^2 and a width of 6.8 MeV/c^2. The mean of the reconstructed ${}^{3}_{\Lambda}$H invariant mass is shifted to the high mass side of about 3 MeV compared to the input ${}^{3}_{\Lambda}$H mass of 2.9913 GeV/c^2. The width of the peak is wider than the one from the experimental data. This may be caused by the imperfect azimuthal angle reconstruction, which is the same effect observed in the Λ hyperon invariant mass reconstruction in the MC data (see section 5.3.3).

The number of reconstructed ${}^{3}_{\Lambda}$H is the integrated counts within the 3σ range around the fitted mean in the final invariant mass spectrum. The reconstruction efficiency of ${}^{3}_{\Lambda}$H is the ratio of identified ${}^{3}_{\Lambda}$H over the number of input ${}^{3}_{\Lambda}$H in a given phase space region. The reconstruction efficiency of ${}^{3}_{\Lambda}$H in the phase space region A1 is about 2.4%. In the same manner, by replacing the constraints of the phase space A1 in table 4.6 to those of other regions, the obtained reconstruction efficiency of ${}^{3}_{\Lambda}$H in the phase space region A2, A3 and A4 is 3.6%, 2.2% and 2.7%, respectively.

5.4.2 Comparison of cut quantities

In order to further inspect the consistency between the experimental data and MC data, the distributions of cut quantities under the selection criteria listed in table 4.6 from measured data and simulated data are compared. In this subsection, the red histograms represent the distributions from measured data, the blue histograms are for the MC data.

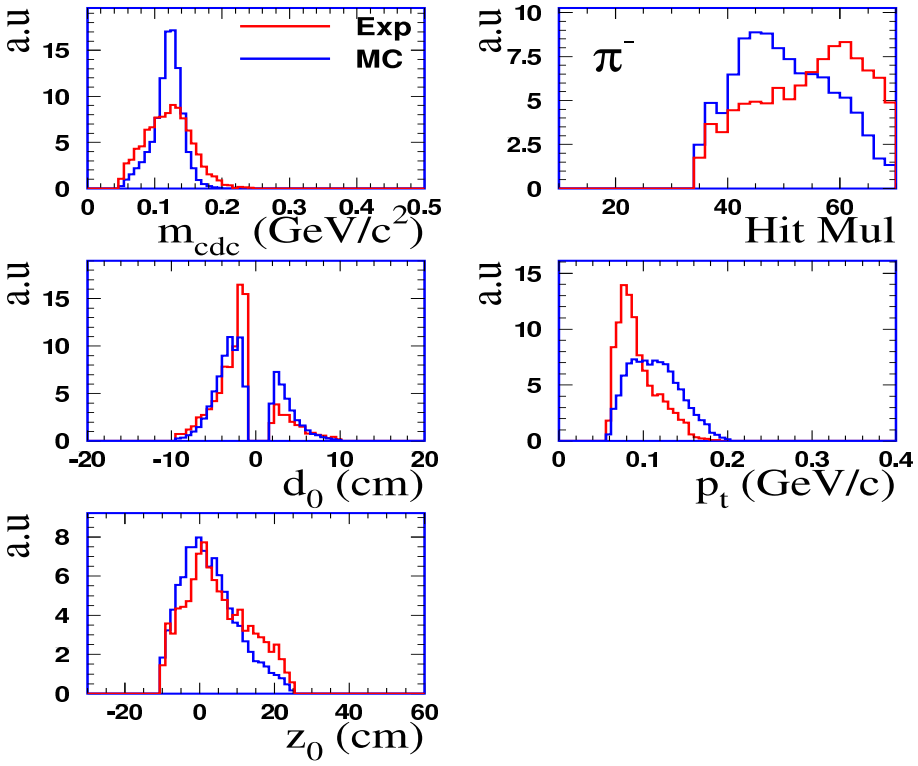

Figure 5.10: Distributions of cut quantities for π^-'s, associated with ${}^{3}_{\Lambda}$H candidates, from the measured data (red curve) and simulated data (blue curve). The concerned quantities are m_{CDC}, $HMUL$, d_0, p_t and z_0. For detailed descriptions see the text.

In order to make a direct comparison, all histograms are normalized by their particular entries.

The distributions of cut quantities for π^-, associated with ${}^{3}_{\Lambda}$H candidates, are shown in Fig. 5.10. The concerned quantities are m_{CDC} (CDC mass), $HMUL$ (CDC hit multiplicity), d_0 (transverse impact parameter), z_0 (intersecting distance of the track and z-axis in the $(r-z)$-plane) and p_t (transverse momentum). The CDC mass resolution of π^- from the simulated data is narrower than the one from the experimental data. This is caused by the imperfect description of the energy loss fluctuation in the simulation. Since the constraints for this quantity are rather loose, this would not lead to a loss of ${}^{3}_{\Lambda}$H detection efficiency. The CDC hit multiplicity of π^- in the measured data is larger than the one in the simulated data, this feature has not been fully understood yet. It is considered as an important source for systematic errors (discussed in chapter 6). The distribution of d_0 and z_0 from the experimental data is in good agreement with the simulated spectrum. The distribution of p_t in MC data is wider than the one from the experimental case. This means the phase space distribution of π^- from the measured data is not fully described by IQMD events.

The distributions of cut quantities for the selected ^{3}He are shown in Fig. 5.11. The concerned quantities are m_{CDC}, $HMUL$, d_0, p_t, z_0, m_{bar} (RPC barrel mass), y_{lab} (rapidity in laboratory frame) and θ (polar angle). The CDC mass distribution of ^{3}He from the

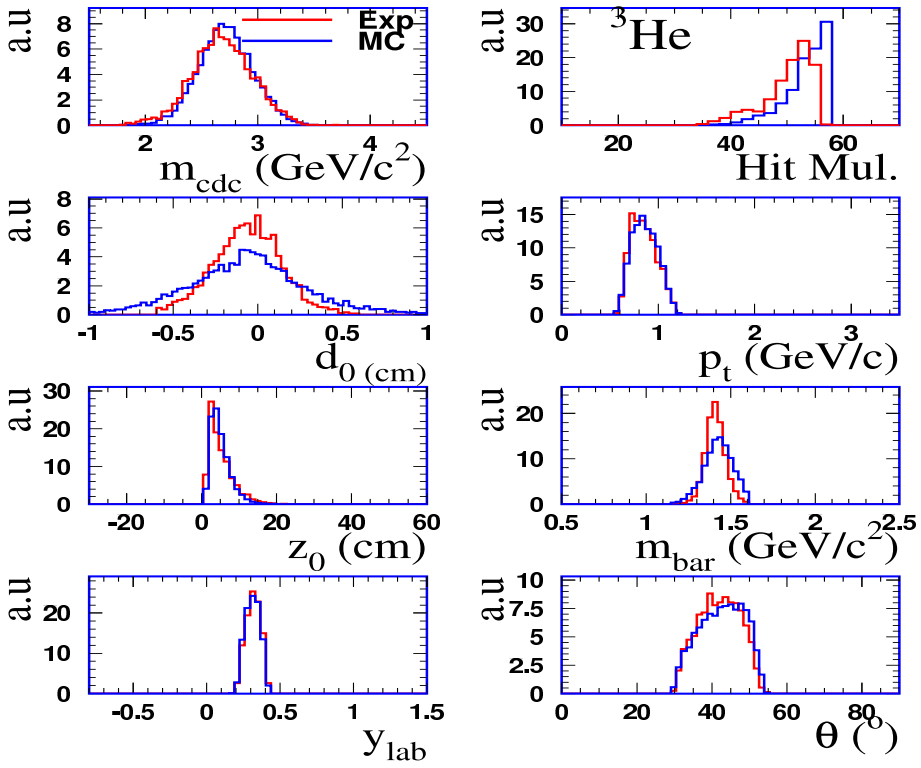

Figure 5.11: Experimental (red) and simulated (blue) spectra of the cut quantities for ^{3}He, which belongs to a $^3_\Lambda$H candidate. Concerned quantities are m_{CDC}, $HMUL$, d_0, p_t, z_0, m_{bar}, y_{lab} and θ, the detailed descriptions see the text.

measured data agrees with the one from the MC data. The tracking hit multiplicity of ^{3}He in the MC data is slightly higher than the experimental one. This may have caused the imperfect description of the energy loss fluctuation. In both case, $HMUL$ is well above the cut limit of 34, this would not reduce the final reconstruction efficiency of $^3_\Lambda$H. The d_0 distribution of ^{3}He in the simulated data is wider than the one in the experimental case. This is because the azimuthal angle resolution of ^{3}He from the MC data is worse than the one in the experimental data, and this is the reason for the relatively wider invariant mass peak of $^3_\Lambda$H in MC data. The distribution of p_t, z_0 and y_{lab} from the measured data is consistent with the corresponding one from the MC data. The RPC mass resolution of ^{3}He in experimental and MC data agree with each other. The polar angle distribution of ^{3}He in the measured data is reproduced by simulated data, since the polar angle of ^{3}He is given by a hit in the RPC barrel which is matched with a CDC track. This implies that the matching between the CDC tracks and the RPC hits is properly realized in the MC simulation.

Distributions of the cut quantities for the $^3_\Lambda$H candidates are shown in Fig. 5.12. The quantities of concern are r_s (distance between the secondary vertex to the primary vertex in the transverse plane), p_t , y_{lab}, d_0, z_s, and $d\phi$ ($\phi_{Hyp} - \phi_s$). Detailed definitions of these quantities are described in section 4.2.2. Distributions of r_s and z_s from the simulated data exceed the corresponding experimental ones for small values of r_s and z_s. Most probably, because the phase space distribution of π^- and/or ^{3}He in the data is not fully

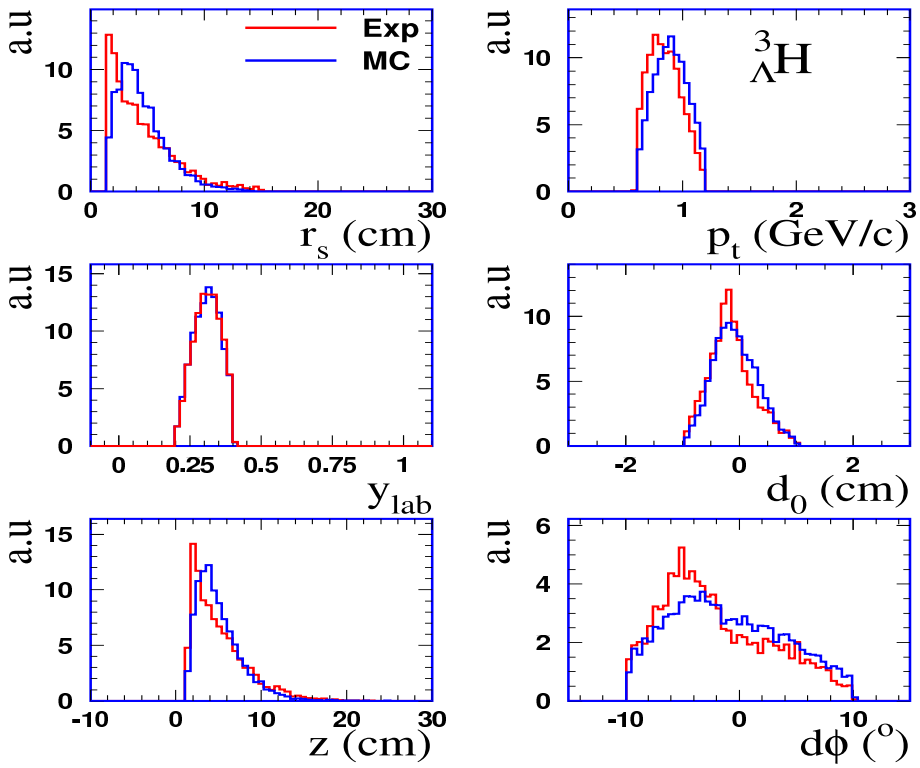

Figure 5.12: Experimental (red curve) and MC (blue curve) distribution of cut quantities for ${}^{3}_{\Lambda}$H candidates. The concerned quantities are r_s, p_t, y_{lab}, d_0, z_0 and $d\phi$. For detailed descriptions see the text.

described by the MC events and more combinatorial pairs were found in the MC data than exist in this data. Since the mixed-event background needs to be extracted from the r_s distribution, this would not influence the final differential decay time efficiency. The distributions of p_t, y_{lab}, d_0, z and $d\phi$ are satisfactorily reproduced by the corresponding distributions from the MC data.

5.4.3 Differential decay time efficiency of ${}^{3}_{\Lambda}$H

The lifetime is one of the most important characteristics for a particle. By applying the differential decay time efficiency spectrum, the mean lifetime of ${}^{3}_{\Lambda}$H can be extracted from its decay time distribution. The procedure for obtaining the differential decay time efficiency has been demonstrated in section 5.3.3. Since the ${}^{3}_{\Lambda}$H signal is only observed in the phase space region A1, the spectra, presented in this subsection, are obtained under the cuts listed in table 4.6.

The decay time of the ${}^{3}_{\Lambda}$H candidates is calculated following Eq. 5.3, where r_s is the corrected distance (arc length) between the secondary vertex and the primary vertex in the transverse plane, m is the nominal mass of ${}^{3}_{\Lambda}$H (2.991 GeV/c^2) and p_t is the transverse momentum. The decay time distribution of ${}^{3}_{\Lambda}$H candidates from the MC events (solid red curve) and the normalized decay time distribution from the mixed events (blue curve)

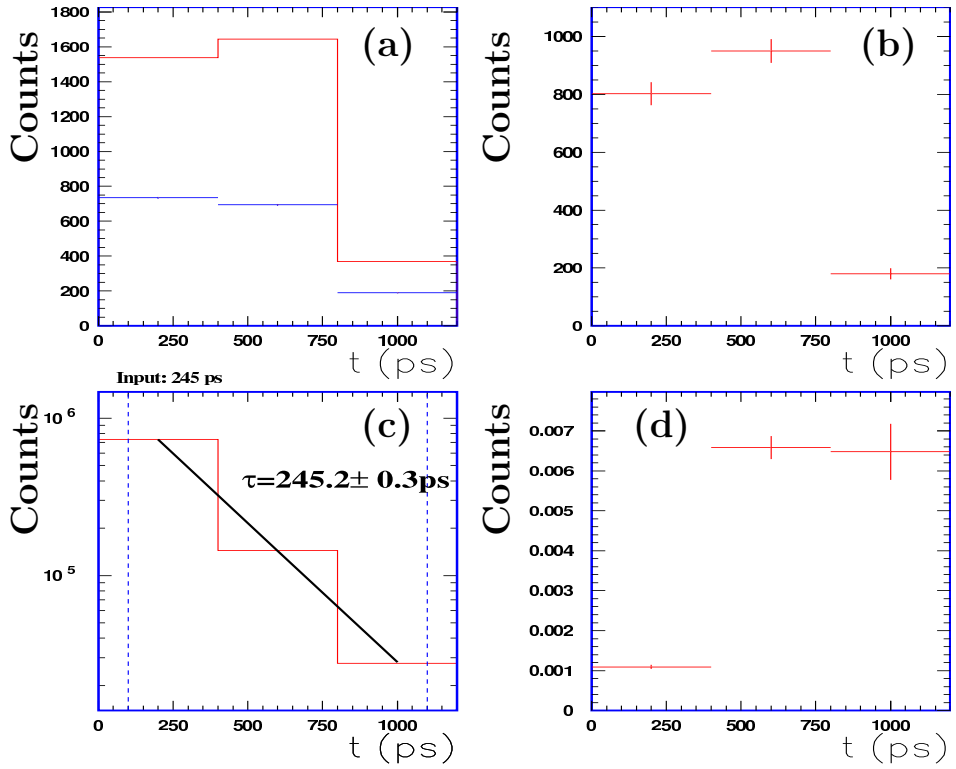

Figure 5.13: (a) The decay time distribution of the ${}^{3}_{\Lambda}$H candidates (solid red curve) and the normalized decay time distribution from the mixed events (dashed blue curve). (b) The decay time distribution after subtracting the mixed-event background. (c) The decay time distribution of the input ${}^{3}_{\Lambda}$H's. (d) The differential decay time efficiency.

are depicted in Fig. 5.13(a). The resulting spectrum after background subtraction is shown in Fig. 5.13(b). The decay time distributions of the input ${}^{3}_{\Lambda}$H, calculated from the flight distance provided by Geant and its momentum, are depicted in Fig. 5.13(c). The spectrum is fitted by Eq. 5.4, shown by a straight black line. The fitted slope parameter τ equals 244.8$\pm$0.2 ps, which agrees with the input value of 245 ps. The differential decay time efficiency of ${}^{3}_{\Lambda}$H is the ratio of Fig. 5.13(b) and Fig. 5.13(c) bin by bin, shown in Fig. 5.13(d), noting that the error bars represent the statistical error only. By applying this differential decay time efficiency, the mean lifetime of ${}^{3}_{\Lambda}$H can be extracted. The result is presented in chapter 6.

5.5 ${}^{4}_{\Lambda}$H$\rightarrow\pi^{-}+{}^{4}$He simulation

The ${}^{4}_{\Lambda}$H is created in the Geant environment with a mass of 3.9228 GeV/c^2 and a lifetime of 245 ps, fully decaying by the two-body π^{-}-decay channel. Like in the ${}^{3}_{\Lambda}$H simulation, a ${}^{4}_{\Lambda}$H, sampled from a flat $p_t/m - y_{\rm lab}$ distribution, is embedded into each background event. In this section, first the reconstruction efficiency of ${}^{4}_{\Lambda}$H in various phase space regions is obtained. Then, the spectra of the cut quantities from the experimental data

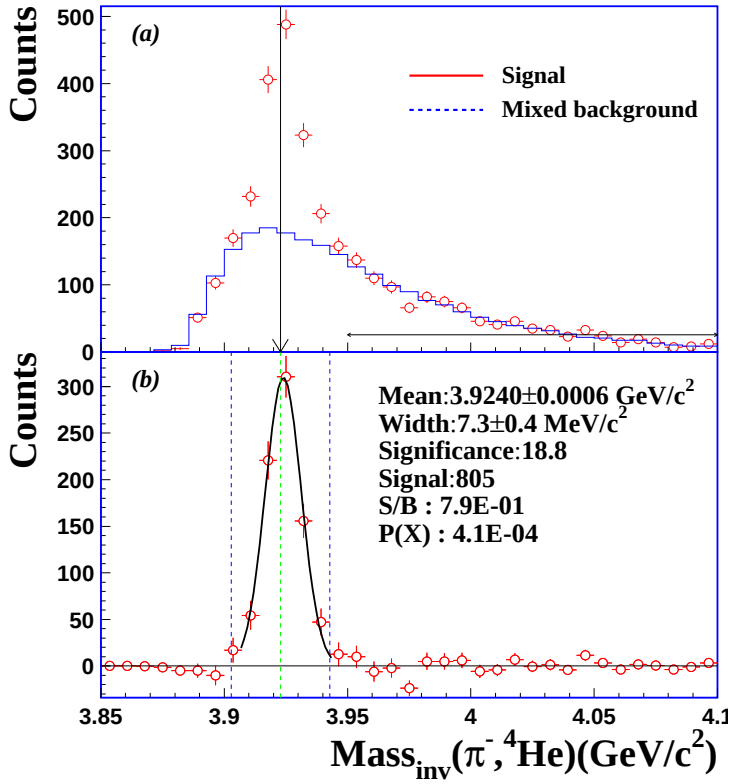

Figure 5.14: Invariant mass distribution of ${}^{4}_{\Lambda}$H candidates (open circle) and normalized mixed-event background spectrum (solid line) from MC events (upper panel). The normalization region is depicted by a horizontal arrow. Resulting invariant mass spectrum after subtracting the background (lower panel). The peak is fitted by a Gaussian distribution.

and simulated data are compared. In the last part, the differential decay time efficiency of ${}^{4}_{\Lambda}$H in the phase space region B1 is derived.

5.5.1 Reconstruction efficiency of ${}^{4}_{\Lambda}$H

The reconstruction procedure for ${}^{4}_{\Lambda}$H has been presented in section 4.5. By applying the selection cuts listed in table 4.9 (in the phase space regions B1), the invariant mass spectrum of the ${}^{4}_{\Lambda}$H candidates (red circles) and the normalized mixed-event background spectrum (solid blue line) in the phase space region B1 are obtained, shown in the upper panel of Fig. 5.14. The spectrum after subtracting the background distribution is depicted in the lower panel of Fig. 5.14. Apart from the ${}^{3}_{\Lambda}$H mass peak, the counts in other regions of the spectrum are almost flat around zero. The peak is fitted by a Gaussian distribution. The obtained mean and width are 3.9240 GeV and 7.0 ± 0.3 MeV, respectively. As in the ${}^{3}_{\Lambda}$H case, the mean is also shifted to the high mass side by about 1.2 MeV, and the width of the peak is also larger than the one observed from the experimental data.

The number of reconstructed ${}^{4}_{\Lambda}$H is the integrated counts in the final invariant mass spectrum in a 3σ range around the fitted mean. The reconstruction efficiency in the region B1 is found to be 1.4%, which is the ratio of the number of identified ${}^{4}_{\Lambda}$H over the number of input ${}^{4}_{\Lambda}$H in the region B1. Similarly, the determined reconstruction efficiencies of ${}^{4}_{\Lambda}$H in the phase space region B2-B4 is 2.0%, 0.6% and 0.7%, respectively. The reason for the relatively low reconstruction efficiency of ${}^{4}_{\Lambda}$H in the phase space region B3 and B4 is not fully understood at the moment.

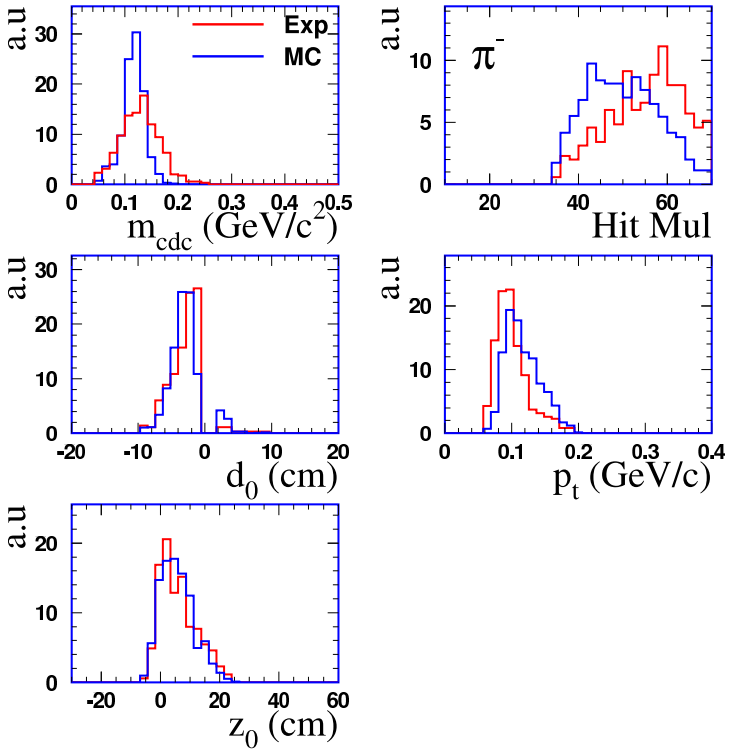

Figure 5.15: Experimental (red curve) and simulated (blue curve) distributions of cut quantities for the π^-, associated with the ${}^{4}_{\Lambda}$H candidates. The quantities of concern are m_{CDC}, $HMUL$, d_0, p_t and z_0.

5.5.2 Comparison of cut quantities

The necessities to compare the spectra of cut quantities between the measured date and simulated data have been presented in section 5.4.2. In this section, the distributions of the cut quantities for selected π^- and ^{4}He, as well as ${}^{4}_{\Lambda}$H candidates from the experimental data (red curve) and MC data (blue curve) are compared. The distributions are obtained under the selection cuts listed in table 4.9 (in the phase space region B1). In order to compare the distributions directly, each spectrum is normalized by its respective number of entries.

The distributions of cut quantities for π^-, associated with the ${}^{4}_{\Lambda}$H candidates, are shown in Fig. 5.15. The concerned quantities are m_{CDC}, $HMUL$, d_0, p_t and z_0. The distributions of π^- from the MC data looks quite similar to those in the ${}^{3}_{\Lambda}$H simulation case. Therefore the conclusions, regarding a comparison of the spectra from the experimental data and simulated data, are the same as those presented in section 5.4.2.

The spectra of cut quantities for the ^{4}He in the selected pairs from the experimental data (red curve) and the simulated data (blue curve) are plotted in Fig. 5.16. The concerned quantities are m_{CDC}, $HMUL$, d_0, p_t, z_0, m_{bar}, y_{lab} and θ. The CDC mass distribution of ^{4}He from the simulated data is comparable with the one from the measured data. The mean $HMUL$ of ^{4}He in simulated data is a bit larger than the one in experimental data. The d_0 distribution from the simulated data is wider than the one from the measured data

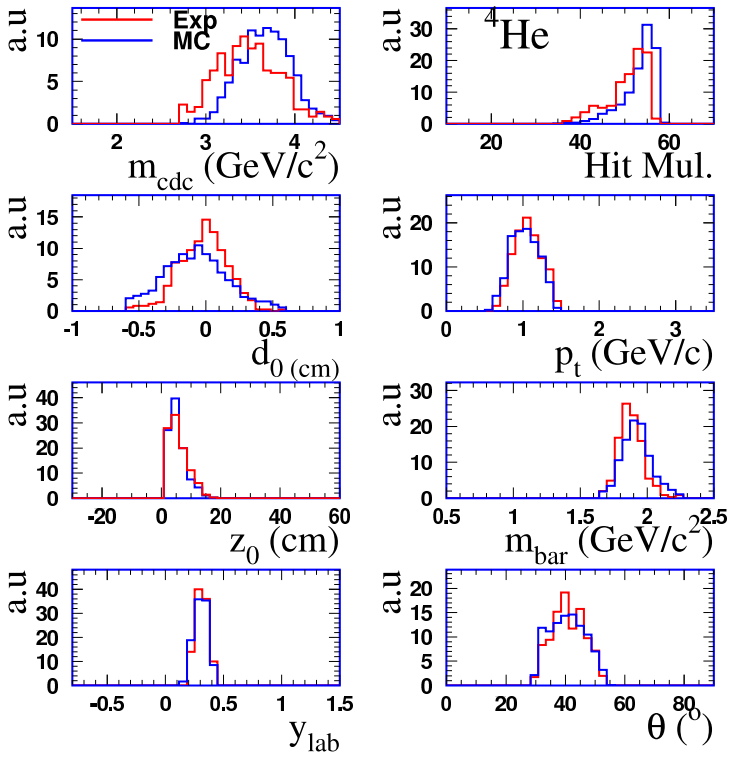

Figure 5.16: Experimental (red curve) and simulated (blue curve) spectra of the cut quantities for ^{4}He from the selected pairs. The concerned quantities are m_{CDC}, $HMUL$, d_0, p_t, z_0, m_{bar}, y_{lab} and θ.

and has a small shift to the negative side. This is due to the imperfect azimuthal angle reconstruction of ^{4}He in MC data. The RPC barrel mass distribution of ^{4}He from the measured and simulated data agrees with each other. The rapidity distribution of ^{4}He in the simulated data is nearly the same as that of the experimental data. The distribution of the polar angle θ from the measured data is well reproduced by the simulated data as well.

The distributions of cut quantities for ${}^{4}_{\Lambda}$H candidates are shown in Fig. 5.17. The concerned quantities are r_s, p_t, y_{lab}, d_0, z and $d\phi$, the meaning of these quantities are the same as those discussed in section 5.4.2. The distribution of r_s and z_s from the simulated data is higher than the corresponding experimental distribution at small r_s and z_s. The reason and the possible influence are quite similar to those discussed in section 5.4.2. The distributions of p_t, y_{lab}, d_0, z_s and $d\phi$ from experimental data are well reproduced by the MC data.

5.5.3 Differential decay time efficiency of ${}^{4}_{\Lambda}$H

The decay time of the ${}^{4}_{\Lambda}$H candidates is calculated by Eq. 5.4. The obtained decay time distribution of the ${}^{4}_{\Lambda}$H candidates (red curve) and the normalized mixed-event background (blue curve) are depicted in Fig. 5.18(a). The decay time distribution after subtracting

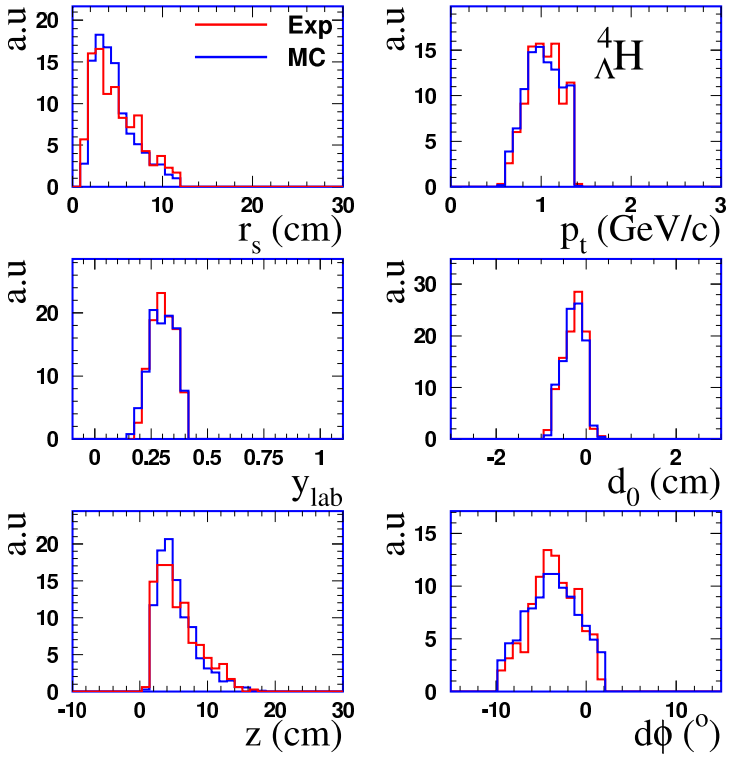

Figure 5.17: Experimental (red curve) and MC (blue curve) distributions of the cut quantities for $^4_\Lambda$H candidates. The concerned quantities are r_s, p_t, y_{lab}, d_0, z_s and $d\phi$. For detailed descriptions see the text.

the background spectrum is shown in Fig. 5.18(b). Fig. 5.18(c) depicts the decay time distribution of the input $^4_\Lambda$H. The distribution is fitted by Eq. 5.4, shown by a straight black line, its slope parameter τ equals to 244 ps, which is consistent with the assigned mean lifetime of the $^4_\Lambda$H in Geant. The differential decay time efficiency is plotted in Fig. 5.18(d), which is the ratio of the reconstructed decay time spectrum (Fig. 5.18(b)) and the one of the input $^4_\Lambda$H's (Fig. 5.18(c)) bin by bin, where the error bars represent the statistical error only.

This differential decay time efficiency can be applied to the experimental decay time spectrum directly. Detailed results of extracting the mean lifetime of $^4_\Lambda$H are presented in next chapter.

5.6 Detection efficiencies of charged particles

Particle yield ratios can provide the information about how hypernuclei are produced in HICs. In order to obtain the absolute yields of charged particles, their detection efficiency have to be applied. The background events (see section 5.3.1), with additional deuteron and triton embedded therein, are filtered through the Geant package and reconstruction routines. The triton and ^{3}He share the same set of parameters, as described in section 5.3.1. The deuteron is sampled from a Siemens-Rasmussen-like (Eq. 5.1) distribution

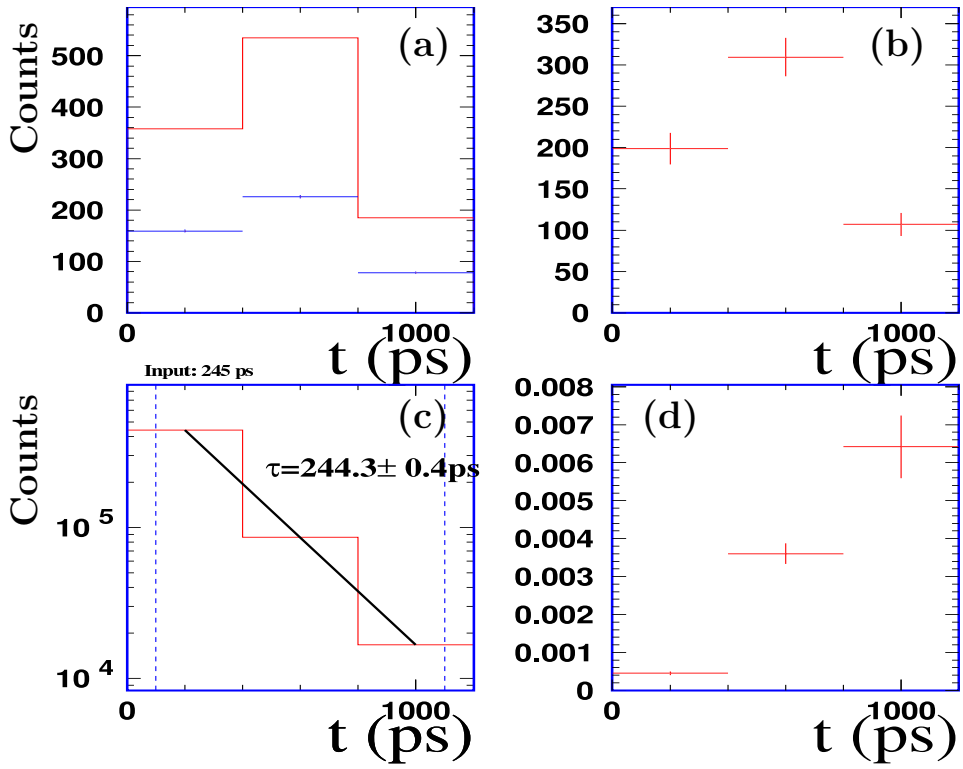

Figure 5.18: (a) Decay time distribution of ${}^{4}_{\Lambda}$H candidates (red curve) and normalized mixed-event background (blue curve). (b) Decay time distribution after subtracting the background spectrum. (c) Input decay time distribution of ${}^{4}_{\Lambda}$H, the straight black line is the fitted exponential function. (d) Differential decay time efficiency of ${}^{4}_{\Lambda}$H.

with T=60 MeV, β=0.3 and the mean of the rapidity distribution is shifted to y=0.15 as well.

The detection efficiency is the ratio between the number of identified particles and the number of corresponding input particles. The selection criteria for those particles are listed in table 5.1. Since the PID of heavy clusters like t, ^{3}He and ^{4}He need the velocity information provided by the TOF detectors, the constraints on the barrel (the PLW and the RPC) mass are essential. The derived detection efficiencies of these particles in the phase space region A1-A4 and B1-B4 are listed in table 5.2. Note that the detection efficiency of triton in the phase space region A2 and B2 are lower than those of other particles in the corresponding phase space region, this needs to be clarified. For completeness, the detection efficiencies of the Λ hyperon, ${}^{3}_{\Lambda}$H and ${}^{4}_{\Lambda}$H in the concerned phase space regions are listed as well.

Table 5.1: Selection cuts for p, d, t, ^{3}He and ^{4}He.

Particle	Charge: Q [e]	m_{CDC} [GeV/c^2]	m_{BAR} [GeV/c^2]
p	$\|Q-1\| < 0.5$	$\|m_{CDC} - 0.94\| < 0.4$	–
d	$\|Q-1\| < 0.5$	$\|m_{CDC} - 1.88\| < 0.4$	–
t	$\|Q-1\| < 0.5$	$1.8 < m_{CDC} < 3.5$	$2.3 < m_{bar} < 3.2$
^{3}He	$Q > 1.5$	$1.8 < m_{CDC} < 3.5$	$2.3 < 2{\cdot}m_{bar} < 3.2$
^{4}He	$Q > 1.5$	$3.2 < m_{CDC} < 4.5$	$3.2 < 2{\cdot}m_{bar} < 4.5$

Table 5.2: Detection efficiency of p, d, t, ^{3}He and ^{4}He in various phase space regions.

Particle	Reconstruction efficiency(%)							
	A1	A2	A3	A4	B1	B2	B3	B4
p	65.9%	66.2%	76.6%	78.8%	54.6%	64.9%	76.6%	78.8%
d	69.0%	60.7%	78.2%	74.1%	67.4%	63.2%	78.2%	74.1%
t	64.8%	38.6%*	76.2%	61.1%	66.9%	43.7%*	76.2%	61.1%
^{3}He	73.5%	71.2%	83.2%	84.6%	63.6%	72.0%	83.2%	84.6%
^{4}He	71.1%	58.8%	75.1%	75.3%	64.6%	62.8%	75.1%	75.3%
Λ	1.6%	3.1%	2.5 %	4.5%	1.3 %	2.7 %	2.5%	4.5%
$^3_\Lambda$H	2.4%	3.6%	2.2%	2.7%	-	-	-	-
$^4_\Lambda$H	-	-	-	-	1.4%	2.0%	0.6%	0.7%

* see the text.

Chapter 6

Results

In the previous chapters, the raw yield and the reconstruction efficiencies of ${}^{3}_{\Lambda}$H, ${}^{4}_{\Lambda}$H, Λ, d, t, ^{3}He and ^{4}He in the various phase space regions were discussed. In this chapter, firstly the total yield or the upper production limit of these particle species in the concerned phase space regions are finalised. In the second part, the systematic error of the yield of ${}^{3}_{\Lambda}$H and ${}^{4}_{\Lambda}$H is estimated. In the third part, the mean lifetime of ${}^{3}_{\Lambda}$H and ${}^{4}_{\Lambda}$H is extracted from the decay time distribution, respectively. In the fourth part, the impact parameter range corresponding to the centrality selections for the ${}^{3}_{\Lambda}$H and ${}^{4}_{\Lambda}$H production in Ni+Ni collisions at 1.91A GeV is discussed. In the last part, the coalescence scenario for the hypernuclei production in HICs is naively discussed and the yield ratio of ${}^{3}_{\Lambda}$H/^{3}He and ${}^{4}_{\Lambda}$H/^{4}He are compared with thermal predictions.

6.1 Yields of particles

As presented in chapter 4, 373±112 (sta.) ${}^{3}_{\Lambda}$H and 73±36 (sta.) ${}^{4}_{\Lambda}$H, are observed in the phase space regions A1 and B1, respectively. After applying the detection efficiency listed in table 5.2, the total yield of ${}^{3}_{\Lambda}$H and ${}^{4}_{\Lambda}$H in the corresponding phase space regions

Table 6.1: Efficiency-corrected yield of ${}^{3}_{\Lambda}$H, ${}^{4}_{\Lambda}$H, Λ, p, d, t, ^{3}He and ^{4}He in various phase space regions.

P	Efficiency-corrected yield							
	A1	A2	A3	A4	B1	B2	B3	B4
p	1.0	1.2	8.5×10^{-1}	9.0×10^{-1}	1.2	1.3	8.5×10^{-1}	9.0×10^{-1}
d	3.3×10^{-1}	3.0×10^{-1}	3.6×10^{-1}	1.8×10^{-1}	3.7×10^{-1}	3.3×10^{-1}	3.6×10^{-1}	1.8×10^{-1}
t	6.6×10^{-2}	6.7×10^{-2}	7.7×10^{-2}	2.0×10^{-2}	8.2×10^{-2}	7.3×10^{-2}	7.7×10^{-2}	2.0×10^{-2}
^{3}He	3.7×10^{-2}	2.0×10^{-2}	2.9×10^{-2}	9.9×10^{-3}	4.4×10^{-2}	2.5×10^{-2}	2.9×10^{-2}	9.9×10^{-3}
^{4}He	1.1×10^{-2}	3.4×10^{-3}	1.2×10^{-2}	1.6×10^{-3}	1.4×10^{-2}	4.6×10^{-3}	1.2×10^{-2}	1.6×10^{-3}
Λ	2.0×10^{-3}	3.4×10^{-3}	6.9×10^{-4}	8.3×10^{-4}	1.9×10^{-3}	3.9×10^{-3}	6.9×10^{-4}	8.3×10^{-4}
${}^{3}_{\Lambda}$H	7.7×10^{-4}	—	—	—	—	—	—	—
${}^{4}_{\Lambda}$H	—	—	—	—	1.3×10^{-4}	—	—	—

are obtained, see table 6.1. The efficiency-corrected yield of the Λ hyperon and other charged particles in various phase space regions is listed in the table as well. The 35% decay branching ratio of ${}^{3}_{\Lambda}$H $\rightarrow\pi^{-}+{}^{3}$He is taken into account, which is averaged from the measured data [119] (see table 4.1) and it has an error of about 5-7%. The 69% decay branching ratio of ${}^{4}_{\Lambda}$H$\rightarrow\pi^{-}+{}^{4}$He is included with a relatively small error of about 2% [118]. For the yields of the Λ hyperon, the 64% decay branching ratio of $\Lambda \rightarrow \pi^{-}$+p is applied. The numbers are normalised to the total event number of the S325e experiment, i.e. 56×10^{6} events.

Since no significant signal of ${}^{3}_{\Lambda}$H (${}^{4}_{\Lambda}$H) is observed in the phase space region A2-A4 (B2-B4), the upper limit of ${}^{3}_{\Lambda}$H and ${}^{4}_{\Lambda}$H production in these regions is estimated. The observed signal counts N_{SIG} and the background counts N_{BCK} in the corresponding signal region (see Fig. 4.7 and 4.15) are listed in table 6.2. In the considered phase space region, the total counts N_{TOT} are the summed value of the signal counts and the background counts, i.e. $N_{TOT} = N_{SIG} + N_{BCK}$, which is assumed to follow a Gaussian distribution (since N_{tot} is a large number). The mean and the variance of the Gaussian distribution are N_{tot} and $\sqrt{N_{tot}}$, respectively. A number N_{CL}, obtained by integrating from $-\infty$ to N_{CL}, equals 95% of the area of the Gaussian distribution. The upper limit of the ${}^{3}_{\Lambda}$H or ${}^{4}_{\Lambda}$H counts $N_{SIg,CI}$ at the 95% confidence level is $N_{SIG,CI} = N_{CI} - N_{BCK}$. As an example, the N_{tot} distribution for estimating the upper limit of the ${}^{3}_{\Lambda}$H signal at the 95% confidence level in the phase space region A2 in the considered signal region (see section 4.4.3) is shown in Fig. 6.1. The dashed vertical line indicates the position of $N_{CL=95\%} = 2509$. The upper limit of the ${}^{3}_{\Lambda}$H production in the phase space region A2 is $N_{{}^{3}_{\Lambda}\mathrm{H}} = N_{CL=95\%} - N_{bck}$=71, under the selection criteria listed in table 4.6 (in the phase space region A2). In the same manner, the upper limit of the ${}^{3}_{\Lambda}$H production in the phase space region A3-A4 and that of the ${}^{4}_{\Lambda}$H production in the phase space region B2-B4 are estimated. The numbers and the corresponding upper limit of the production yields (the reconstruction efficiency and decay branching ratio are included) are listed in table 6.2. In this estimation, the upper yield limit of ${}^{3}_{\Lambda}$H and ${}^{4}_{\Lambda}$H in the phase space region A3 and B3 is close to the corresponding yield in the phase space region A1 and B1, respectively. These suggest that the ${}^{3}_{\Lambda}$H and ${}^{4}_{\Lambda}$H signal may populate the phase space region A3 and B3, but due to the worse detection resolution (mostly from the old plastic barrel), no clear signal could be observed. Beware that the lower detection efficiency of ${}^{4}_{\Lambda}$H in the phase space region A3 is used.

Table 6.2: Upper production limit of ${}^{3}_{\Lambda}$H and ${}^{4}_{\Lambda}$H at 95% confidence level in the phase space region A2-A4 and B2-B4, respectively.

Particle	${}^{3}_{\Lambda}$H			${}^{4}_{\Lambda}$H		
Region	A2	A3	A4	B2	B3	B4
N_{SIG}	-5	139	63	-10	15	4
N_{BCK}	2438	2651	899	184	200	46
$N_{<SIG\|Cl=95\%>}$	71	225.	113.	11.	39.	15.
$Y_{<SIG\|Cl=95\%>}$	1.0E-04	5.2E-04	2.1E-04	1.4E-05	1.7E-04	5.6E-05

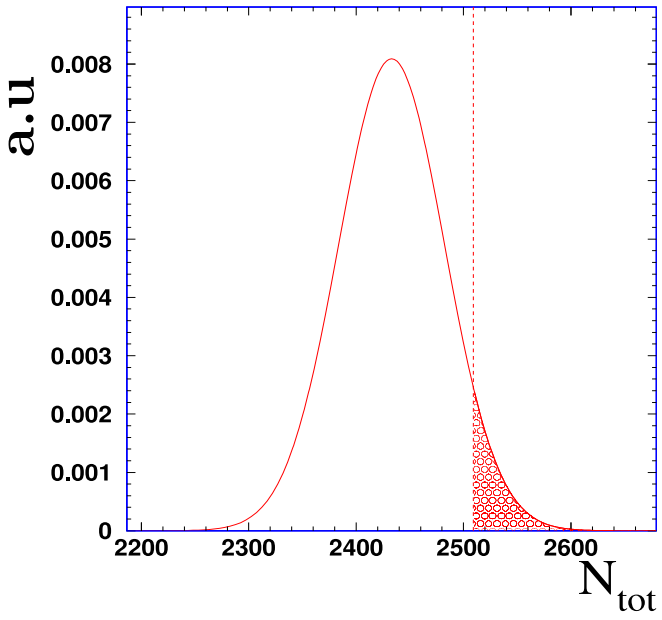

Figure 6.1: Assumed Gaussian distribution of the total counts ($^3_\Lambda$H signal counts plus the background counts) in the phase space region B2. The area from $-\infty$ to the vertical dashed line corresponds to 95% of the distribution.

6.2 Systematic error estimation

The systematic error of the yield of $^3_\Lambda$H and $^4_\Lambda$H is estimated by comparing the number of reconstructed $^3_\Lambda$H and $^4_\Lambda$H in the data and the MC simulation by varying the cut conditions. The critical cut quantities for $^3_\Lambda$H reconstruction are listed in the first column of table 6.3. In the second column, "L" and "U" indicate the variation applied in the lower or upper cut limit of the corresponding quantity. For each concerned cut, the boundary is varied by a value of Δ_+ and Δ_- with respect to the original cut value. The value of Δ_+ and Δ_- for each quantity is listed in table 6.3. In the units column, the σ_{d_0,π^-} is the variance of the d_0 distribution of π^-, it has a value of 0.45 cm. For the other quantities without a clear reference, the cut condition varies by about 10-20%. Among the evaluations, only one cut condition is changed each time, the others are kept the same.

Under each cut variation, a relative change in the number of identified $^3_\Lambda$H is calculated, i.e. $\Delta N_\pm = (N_\pm - N_{ori})/N_{ori}$, where $N_\pm$ is the number of identified $^3_\Lambda$H with the Δ_+ or Δ_- variation, N_{ori} is that under the original selection criteria (listed in table 4.6). For each cut condition, ΔN_+ and ΔN_- can be viewed as a different sample around the original cut condition. The relative change of identified $^3_\Lambda$H under these two variations is their averaged value, i.e. $\Delta N = (\Delta N_+ + \Delta N_-)/2$. Under the same cut variation, a ΔN can be derived from both the experimental data and the simulated data, substituted as Δ_{exp} and Δ_{MC}. Their values are listed in table 6.3. The systematic error contribution of each concerned cut condition is given by $\Delta N_{E-M} = \Delta N_{Exp}$-$\Delta N_{MC}$, which quantifies the matching quality between the experimental data and the MC data. The another systematic error source comes from the normalization factor, which has been discussed in chapter 4. For $^3_\Lambda$H, the error of the normalization factor is about 0.25%. The SOB ratio is about 1/10 for the signal region: mean$\pm 1.5\sigma$ (see Fig. 4.9), this results in about 2.5% relative change of the signal number.

Since the number of identified $^3_\Lambda$H is a common effect from all contributions, the systematic

error of the final yield of ${}^{3}_{\Lambda}$H is the quadratic sum of all contributions. It has a value of about 19%. Finally, the number of identified ${}^{3}_{\Lambda}$H in the phase space region A1 is 363±128(sta.)±87(sys.). The systematic error of the final yield of ${}^{4}_{\Lambda}$H is estimated in the same manner as in the case of ${}^{3}_{\Lambda}$H. The error sources and their contributions are listed in table 6.4. The systematic error for the yield of ${}^{4}_{\Lambda}$H is about 32%. Therefore, the number of identified ${}^{4}_{\Lambda}$H in the phase space region B1 is 73±36 (sta.)±23(sys.).

Table 6.3: Systematic error sources of yield and lifetime of ${}^{3}_{\Lambda}$H.

Variable	edge	Variation			ΔN_{exp}	ΔN_{MC}	ΔN_{E-M}	Δ_τ
		Δ+	Δ-	unit	(%)	(%)	(%)	(ps)
d_{0,π^-}	L	-0.5	0.5	$\sigma_{d_{0,\pi^-}}$	-11.8	0.1	-11.9	21.0
$HMUL_{\pi^-}$	L	2	4	-	-10.0	-6.3	-3.7	-2.0
p_{t,π^-}	L	0.005	0.01	GeV/c	-2.5	-3.3	0.8	25.0
r_s	L	-0.10	0.10	cm	-2.4	0.2	-2.6	15.0
r_s	U	-2.00	2.00	cm	-1.5	0.1	-1.6	-9.0
$p_t/m^\dagger$	L	-0.02	0.02	[c]	-11.0	-0.8	-10.2	10.0
p_t/m †	H	-0.02	0.02	[c]	-1.4	-1.3	-0.1	-2.5
$y_{lab}{}^\dagger$	L	-0.02	0.02	-	-3.1	-0.9	-2.2	-1.5
$y_{lab}{}^\dagger$	U	-0.02	0.02	-	-6.7	-1.3	-5.4	2.0
$PMUL$	L	-3	3	-	-3.1	0.0	-3.1	-2.0
$PMUL$	U	-3	3	-	-5.2	0.0	-5.2	-1.0
$TMUL$	L	-2	2	-	-3.8	0.0	-3.8	16.0
$TMUL$	U	-2	2	-	-2.6	0.0	-2.6	-13.0
η					2.5	-	2.5	-
Total							19.%	44.

† ^{3}He related variables

6.3 Determination of the mean lifetime of ${}^{3}_{\Lambda}$H and ${}^{4}_{\Lambda}$H

The lifetime is one of the most important properties for a particle species. So far, the measured lifetime of ${}^{3}_{\Lambda}$H and ${}^{4}_{\Lambda}$H is of the same order as the lifetime of the Λ hyperon, but both are not precisely measured (see table 4.1). In this section, the mean lifetime of ${}^{3}_{\Lambda}$H and ${}^{4}_{\Lambda}$H is derived from their decay time distribution, and the extracted result is compared to the other measurements, respectively.

6.3.1 The mean lifetime of ${}^{3}_{\Lambda}$H

The procedure used to extract the mean lifetime from the decay time spectrum was demonstrated in section 5.3.3, where the mean lifetime of the Λ hyperon was extracted. The decay times of the ${}^{3}_{\Lambda}$H candidates are calculated with Eq. 5.3, in which r_s is the arc length between the primary vertex and the secondary vertex, p_t represents the transverse momentum of the ${}^{3}_{\Lambda}$H candidate and m is the nominal mass of ${}^{3}_{\Lambda}$H.

Table 6.4: Systematic error sources of yield and lifetime of ${}^{4}_{\Lambda}$H.

Variable	edge	Variation			ΔN_{exp}	ΔN_{MC}	ΔN_{E-M}	Δ_{τ}
		$\Delta+$	$\Delta-$	unit	(%)	(%)	(%)	(ps)
d_{0,π^-}	L	-0.3	0.3	$\sigma_{d_{0,\pi^-}}$	-15.5	0.5	-16.0	5.0
$HMUL_{\pi^-}$	L	2	4	-	-4.9	-6.0	1.1	-0.5
p_{t,π^-}	L	0.005	0.01	GeV/c	-7.0	-1.2	-5.8	-8.0
r_s	L	-0.10	0.10	cm	-7.0	-0.8	-6.2	-14.5
r_s	U	-2.00	2.00	cm	1.4	-1.1	2.5	0.0
$p_t/m^{\dagger}$	L	-0.02	0.02	[c]	0.0	0.0	0.0	0.0
p_t/m †	H	-0.02	0.02	[c]	0.0	0.0	0.0	0.0
$y_{lab}{}^{\dagger}$	L	-0.02	0.02	-	0.0	-0.4	0.4	-0.5
$y_{lab}{}^{\dagger}$	U	-0.02	0.02	-	-7.0	-3.1	-3.9	25.5
$PMUL$	L	-3	3	-	0.7	-4.1	4.8	-2.0
$PMUL$	U	-3	3	-	-4.9	0.7	-5.6	-6.0
$TMUL$	L	-2	2	-	-5.6	-0.3	-5.3	28.5
$TMUL$	U	-2	2	-	-2.1	0.5	-2.6	8.0
η					2.5	-	2.5	-
Total							21.%	43.

† ^{4}He related variables

In the S325e data, under the selection cuts listed in table 4.6 (in the phase space region A1), the decay time distribution of the ${}^{3}_{\Lambda}$H candidates (red line) and the normalized decay time distribution obtained from the mixed events (blue line) are obtained, see Fig. 6.2(a). After subtracting the background spectrum, the decay time spectrum is plotted in Fig. 6.2(b). The differential decay time efficiency of ${}^{3}_{\Lambda}$H obtained from the MC simulation is shown in Fig. 6.2(c). The decay time distribution is corrected bin by bin by the differential efficiency spectrum, and the resulting spectrum is drawn in Fig. 6.2(d). The spectrum is fitted by Eq. 5.4, which is depicted by a straight black line. The extracted lifetime of ${}^{3}_{\Lambda}$H is 263±64 ps.

As a cross check, the flight distance in the z-direction of the ${}^{3}_{\Lambda}$H candidates can be recalculated by $z_s = r_s/\tan(\theta)$, from a known r_s and θ (polar angle). By using an expression similar to Eq. 5.3, the decay time t_z can be derived from the variable z_s and p_z, where p_z is the longitudinal momentum of the ${}^{3}_{\Lambda}$H candidate. Similarly, the total flight distance s in space can be calculated, i.e. $s = \sqrt{r_s^2 + z_z^2}$. The decay time t_s can be derived by using the variables s and p (the total momentum of the ${}^{3}_{\Lambda}$H candidate) as well. The decay time t used in the previous chapters, derived from the variables in the transverse plane, is substituted as t_t. Since the spectrum of t_t, t_z and t_s carries the lifetime information of the same particle species, the extracted results should be consistent with each other.

Fig. 6.3 shows the decay time distributions of t_t (circles), t_z (triangles) and t_s (crosses). Each spectrum is corrected by a corresponding differential efficiency distribution and fitted by an exponential function (Eq. 5.4). The slope parameter extracted from the t_t, t_z and t_s spectrum are 263±64 ps, 245±52 ps and 256±55 ps, respectively. The quoted errors are the statistical errors. The mean lifetimes of ${}^{3}_{\Lambda}$H extracted from the t_t, t_s and t_s

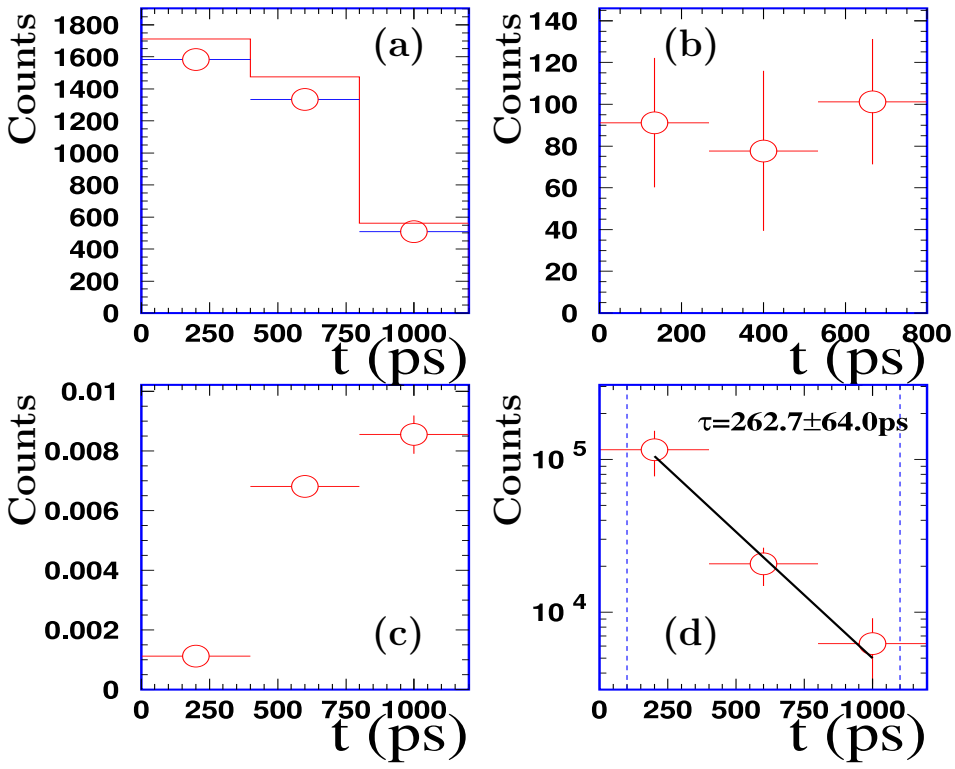

Figure 6.2: (a) Decay time distribution of the ${}^{3}_{\Lambda}$H candidates (solid red line) and normalized mixed event background (open circles). (b) Decay time distribution after subtracting the background spectrum. (c) The differential decay time efficiency. (d) Decay time distribution after the efficiency correction, the straight black line is the fitted exponential function.

distributions are consistent each other within the errors. It implies that the polar angle of the ${}^{3}_{\Lambda}$H candidates assigned from the one corresponding to ^{3}He is a good approximation.

The systematic error of the extracted mean lifetime of ${}^{3}_{\Lambda}$H is estimated by the same procedure as described in section 6.2. Under each cut variation, a mean lifetime is extracted from an efficiency-corrected t_t distribution. Noting that both the decay time spectrum and the differential efficiency spectrum are obtained under the same cut variation. The quantity $\Delta\tau$ listed in table 6.3, is the averaged mean lifetime change under the Δ_+ and Δ_- actions, i.e. $\Delta\tau = (\Delta\tau^- + \Delta\tau^+)/2$, where $\Delta\tau^{\pm} = \tau^{\pm} - \tau_{ori}$, τ^- and τ^+ are the extracted mean lifetime of ${}^{3}_{\Lambda}$H under Δ_- or Δ_+ variation and τ_{ori} is that under the original selection criteria. The systematic error of the mean lifetime of ${}^{3}_{\Lambda}$H is the quadratic sum of all contributions, it has a value of 44 ps. Therefore, the mean lifetime of ${}^{3}_{\Lambda}$H extracted in this work is 263±64(sta.)±44(sys.) ps.

The lifetime of ${}^{3}_{\Lambda}$H was measured by the early emulsion and bubble chamber experiments with large uncertainties. More recently, the lifetime of ${}^{3}_{\Lambda}$H was measured by the STAR [70] and the HypHI [71] collaboration. The uncertainties of these results are comparable to the old measurements. The mean lifetime of ${}^{3}_{\Lambda}$H, extracted from this work, is compatible with other measurements within the margin of error. The measurements are compiled in

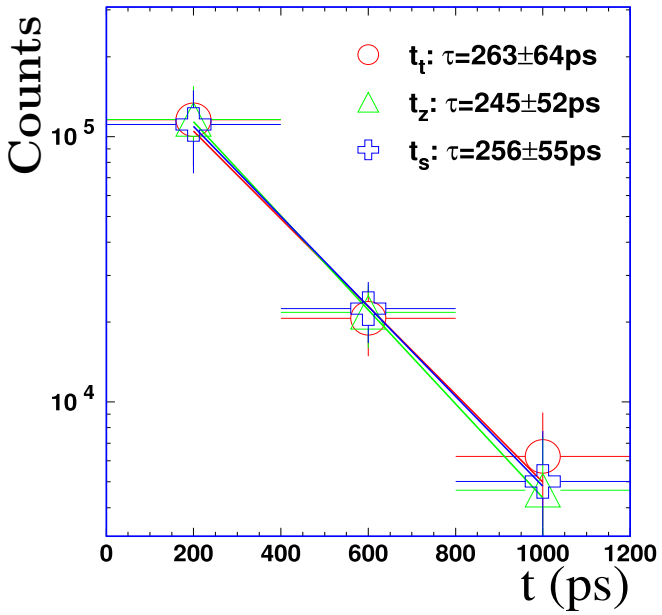

Figure 6.3: Decay time distribution of t_t (circles), t_z (triangles) and t_s (crosses) of identified ${}^{3}_{\Lambda}$H. Lines are the fitted exponential functions.

table 6.5. As a reference, the lifetime of the Λ hyperon is also listed in the last column of table 6.5.

Table 6.5: Compilation of the measured mean lifetimes of ${}^{3}_{\Lambda}$H.

A	τ (ps)	Ref.	Technique
${}^{3}_{\Lambda}$H	90^{+220}_{-40}	[133]	Emulsion
	232^{+45}_{-34}	[134]	Bubble chamber
	285^{+127}_{-105}	[135]	Emulsion
	128^{+35}_{-26}	[136]	Emulsion
	264^{+84}_{-52}	[137]	Bubble chamber
	246^{+62}_{-41}	[119]	Bubble chamber
	191^{+62}_{-41}	[70]	HICs
	231^{+112}_{-75}	[71]	HICs
	263±64±44	This work	HICs
Λ	263±2	[132]	PDG value

6.3.2 The mean lifetime of ${}^{4}_{\Lambda}$H

The procedure for extracting the mean lifetime of ${}^{4}_{\Lambda}$H is the same as the one presented in the previous section. The decay time distribution of t_t (circles), t_z (triangles) and t_s (crosses) of the ${}^{4}_{\Lambda}$H candidates is depicted in Fig. 6.4, respectively. Each distribution is corrected by a corresponding differential efficiency spectrum and fitted by an exponential function (Eq. 5.4). The extracted slope parameter from the t_t, t_z and t_s spectrum is 196±78 ps, 243±110 ps and 247 ±128 ps, respectively. The quoted errors are the statistical error only. The systematic error of the measured mean lifetime of ${}^{4}_{\Lambda}$H is estimated in the same manner as the one in the ${}^{3}_{\Lambda}$H case. The systematic errors contributed by the

considered cut variations are listed in the $\Delta\tau$ column of table 6.4. The systematic error of the mean lifetime of ${}^{4}_{\Lambda}$H is the quadratic sum of all contributions, it has a value of 45 ps. Therefore, the final measured mean lifetime of ${}^{4}_{\Lambda}$H in this work is 196±78(sta.)±43(sys.) ps.

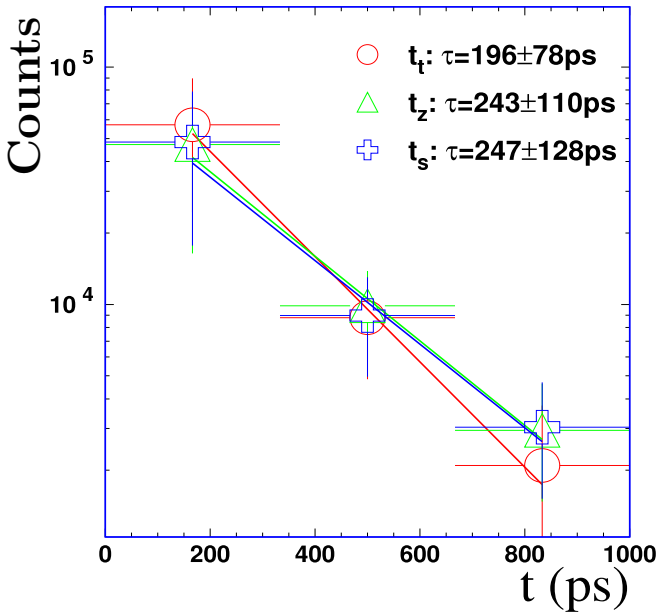

Figure 6.4: Decay time distribution of t_t (circles), t_z (triangles) and t_s (crosses) of ${}^{4}_{\Lambda}$H. Lines are the fitted exponential functions.

The lifetime of ${}^{4}_{\Lambda}$H was measured by the early emulsion and bubble chamber data with large uncertainties as with the lifetime of ${}^{3}_{\Lambda}$H. However the lifetime of ${}^{4}_{\Lambda}$H was better constrained by the K^--stopped experiment at the KEK [138]. The measurement status is compiled in table 6.6. The mean lifetime of ${}^{4}_{\Lambda}$H extracted in this work is compatible with the other measurements within the margin of error.

Table 6.6: Compilation of the measured mean lifetimes of ${}^{4}_{\Lambda}$H.

A	τ (ps)	Ref.	Technique
${}^{4}_{\Lambda}$H	180^{+250}_{-70}	[133]	Bubble chamber
	268^{+166}_{-107}	[139]	Emulsion
	194^{+24}_{-26}	[138]	Stopped K^-
	162^{+99}_{-73}	[71]	HICs
	196±78±43	This work	HICs
Λ	263±2	[132]	PDG value

6.4 Impact parameter range for ${}^{3,4}_{\Lambda}$H production

In the FOPI experiment, the centrality of the collisions is characterized by the CDC track multiplicity $TMUL$ and the PLW hit multiplicity $PMUL$. The distributions of $TMUL$ and $PMUL$ of the S325e experiment are depicted in Fig. 3.1. As mentioned in chapter 3, the dependence of the number of emitted particles in HICs on the impact parameter

can not be expressed in an analytic fashion. However, with a given particle multiplicity range, the corresponding impact parameter range can be estimated by comparing the measured multiplicity to the one given by the transport model calculation. In the model calculation, the dependence of the number of the emitted particles on the impact parameters can be connected. Usually, it is easier to use the impact parameter rather than the measured multiplicity to compare the centrality conditions to the other measurements or the theoretical predictions. Therefore, the impact parameter range, corresponding to the centrality constraints for $TMUL$ and $PMUL$ of ${}^{3}_{\Lambda}\mathrm{H}$ and ${}^{4}_{\Lambda}\mathrm{H}$ production, is discussed via comparing the measured particle multiplicities to the IQMD calculations.

The constraints for $TMUL$ and $PMUL$ are necessary for observing a significant signal of ${}^{3}_{\Lambda}\mathrm{H}$ and ${}^{4}_{\Lambda}\mathrm{H}$. It implies that these hypernuclei are produced in a certain favored impact parameter range. Since $TMUL$ and $PMUL$ are the measured particle multiplicities of the same event in the different solid angle range, a total multiplicity, i.e. $SMUL{=}TMUL + PMUL$, is used in the following discussion.

The impact parameter and the particle multiplicity are known for each IQMD event. Filtering such events through the Geant software and the data analysis routines, the distribution of $SMUL$ is obtained, which is depicted by the blue line in Fig. 6.5(a). The cyan line represents the $SMUL$ distribution of IQMD events with application of the trigger conditions of the S325e experiment, i.e. $PMUL{\geq}5$ and $BMUL{\geq}1$ (the PLB multiplicity) (see section 2.3.2). It is in good agreement with the measured $SMUL$ distribution of the S325e experiment (red), corresponding to about 61% of the most central events. In the figure, the $SMUL$ distribution of the S325e experiment is normalized to that of the IQMD events in a range of $40 < SMUL < 80$. The constrained $SMUL$ distribution for ${}^{3}_{\Lambda}\mathrm{H}$ (green) and ${}^{4}_{\Lambda}\mathrm{H}$ (magenta) production is about 51% and 21% of the S325e events, respectively.

By applying the experimental constraints to the IQMD events, the corresponding impact parameter ranges can be obtained. The impact parameter distribution of IQMD events (blue), IQMD events with the trigger condition of the S325e experiment (cyan) and with the $SMUL$ constraints for ${}^{3}_{\Lambda}\mathrm{H}$ (green) and ${}^{4}_{\Lambda}\mathrm{H}$ (magenta) production are drawn in Fig. 6.5(b).

The mean of the corresponding impact parameter range for ${}^{3}_{\Lambda}\mathrm{H}$ and ${}^{4}_{\Lambda}\mathrm{H}$ production is $\bar{b}_{{}^{3}_{\Lambda}\mathrm{H}}$=3.7 fm and $\bar{b}_{{}^{4}_{\Lambda}\mathrm{H}}$=3.3 fm, respectively, shown by the vertical dashed green and magenta line. Comparing the impact parameter range (up to 9 fm) of Ni+Ni collisions, the favored impact parameter range for ${}^{3}_{\Lambda}\mathrm{H}$ and ${}^{4}_{\Lambda}\mathrm{H}$ production in Ni+Ni collisions lies between the most-central events and semi-central collisions. As a reference, the vertical dotted-dashed line near b=2 fm and b=5.5 fm indicate the upper impact parameter limit of the integrated 5% and 40% of the most central events, respectively.

6.5 Production mechanism discussion

In non-central HICs at SIS18 energies, the particles, like $\pi^{\pm}$, K^{-} and hyperon Λ produced in the fireball, strongly interact with the spectators. In the course of these interactions,

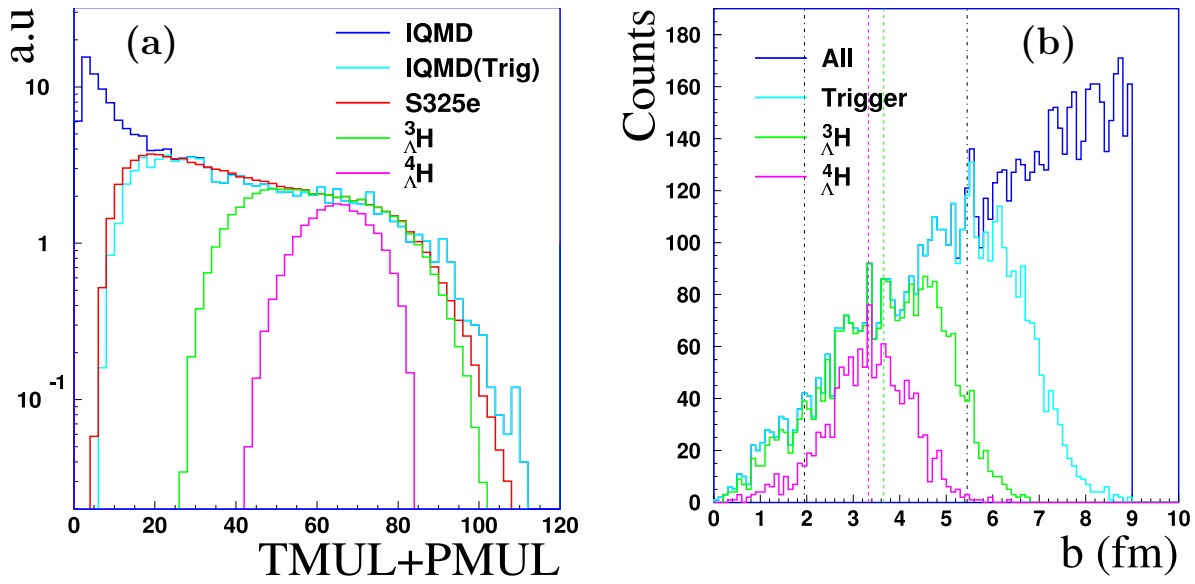

Figure 6.5: (a) $SMUL$ distribution of filtered IQMD events (blue), IQMD events with the trigger conditions of the S325e experiment (cyan), S325e experimental data (red) and the constrained $SMUL$ distribution for $^{3}_{\Lambda}$H (green) and $^{4}_{\Lambda}$H (magenta) production. (b) Impact parameter distribution of IQMD events (red), IQMD events with the trigger conditions of the S325e experiment (cyan) and with $SMUL$ constraints for $^{3}_{\Lambda}$H (green) and $^{4}_{\Lambda}$H (magenta) production.

the hypernuclei can be produced by several scenarios, as discussed in chapter 1 (section 1.2.1). Due to the shortage of available data, the production probability of those processes are unknown so far. In this section, firstly the hypernuclei production via the coalescence process is naively discussed. In the second part, the yield ratios of $^{3}_{\Lambda}$H/^{3}He and $^{4}_{\Lambda}$H/^{4}He are compared with the thermal predictions.

6.5.1 Coalescence scenario

The coalescence scenario for the hypernuclei production in HICs is the earliest and most discussed scenario. Hypernucleus formation by this process can be expressed as $\Lambda + ^{A}X \rightarrow ^{A+1}_{\Lambda}X$, where X is the core nucleus and A is its mass number. From this picture, $^{3}_{\Lambda}$H ($^{4}_{\Lambda}$H) are the coalescent products of the Λ hyperons and the deuterons (tritons). The particles, populated in the same phase space cell in the $p_t/m - y_{\mathrm{lab}}$ plane, have a similar velocity vector. Assuming the particles in the same phase space cell have the same probability to "stick" together during the emission, the production probability of $^{3}_{\Lambda}$H or $^{4}_{\Lambda}$H should be proportional to the production probability of a Λ hyperon and a deuteron or triton, i.e. $Y(^{3}_{\Lambda}\mathrm{H}) \propto Y(\Lambda)\cdot Y(\mathrm{d})$ and $Y(^{4}_{\Lambda}\mathrm{H}) \propto Y(\Lambda)\cdot Y(\mathrm{t})$.

The efficiency-corrected yield of Λ and d(t) in the phase space region A1 (B1) and A2 (B2) is listed in table 6.7. The joint yield of $Y(\Lambda)\cdot Y(\mathrm{d})$ in the phase space region A2 is about 1.5 times higher than that in the phase space region A1. If the above assumption is true, the yield of $^{3}_{\Lambda}$H in the phase space region A2 should be about 1.5 times higher than the one

Table 6.7: Yield of Λ and d(t) in the phase region A1 (B1) and A2 (B2).

Region	Y(Λ)	Y(d)	Region	Y(Λ)	Y(t)
A1	1.3×10^{-3}	3.3×10^{-1}	B1	1.2×10^{-3}	6.6×10^{-2}
A2	2.2×10^{-3}	3.0×10^{-1}	B2	2.3×10^{-3}	6.7×10^{-2}

in the phase space region A1. In other words, more than 500 ${}^{3}_{\Lambda}$H are expected in the phase space region A2, since the detection efficiencies in both regions are comparable. Similarly, the joint yield of the Λ hyperon and triton, i.e. $Y(\Lambda)\cdot Y(\mathrm{t})$ in the phase space region B2 is about 2 times higher than that in the phase space region A1. About 150 ${}^{4}_{\Lambda}$H are expected in the phase space region B2. These naive expectations are not compatible with the experimental observations, i.e. no clear signal of ${}^{3}_{\Lambda}$H and ${}^{4}_{\Lambda}$H is observed in the phase space regions A2 and B2 in the data, respectively.

From these simple estimations, we can not rule out the coalescence scenario for the ${}^{3}_{\Lambda}$H and ${}^{4}_{\Lambda}$H production in Ni+Ni collisions at 1.91A GeV, because the relative positions of the considered particles during the emission are unknown. This means that the assumption made at the beginning of this section may be not valid.

6.5.2 Yield ratios and thermal model predictions

The statistic model is a successful approach to describe the hadron production in HICs with the assumption of the whole system reaching a thermal and chemical equilibrium. In a thermal system with a given temperature and baryon chemical potential, the yield of the conventional particles is only related to their masses. For the yield of clusters with the strangeness in HICs at SIS18 energies, a suppression factor, due to the local strangeness conservation, has to be taken into account. The yield ratios of the particles with similar masses are of particular interest, like the yield ratio of ${}^{3}_{\Lambda}$H and ^{3}He, as well as that of ${}^{4}_{\Lambda}$H and ^{4}He. In the thermal production, the yield ratio of the considered pairs is the same in the whole phase space. Therefore, in the given phase space region, the yield ratios of ${}^{3}_{\Lambda}$H/^{3}He and ${}^{4}_{\Lambda}$H/^{4}He predicted by the thermal model are valid.

The yield ratio of ${}^{3}_{\Lambda}$H/^{3}He (${}^{4}_{\Lambda}$H/^{4}He) in the phase space region A1 (B1) and its upper limit (at the 95% confidence level) in the phase space region A2 (B1) are listed in table 6.8 (table 6.9). The reconstruction efficiencies and the decay branching ratios are included in those numbers, while noting that the yield of ${}^{3}_{\Lambda}$H and ${}^{4}_{\Lambda}$H is normalized to the centrality constrained events, which are about a half and 20% of all S325e events, respectively (see section 6.4). The used yield of ^{3}He and ^{4}He is obtained from the events, which are constrained by the corresponding centrality conditions for ${}^{3}_{\Lambda}$H and ${}^{4}_{\Lambda}$H reconstruction.

The statistic error of the yield ratio of ${}^{3}_{\Lambda}$H/^{3}He in the phase space region A1 is dominated by the statistic error of ${}^{3}_{\Lambda}$H, which is about 35%. Its systematic errors, contributed by ^{3}He, are cancelled out. Therefore, only the contributions from the variables which do not directly relate to ^{3}He (see table 6.3) are taken into account. By taking the 5-7% decay-branching uncertainty of channel ${}^{3}_{\Lambda}\mathrm{H}\rightarrow\pi^{-}+{}^{3}\mathrm{He}$, the systematic error of this yield ratio is about 16%. The yield ratio of ${}^{4}_{\Lambda}$H/^{4}He in the phase space region B1 and the upper limit of

the ratio in the phase space region B2 are listed in table 6.9. The statistical error of this ratio is about 49%, and its systematic error is the quadratic sum of those contributions which do not directly relate to ^{4}He. The total systematic error has a value of 17%. The uncertainty of the decay branch of two-body π^--decay of $^4_\Lambda$H is relatively small with a value of 0.2% (see table 4.1).

Table 6.8: Yield ratio of $^3_\Lambda$H/^{3}He in the phase pace regions A1 and A2.

Region	$^3_\Lambda$H	^{3}He	$^3_\Lambda$H/^{3}He	Error(sta.)	Error(sys.)
A1	1.5×10^{-3}	5.3×10^{-2}	2.9×10^{-2}	35%	15%
A2	$< 2.0 \times 10^{-4}$	3.4×10^{-2}	$< 6.0 \times 10^{-3}$	—	—

Table 6.9: Yield ratio of $^4_\Lambda$H/^{4}He in the phase pace regions B1 and B2.

Region	$^4_\Lambda$H	^{4}He	$^4_\Lambda$H/^{4}He	Error(sta.)	Error(sys.)
B1	6.4×10^{-4}	2.3×10^{-2}	2.8×10^{-2}	49%	20%
B2	$< 6.9 \times 10^{-5}$	1.0×10^{-2}	$< 6.7 \times 10^{-3}$	—	—

These yield ratios are compared to the thermal calculations. Fig. 6.6(a) shows the yield ratio of $^3_\Lambda$H/^{3}He as a function of the baryon chemical potential μ_b. The symbols are the predicted yield ratios for a Ni+Ni system at different temperatures, i.e. $T = 80$ MeV (circles), $T = 70$ MeV (square), $T = 64$ MeV (pentagram) and $T = 60$ MeV (triangles) [140]. The freeze-out parameters are for the HICs at SIS18 energies (see Fig. 1.1). The measured yield ratio of $^3_\Lambda$H/^{3}He in the phase space region A1 is depicted by a black horizontal line, and the cross-hatched-line blue band indicates its statistical error. The upper limit at the 95% confidence level of the ratio $^3_\Lambda$H/^{3}He in the phase space region A2 is indicated by a horizontal red line.

The Fig. 6.6(b) shows the yield ratio $^4_\Lambda$H/^{4}He as a function of the baryon chemical potential. The symbols have the same meaning as those in Fig. 6.6(a). The yield ratio of $^4_\Lambda$H/^{4}He in the phase space region B1 is shown by a black horizontal line, and its statistical error is shown by the cross-hatched-line blue band. The red line is the upper limit of the yield ratio at 95% confidence level of $^4_\Lambda$H/^{4}He in the phase space region B2.

The yield ratio of $^3_\Lambda$H/^{3}He in the phase space region A1 and that of $^4_\Lambda$H/^{4}He in the phase space region B1 can be produced by the thermal prediction with the large temperature and/or the small baryon chemical potential. The upper limit of the yield ratio of $^3_\Lambda$H/^{3}He in the phase space region A2 and that of $^4_\Lambda$H/^{4}He in the phase space region B2 are close to the predictions with the lower temperature and/or the high baryon chemical potential.

Since the phase space region A2 and B2 are closer to the mid-rapidity in Ni+Ni collisions at 1.91A GeV, comparing to the phase space region A1 and B1, intuitively the temperature in the region A2 (B2) should be higher than the one in the phase space region A1 (B1). Therefore, it is not possible to describe these yield ratios by the thermal model at the same time. This implies that thermal predictions are not applicable to hypernuclei production in HICs at SIS energies directly. This may be because the nuclear matter at the regions where the hypernuclei were produced, does not reach thermal and chemical equilibrium.

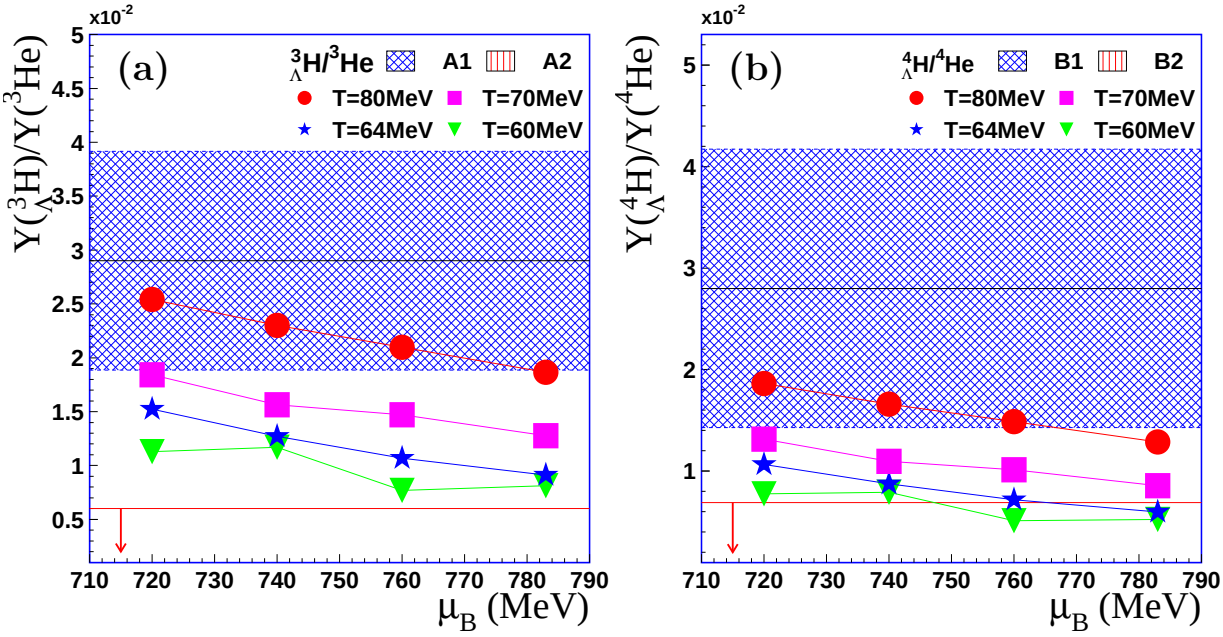

Figure 6.6: Yield ratio of ${}^{3}_{\Lambda}$H/^{3}He (a) and ${}^{4}_{\Lambda}$H/^{4}He (b) as a function of baryon chemical potential μ_b. The blue band is the yield ratio of ${}^{3}_{\Lambda}$H/^{3}He (${}^{4}_{\Lambda}$H/^{4}He) in the phase space region A1 (B1). The red line is the upper limit of the corresponding yield ratio in the phase space region A2 (B2). The symbols are the yield ratios of ${}^{3}_{\Lambda}$H/^{3}He (a) and ${}^{4}_{\Lambda}$H/^{4}He (b) at various temperatures predicted by the thermal model. For detailed descriptions see the text.

Chapter 7

Summary and outlook

A spectacular feature of non-central HICs at SIS18 energies is that the fireball matter strongly interacts with the spectator matter. This feature is vividly illustrated by the collective behaviors of the emitted particles, i.e. the strong sideflow and the out-of-plane elliptic flow. In the course of the interactions between the fireball matter and the spectator matter, the hadrons with the "s" quark, like Λ, Σ and K^- produced in the fireball, may get absorbed by the cold spectator matter. Hadronic matter with special compositions may be created. Hypernuclei and kaonic bound states are possible expectations. Therefore, the HICs in this energy regime provide a unique environment to study the hyperon-nucleon (YN) interaction and the in-medium properties of the kaon. The advantage of HICs for investigating the Λ-hypernuclei is that the produced hypernuclei have relatively large momenta, which can be used to determine the lifetime of the hypernuclei precisely. However, the drawback of HICs is their high background.

In this work, the production of ${}^{3}_{\Lambda}$H and ${}^{4}_{\Lambda}$H in Ni+Ni collisions at a beam energy of 1.91A GeV, performed with the FOPI spectrometer, is investigated. The analysed decay channel to identify ${}^{3}_{\Lambda}$H and ${}^{4}_{\Lambda}$H is their two-body π^--decay channel, i.e. ${}^{3}_{\Lambda}\mathrm{H}\rightarrow\pi^-+{}^{3}\mathrm{He}$ and ${}^{4}_{\Lambda}\mathrm{H}\rightarrow\pi^-+{}^{4}\mathrm{He}$. The ($\pi^-$,^{3}He) and ($\pi^-$,^{4}He) pairs are sought according to geometrical and kinematic constraints. Due to the high particle multiplicity in HICs, most of the selected pairs are accidental combinations. In order to eliminate the combinatorial background, a mixed-event technique is used to reconstruct this background. The full procedure is demonstrated by reconstructing the invariant mass of the Λ hyperons.

For the first time, evidence of ${}^{3}_{\Lambda}$H and ${}^{4}_{\Lambda}$H production in the heavy system at SIS18 energies is obtained from the invariant mass spectrum of (π^-,^{3}He) and (π^-,^{4}He), respectively. However, these signals are only populated in a certain phase space region in the p_t/m-y_{lab} plane. Under a set of stringent geometrical and centrality constraints, about 363$\pm$128(sta.)$\pm$87(sys.) ${}^{3}_{\Lambda}$H are identified in a restricted phase space region (called A1 in the text) from the data sample, which consists of 56×10^6 events covering the most-central 60% of the total reaction cross section. The excess in the final invariant mass spectrum of (π^-,^{3}He) pairs is fitted by a Gaussian function, with a mean of 2.9927$\pm$0.017 GeV/c^2 and a width of 5.6$\pm$1.6 MeV/c^2. Within the margins of error, the reconstructed invariant mass is consistent with the nominal mass of ${}^{3}_{\Lambda}$H. The significance of the excess depends on

the range of the signal region, and it reaches its maximum value of 5.6 within the signal region: $\bar{M}\pm1.5\sigma$. By applying the very same selection criteria in three other phase space regions (called A2, A3 and A4 in the text), no significant signal is observed.

Similarly, about 73±36(sta.)±23(sys.) ${}^{4}_{\Lambda}$H are identified in a certain phase space region (called B1 in the text) with a set of geometrical and centrality constraints. The excess, around the nominal mass of ${}^{4}_{\Lambda}$H, in the final invariant mass spectrum of (π^-,^{4}He) pairs is fitted by a Gaussian distribution, the mean and the width of the excess are 3.9926±0.001 GeV/c^2 and 4.0±1.6 MeV/c^2, respectively. Within the signal region of about $\bar{M} \pm 1.5\sigma$, the significance of the excess reaches its maximum, and it has a value of 4.2. As with the ${}^{3}_{\Lambda}$H case, applying the very same selection cuts in three other phase space regions (called B2, B3 and B4 in the text) in the p_t/m-$y_{\rm lab}$ plane, no significant signal of ${}^{4}_{\Lambda}$H is observed.

The detection efficiency of ${}^{3}_{\Lambda}$H and ${}^{4}_{\Lambda}$H is estimated by a full Geant simulation. ${}^{3}_{\Lambda}$H and ${}^{4}_{\Lambda}$H signals, sampled from a flat distribution in the p_t/m-$y_{\rm lab}$ plane, are embedded into background events. After filtering such events through the Geant package and the reconstruction routines, the detection efficiency of ${}^{3}_{\Lambda}$H in the phase space region A1-A4 is determined to be 2.4%, 3.6%, 2.2% and 2.7%, respectively. That of ${}^{4}_{\Lambda}$H in the phase space region B1-B4 is 1.4%, 2.0%, 0.6% and 0.7%. In order to cross check the consistency between the experimental data and the simulated data, a differential decay time efficiency of the Λ hyperons, obtained from the MC simulation, is applied to the measured decay time spectrum of the Λ hyperons. The extracted mean lifetime of the Λ hyperon is 262 ± 7 ps, which is in good agreement with the PDG value. By applying the similar differential decay time efficiency obtained from the MC simulation, the extracted mean lifetime of ${}^{3}_{\Lambda}$H and ${}^{4}_{\Lambda}$H is 263±64(sta.)±44(sys.) ps and 196±78(sta.)±43(sys.) ps, respectively. Within the error, the values agree with other lifetime measurements available in the literature.

By applying the obtained detection efficiency and its decay branching ratio, the obtained total yields of ${}^{3}_{\Lambda}$H in the phase region A1 and the one of ${}^{4}_{\Lambda}$H in the phase space region B1 are 7.5×10^{-4} and 1.3×10^{-4}, respectively. In the phase space region A2-A4 and B2-B4, the upper production limit of ${}^{3}_{\Lambda}$H and ${}^{4}_{\Lambda}$H at the 95% confidence level is estimated, based on the signal counts and the background counts in the signal region, respectively. From this estimation, we found that the upper limit of the yield of ${}^{3}_{\Lambda}$H and ${}^{4}_{\Lambda}$H in the phase space region A3 and B3 (lower momentum region close to the target rapidity) is close to the corresponding yield in the signal phase space region A1 and B1, respectively. The systematic errors, quoted for the yield and the mean lifetime of ${}^{3}_{\Lambda}$H and ${}^{4}_{\Lambda}$H, are estimated by varying the cut conditions and comparing the variation of results between the experimental data and the simulated data.

The impact parameter range for ${}^{3}_{\Lambda}$H and ${}^{4}_{\Lambda}$H production in Ni+Ni collisions at 1.91A GeV is obtained by comparing the particle multiplicity from the measured data and filtered IQMD events. It is found that the favored impact parameter range for ${}^{3}_{\Lambda}$H and ${}^{4}_{\Lambda}$H production lies between the very central (5%) and the moderately central collisions (40%).

Based on the measured particle yields, the hypernuclei production via the coalescence process is naively discussed. According to the coalescence scenario, the ${}^{3}_{\Lambda}$H (${}^{4}_{\Lambda}$H) are the coalescent products of the Λ hyperons and the deuterons (tritons). Assuming that the

particles, populated in the same phase space cell in the $p_t/m - y_{lab}$ plane (velocity space), have the same probability to "stick" together during the emission. Comparing the yield of Λ and d(t) in the phase space region A1 (B1) and A2 (B2), the number of ${}^{3}_{\Lambda}\mathrm{H}$ in the phase space region A2 and that of ${}^{4}_{\Lambda}\mathrm{H}$ in the phase space region B2 are expected to be about 1.5 times and 2 times higher than the corresponding observation in the phase space region A1 and B1, respectively. These expectations are not compatible with the experimental observations.

Yield ratios of ${}^{3}_{\Lambda}\mathrm{H}/{}^{3}\mathrm{He}$ (${}^{4}_{\Lambda}\mathrm{H}/{}^{4}\mathrm{He}$) in the phase space region A1 (B1) and the upper limit of the ratio in the phase space region A2 (B2) are obtained from those events, constrained by the centrality cuts of the ${}^{3}_{\Lambda}\mathrm{H}$ (${}^{4}_{\Lambda}\mathrm{H}$) reconstruction. These ratios are compared with thermal predictions with various temperatures and baryon chemical potentials. It is found that the yield ratio of ${}^{3}_{\Lambda}\mathrm{H}/{}^{3}\mathrm{He}$ (${}^{4}_{\Lambda}\mathrm{H}/{}^{4}\mathrm{He}$) in the phase space region A1 (B1) can be reproduced by the thermal model with high temperature and/or low baryon chemical potential. The upper limit of the yield ratio of ${}^{3}_{\Lambda}\mathrm{H}/{}^{3}\mathrm{He}$ (${}^{4}_{\Lambda}\mathrm{H}/{}^{4}\mathrm{He}$) in the phase space region A2 (B2) can be described by a thermal calculation as well, but with lower temperature and/or higher baryonic chemical potential. This trend is counterintuitive, since the temperature of the spectator matter is expected to be colder than the one of participate matter. This could be a evidence that the thermal predictions are not directly applicable to hypernuclei production in HICs at SIS energies.

Since the phase space coverage of the current FOPI setup is limited by the detector acceptance, it is possible that the formed hyperclusters populate a wider rapidity range and lower transverse momentum region. This question can be taken up by the future heavy-ion experiment setup, like CBM@FAIR [141], which has an excellent spatial resolution and a high rate capability. It would act as a hypernuclei factory and would allow to investigate the decay branching, lifetime and decay mode of the single-Λ hypernuclei precisely. Meanwhile, investigating the properties of even more rare probes, like the Σ-hypernuclei and double-strangeness hypernuclei, is also possible. More theoretical inputs are necessary for clarifying the mechanism of hypernuclei production in HICs.

Appendix A

The Bethe-Bloch Formula

The mean energy loss of a moderately relativistic charged heavy particle passing through the material is described by the Bethe-Bloch formula [142],

$$-\frac{dE}{dx} = 4\pi N_A r_e^2 m_e c^2 \rho \frac{Z}{A}\frac{z^2}{\beta^2}\left[\frac{1}{2}\ln\left(\frac{2m_e c^2\beta^2\gamma^2 T_{max}}{I^2}\right) - \beta^2 - \frac{\delta(\beta\gamma)}{2}\right] \tag{A.1}$$

where,

N_a:	Avogadro's number = 6.022×10^{23} mol^{-1}
r_e:	Classical electron radius = 2.818 fm
$m_e c^2$:	The mass of electron = 511 keV
Z, A:	Atomic number and atomic mass of absorber
ρ:	Density of absorber
z:	Charge of the incident particle
β:	Velocity of incident particle = v/c, $\gamma = 1/\sqrt{1-\beta^2}$
I:	Mean excitation energy ($\simeq$10 eV)
T_{max}:	The maximum kinetic energy can be imparted to a free electron
$\delta(\beta\gamma)$:	Density effect correction to ionization energy loss

The energy loss -dE/dx is usually given in units of MeV·$g^{-1}cm^2$. The energy loss is related with the velocity of incident particle, but independent of its mass. For a particle with low velocity, the mean energy loss is proportional to $1/\beta^2$, i.e.

$$-\frac{dE}{dx} \propto \frac{z^2}{\beta^2}. \tag{A.2}$$

By correlating the velocities of the charged particles, measured by the TOF detectors (PLW, PLB and RPC) and the dE/dx information measured by the CDC, the charges of the particles can be determined. For the CDC alone, besides the dE/dx information,

the charge scaled momentum p/z is measured. With assuming $z = 1, 2, \cdots$, we have $\beta^2 = p^2/(p^2 + m^2)$. Eq. A.2 can then be rewritten as the following,

$$-\frac{dE}{dx} \propto \frac{z^2}{\beta^2} = z^2 \left(\frac{p^2 + m^2}{p^2} \right) = z^2(1 + \frac{m^2}{p^2}) = z^2 + \frac{m^2}{(p/z)^2}. \tag{A.3}$$

Noting that from the above expression, the mass of the particle is required. Sine the masses of heavy clusters like ^{3,4}He can not be well defined by the CDC alone, their charge can also not be derived precisely.

Appendix B

Kinematic Variables

In relativistic heavy-ion collisions, if the beam is moving along the z direction towards a fixed target, then the center of mass frame moves along the z-direction. For simplicity, in this section units are used in $c = \bar{h} = 1$. For the convenience of transforming the kinematic variables between the laboratory frame and the center of mass frame, instead of the longitudinal velocity $\beta_z = v_z$, the rapidity y is defined by the total energy E and the longitudinal momentum p_z, i.e.

$$y = \frac{1}{2}\ln\left(\frac{E + p_z}{E - p_z}\right) = \tanh^{-1}\beta_z. \tag{B.1}$$

Although this variable depends on the reference frame, it shows a very convenient behaviour under a Lorentz transformation. Namely, the rapidity can be used like a number to calculate the final result. For example, a particle with rapidity y in laboratory frame, which needs to be transformed into the center-of-mass frame with the y_{cm} relative to the lab frame, the rapidity of the particle in center-of-mass frame is $y' = y - y_{cm}$.

Initially, there is no energy in the transverse plane, the transverse momentum p_t is invariant under a Lorentz transformation along the beam direction. A variable called the transverse mass is defined by the transverse momentum and the mass,

$$m_t = \sqrt{p_t^2 + m^2}. \tag{B.2}$$

By using the Eq. B.2, the total energy E and the longitudinal momentum p_t can be expressed by the transverse mass and the rapidity,

$$E = m_t \cdot \cosh(y), \tag{B.3}$$

$$p_z = m_t \cdot \sinh(y). \tag{B.4}$$

For Ni+Ni collisions at 1.91A GeV, the rapidity of the fixed target is zero in the lab frame. The total energy and the longitudinal momentum of the beam particle have the following forms

$$E = E_{beam} + m_{amu}, \tag{B.5}$$

$$p = \sqrt{E^2 - m_{amu}^2}, \tag{B.6}$$

where E_{beam} is the kinetic energy of the beam per unit mass $m_{amu} = 0.9315$ GeV. Since this is a symmetrical reaction, the rapidity of the center-of-mass frame can be calculated as the following,

$$y_{cm} = \frac{y_{tar} + y_{beam}}{2} = \frac{0. + 1.78}{2} = 0.89 \tag{B.7}$$

Typically, the phase space of the particles in HICs is shown in the plane of mass scaled transverse momentum p_t/m and rapidity y_{lab}.

Two useful relations:

a) Transverse momentum p_t as a function of rapidity y_{lab} with a given polar angle θ. This is used quite frequently to indicate the polar angle acceptance of the detectors. The relation can be derived from Eq. B.4 by using $p_z = p_t/\tan\theta$,

$$p_t = \frac{m}{\sqrt{\left(\frac{\sinh(y)}{\tan(\theta)}\right)^2 - 1}}. \tag{B.8}$$

b) Transverse momentum p_t as a function of rapidity y_{lab} with a given total momentum, which can be derived from Eq. B.3 by using the relation $E = \sqrt{p_{tot}^2 + m^2}$,

$$p_t = \sqrt{\frac{p_{tot}^2 + m^2[1 + \cosh^2(y)]}{\cosh^2(y)}} = m \cdot \sqrt{\frac{(p_{tot}/m)^2 + 1 + \cosh^2(y)}{\cosh^2(y)}}. \tag{B.9}$$

Bibliography

[1] P. Braun-Munzinger and J. Stachel (2002). "Particle ratios, Equilibration and the QCD phase boundary". Journal of Physics G: Nuclear and Particle Physics 28(7):1971-1976 and reference therein.

[2] L. D. McLerran and R. D. Pisarski (2007). "Phases of dense quarks at large". Nuclear Physics A 796(1-4):83-100.

[3] Y. Hidaka, L. D. McLerran, and R. D. Pisarski. (2008). "Baryons and the phase diagram for a large number of colors and flavors". Nuclear Physics A 808(1-4):117-123.

[4] J. Pochodzalla, et al. (1995). "Probing the Nuclear Liquid-Gas Phase Transition". Physical Review Letters 75(6):1040-1043.

[5] B. Borderie and M. F. Rivet (2008). "Nuclear multifragmentation and phase transition for hot nuclei". Progress in Particle and Nuclear Physics 61(2):551-601.

[6] H. Stöcker and W. Greiner (1986). "High energy heavy ion collisions probing the equation of state of highly excited hadronic matter". Physics Reports 137(5-6):277-392.

[7] P. Danielewicz (2001). "Nuclear Equation of State". arXiv:nucl-th/0112006v1.

[8] N. K. Glendenning (1988). "Equation of state from nuclear and astrophysical evidence". Physical Review C 37:2733-2743.

[9] W. G. Lynch, et al. (2009). "Probing the symmetry energy with heavy ions". Progress in Particle and Nuclear Physics 62(2):427-432.

[10] P. Danielewicz, R. Lacey, and W. G. Lynch (2002). "Determination of the Equation of State of Dense Matter". Science 298(5598):1592-1596.

[11] C. Sturm, et al. (2001). "Evidence for a Soft Nuclear Equation-of-State from Kaon Production in Heavy-Ion Collisions". Physical Review Letters 86:39-42.

[12] Z. Xiao, et al. (2009). "Circumstantial Evidence for a Soft Nuclear Symmetry Energy at Suprasaturation Densities". Physical Review Letters 102:062502.

[13] T. Gaitanos, H. Lenske, and U. Mosel (2009). "Formation of hypernuclei in high energy reactions within a covariant transport model". Physics Letters B 675(3-4):297-304.

[14] C. Hartnack, et al. (1998). "Modelling the many-body dynamics of heavy ion collisions: Present status and future perspective". The European Physical Journal A - Hadrons and Nuclei 1(2):151-169.

[15] S. Voloshin and Y. Zhang (1994). "Flow Study in Relativistic Nuclear Collisions by Fourier Expansion of Azimuthal Particle Distributions". Zeitschrift für Physik C Particles and Fields 70(4):665-671.

[16] J.-Y. Ollitrault (1997). "Reconstructing azimuthal distributions in nucleus-nucleus collisions". nucl-ex/9711003.

[17] N. Herrmann, J. P.Wessels, and T. Wienold (1999). "COLLECTIVE FLOW IN HEAVY-ION COLLISIONS". Annual Review of Nuclear and Particle Science 49(1):581-632.

[18] C. Pinkenburg, et al. (1999). "Elliptic Flow: Transition from Out-of-Plane to In-Plane Emission in Au+Au Collisions". Physical Review Letters 83:1295-1298.

[19] A. Andronic, et al. (2005). "Excitation function of elliptic flow in Au+Au collisions and the nuclear matter equation of state". Physics Letters B 612(3-4):173-180.

[20] M. Danysz and J. Pniewski (1953). "Delayed disintegration of a heavy nuclear fragment: I". Philosophical Magazine Series 7 44(350):348-350.

[21] M. Jurič, et al. (1973). "A new determination of the binding-energy values of the light hypernuclei (A≤15)". Nuclear Physics B 52(1):1-30.

[22] W. Brückner, et al. (1975). "Hyperchange exchange reactions on nuclei". Physics Letters B 55(1):107-110.

[23] M. May, et al. (1981). "Observation of Levels in ${}^{13}_{\Lambda}$C, ${}^{14}_{\Lambda}$N, and ${}^{18}_{\Lambda}$O Hypernuclei". Physical Review Letters 47:1106-1109.

[24] C. Milner, et al. (1985). "Observation of Λ-Hypernuclei in the Reaction ${}^{12}C(\pi^+,\ K^+){}^{12}_{\Lambda}C$". Physical Review Letters 54:1237-1240.

[25] P. H. Pile, et al. (1991). "Study of hypernuclei by associated production". Physical Review Letters 66:2585-2588.

[26] M. Akel, et al. (1991). "The (π^+, K^+) reaction on ^{12}C and ^{56}Fe". Nuclear Physics A 534(3-4):478-492.

[27] T. Hasegawa, et al. (1995). "Core-Excited States of ${}^{12}_{\Lambda}$C Hypernuclei Formed in the $(\pi^+,\ K^+)$ reaction". Physical Review Letters 74:224-227.

[28] T. Miyoshi, et al. (2003). "High Resolution Spectroscopy of the ${}^{12}_{\Lambda}$B Hypernucleus Produced by the $(e, e'K^+)$ Reaction". Physical Review Letters 90:232502.

[29] H. Ejiri (1994). "Hypernuclear structure". Nuclear Physics A 574(1-2):311-330.

[30] C. B. Dover, L. Ludeking, and G. E. Walker (1980). "Hypernuclear physics with pions". Physical Review C 22:2073-2093.

[31] O. Hashimoto and H. Tamura (2006). "Spectroscopy of hypernuclei". Progress in Particle and Nuclear Physics 57(2):564-653.

[32] A. S. Goldhaber (1964). "Tests of the One-Pion-Exchange Model". Physical Review Online Archive (Prola) 134:B600-B604.

[33] R. H. Dalitz and A. Gal (1978). "The formation of, and the Γ-radiation from, the p-shell hypernuclei". Annals of Physics 116(1):167-243.

[34] D. J. Millener, et al. (1985). "Spin dependence of the ΛN effective interaction". Physical Review C 31:499-509.

[35] Th.A. Rjken et al. (1999). "Soft-core hyperon-nucleon potentials". Physical Review C 59:21-40.

[36] J. Haidenbauer, W. Melnitchouk, and J. Speth (2001). "A meson exchange model for the YN interaction", nucl-th/0108062v1.

[37] T. Motoba, et al. (1988). "Hypernuclear production by the (π^+,K^+) reaction". Physical Review C 38:1322-1334.

[38] D. J. Millener, et al. (1988). "Λ -nucleus single-particle potentials". Physical Review C 38:2700-2708.

[39] P. Baturin (2010), "SPECTROSCOPY OF ELECTROPRODUCED LIGHT TO MEDIUM MASS LAMBDA HYPERNUCLEI". PhD thesis, FLORIDA INTERNATIONAL UNIVERSITY.

[40] J. Schaffner-Bielich, et al. (2002). "Phase Transition to Hyperon Matter in Neutron Stars". Physical Review Letters 89:171101.

[41] V. Thorsson, et al. (1994). "Composition, structure and evolution of neutron stars with kaon condensates". Nuclear Physics A 572(3-4):693-731.

[42] A. Ramos, J. Schaffner-Bielich, and J. Wambach (2001). "Kaon Condensation in Neutron Stars". arXiv:nucl-th/0011003v3.

[43] R. Rapp, et al. (2000). "High-Density QCD and Instantons". Annals of Physics 280(1):35-99.

[44] M. Alford (2001). "COLOR-SUPERCONDUCTING QUARK MATTER". Annual Review of Nuclear and Particle Science 51(1):131-160.

[45] J. Schaffner-Bielich (2010). "Strangeness in Compact Stars". Nuclear Physics A 835(1-4):279-286.

[46] P. B. Demorest, et al. (2010). "A two-solar-mass neutron star measured using Shapiro delay". Nature 467(7319):1081-1083.

[47] I. Vidañ a, et al. (2011). "Estimation of the effect of hyperonic three-body forces on the maximum mass of neutron stars". EPL (Europhysics Letters) 94, 11002.

[48] E. Friedman and A. Gal (2007). "In-medium nuclear interactions of low-energy hadrons". Physics Reports 452(4-5):89-153.

[49] W.-Z. Jiang, B.-A. Li, and L.-W. Chen (2012). "Large-mass neutron stars with hyperonization". arXiv:1207.1686v1.

[50] P. G. Hansen and J. A. Tostevin (2003). "DIRECT REACTIONS WITH EXOTIC NUCLEI". Annual Review of Nuclear and Particle Science 53(1):219-261.

[51] D. Bazin, et al. (2009). "Mechanisms in Knockout Reactions". Physical Review Letters 102:232501.

[52] A. K. Kerman and M. S. Weiss (1973). "Superstrange Nuclei". Physical Review C 8:408-410.

[53] M. Wakai, H. Band, and M. Sano (1988). "Hypernucleus formation in high-energy nuclear collisions". Physical Review C 38:748-759.

[54] J.žofka, et al. (1990). "On the production of the lightest hypernucleus ${}^{3}_{\Lambda}$H in high energy nuclear collisions". Physics Letters B 235(1-2):25-29.

[55] V. T. Pop and S. D. Gupta (2010). "Model for hypernucleus production in heavy ion collisions". Physical Review C 81:054911.

[56] O. Buss, et al. (2012). "Transport-theoretical description of nuclear reactions". Physics Reports 512(1-2):1-124.

[57] A. S. Botvina, et al. (1987). "Statistical simulation of the break-up of highly excited nuclei". Nuclear Physics A 475(4):663-686.

[58] J. P. Bondorf, et al. (1995). "Statistical multifragmentation of nuclei". Physics Reports 257(3):133-221.

[59] J. Steinheimer, et al. (2012). "Hypernuclei, dibaryon and antinuclei production in high energy heavy ion collisions: Thermal production vs. coalescence". Physics Letters B 714(1):85-91.

[60] D. Henzlova, et al. (2008). "Experimental investigation of the residues produced in the ^{136}Xe+Pb and ^{124}Xe+Pb fragmentation reactions at 1A GeV". Physical Review C 78:044616.

[61] V. Föhr, et al. (2011). "Experimental study of fragmentation products in the reactions ^{112}Sn+^{112}Sn and ^{124}Sn+^{124}Sn at 1A GeV". Physical Review C 84:054605.

[62] A. Bacquias, et al. (2012). "Dispersion of longitudinal momentum distributions induced in fragmentation reactions". Physical Review C 85:024904.

[63] P. Braun-Munzinger, et al. (1995). "Thermal equilibration and expansion in nucleus-nucleus collisions at the AGS". Physics Letters B 344(1-4):43-48.

[64] P. Braun-Munzinger, I. Heppe, and J.Stachel (1999). "Chemical equilibration in Pb+Pb collisions at the SPS". Physics Letters B 465(1-4):15-20.

[65] A. Andronic, et al. (2010). "Hadron production in ultra-relativistic nuclear collisions: Quarkyonic matter and a triple point in the phase diagram of QCD". Nuclear Physics A 837(1-2):65-86.

[66] K. J. Nield, et al. (1976). "Production of hypernuclei in a 2.1 GeV/nucleon oxygen beam". Physical Review C 13:1263-1266.

[67] A. U. Abdurakhimov, et al. (1989). "Experimental study of relativistic hypernuclei using the HYBS-spectrometer". Il Nuovo Cimento A (1971-1996) 102(2):645-652.

[68] S. Avramenko, et al. (1992). "A study of the production and lifetime of the lightest relativistic hypernuclei". Nuclear Physics A 547(1-2):95-100.

[69] T. Armstrong, et al. (2004). "Production of $^{3}_{\Lambda}$H and $^{4}_{\Lambda}$H in central 11.5 GeV/c Au+Pt heavy ion collisions". Physical Review C 70:024902.

[70] The STAR Collaboration (2010). "Observation of an Antimatter Hypernucleus". Science 328(5974):58-62. and references therein.

[71] T. R. Saito, et al. (2012). "Production of hypernuclei in peripheral HI collisions: The HypHI project at GSI". Nuclear Physics A 881:218-227.

[72] J. Ciborowski, et al. (1982). "Kaon scattering and charged Sigma hyperon production in K^-p interactions below 300 MeV/c". Journal of Physics G: Nuclear Physics 8(1):13.

[73] D. Evans, et al. (1983). "Charge-exchange scattering in K^-p interactions below 300 MeV/c". Journal of Physics G: Nuclear Physics 9(8):885.

[74] W. E. Humphrey and R. R. Ross (1962). "Low-Energy Interactions of K^- Mesons in Hydrogen". Physical Review Online Archive (Prola) 127:1305-1323.

[75] M. Sakitt, et al. (1965). "Low-Energy K^--Meson Interactions in Hydrogen". Physical Review Online Archive (Prola) 139:B719-B728.

[76] M. Iwasaki, et al. (1997). "Observation of Kaonic Hydrogen K_α X Rays". Physical Review Letters 78:3067-3069.

[77] G. Beer, et al. (2005). "Measurement of the Kaonic Hydrogen X-Ray Spectrum". Physical Review Letters 94:212302.

[78] M. Bazzi, et al. (2011). "A new measurement of kaonic hydrogen X-rays". Physics Letters B 704(3):113-117.

[79] E. Friedman, A. Gal, and C. J. Batty (1994). "Density-dependent K^- nuclear optical potentials from kaonic atoms". Nuclear Physics A 579(3-4):518-538.

[80] E. Friedman, et al. (1999). "K^--nucleus relativistic mean field potentials consistent with kaonic atoms". Physical Review C 60:024314.

[81] N. Kaiser, P. B. Siegel, and W. Weise (1995). "Chiral dynamics and the low-energy kaon-nucleon interaction". Nuclear Physics A 594(3):325-345.

[82] T. Waas, N. Kaiser, and W. Weise (1996). "Low energy N interaction in nuclear matter". Physics Letters B 365(1-4):12-16.

[83] A. Ramos and E. Oset (2000). "The properties of $\bar{K}$ in the nuclear medium". Nuclear Physics A 671(1-4):481-502.

[84] A. Baca (2000). "Deeply bound levels in kaonic atoms". Nuclear Physics A 673(1-4):335-353.

[85] T. Yamazaki and Y. Akaishi (2002). "(K^-, π^-) production of nuclear K^- bound states in proton-rich systems via doorways". Physics Letters B 535(1-4):70-76.

[86] Y. Akaishi and T. Yamazaki (2002). "Nuclear $\bar{K}$ bound states in light nuclei". Physical Review C 65:044005.

[87] T. Yamazaki, A. Doté, and Y. Akaishi (2004). "Invariant-mass spectroscopy for condensed single- and double-$\bar{K}$ nuclear clusters to be formed as residues in relativistic heavy-ion collisions". Physics Letters B 587(3-4):167-174.

[88] D. Jido, et al. (2003). "Chiral dynamics of the two $\Lambda(1405)$ states". Nuclear Physics A 725:181-200.

[89] M. Agnello, et al. (2005). "Evidence for a Kaon-Bound State K^-pp Produced in K^- Absorption Reactions at Rest". Physical Review Letters 94:212303.

[90] V. K. Magas, et al. (2006). "Critical view on the deeply bound K^- system". Physical Review C 74:025206.

[91] T. Yamazaki, et al. (2010). "Indication of a Deeply Bound and Compact K^-pp State Formed in the $pp \to p + \Lambda + K^+$ Reaction at 2.85 GeV". Physical Review Letters 104:132502.

[92] J. Siebenson (2011). "Strange baryon resonances in pp collisions measured with HADES". Hyperfine Interactions pp. 1-8.

[93] Ch. Hartnack, H. Oeschler, and J. Aichelin (2003). "What Determines the K^- Multiplicity at Energies Around (1-2)A GeV?". Physical Review Letters 90:102302.

[94] M. Menzel, et al. (2000). "First measurement of antikaon phase-space distributions in nucleus-nucleus collisions at subthreshold beam energies". Physics Letters B 495(1-2):26-32.

[95] N. Herrmann (2009). "Probing dense baryonic matter with strangeness". Progress in Particle and Nuclear Physics 62(2):445-450.

[96] N. Herrmann (2005), "Search for $ppnK^-$ deeply bound states with FOPI", Proceedings of the EXA05 conference, Vienna (2005), Österreichische Akademie der Wissenschaften, 73, ISBN 3-7001-3616-1.

[97] J. Schaffner, et al. (1994). "Kaon effective mass and energy in dense nuclear matter". Physics Letters B 334(3-4):268-274.

[98] G. Q. Li and C. M. Ko (1995). "Kaon flow in heavy-ion collisions". Nuclear Physics A 594(4):460-482.

[99] W. Weise (1996). "Hadrons in dense baryonic matter". Nuclear Physics A 610:35-48.

[100] A. Gobbi, et al. (1993). "A highly-segmented E-time-of-flight wall as forward detector of the 4π-system for charged particles at the SIS/ESR accelerator". NIM, A324(1-2):156-176.

[101] P. Crochet, et al. (1997). "Onset of nuclear matter expansion in Au+Au collisions". Nuclear Physics A 624(4):755-772.

[102] A. Andronic, et al. (2001). "Transition from in-plane to out-of-plane azimuthal enhancement in Au+Au collisions". Nuclear Physics A 679(3-4):765-792.

[103] D. Pelte, et al. (1997). "Charged pions from In on In collisions between 1 and 2A GeV". Zeitschrift für Physik A Hadrons and Nuclei 359(1):55-65.

[104] D. Best, et al. (1997). "K^+ production in the reaction ^{58}Ni+^{58}Ni at incident energies from 1 to 2A GeV". Nuclear Physics A 625(1-2):307-324.

[105] A. Mangiarotti, et al. (2003). "Sub-threshold ϕ-meson yield in central collisions". Nuclear Physics A 714(1-2):89-123.

[106] M. Merschmeyer, et al. (2007). "K^0 and Λ production in Ni+Ni collisions near threshold". Physical Review C 76:024906.

[107] X. Lopez, et al. (2007). "Subthreshold production of $\Sigma(1385)$ baryons in Al+Al collisions at 1.9A GeV". Physical Review C 76:052203.

[108] M. Kǐs et al. (2010). "A Multi-strip Multi-gap RPC Barrel for Time-of-Flight Measurements". NIM A646(1):27-34.

[109] H. Drumm, et al. (1980). "Experience with the jet-chamber of the JADE detector at PETRA". Nuclear Instruments and Methods 176(1-2):333-344.

[110] R. D. Heuer and A. Wagner (1988). "The OPAL jet chamber". Nuclear Instruments and Methods in Physics Research Section A: Accelerators, Spectrometers, Detectors and Associated Equipment 265(1-2):11-19.

[111] H. M. Fischer, et al. (1989). "The OPAL jet chamber". Nuclear Instruments and Methods in Physics Research Section A: Accelerators, Spectrometers, Detectors and Associated Equipment 283(3):492-501.

[112] Markus Merschmeyer (2004). "Production and Flow of neutral strange particles in Ni+Ni at 1.93A GeV". PhD thesis, Universitüat Heidelberg.

[113] Lotfi Benabderrahmane (2007). "Measurement of the K^0 inclusive cross section in pion-induced reactions at 1.15 GeV/c". PhD thesis, Universitüat Heidelberg.

[114] C. Lippmann (2012). "Particle identification". NIM, A666:148-172

[115] Teaim Kang (2011). "Flow measurements of charged Kaons in ^{58}Ni+^{58}Ni collisions at 1.91A GeV." Phd thesis, Korea University.

[116] I.M. Deppner (2008). "Bestimmung von Detektor-Eigenschaften in Abhaengigkeit von Gasmischungen fuer Resistive Plate Chambers". Diploma Thesis, Universitüat Heidelberg.

[117] P. Danielewicz and G. Odyniec (1985). "Transverse momentum analysis of collective motion in relativistic nuclear collisions". Physics Letters B 157(2-3):146-150.

[118] D. Bertrand, et al. (1970). "Branching ratios for the π^--msonic decays of the hypernuclei $^3_\Lambda$H and $^4_\Lambda$H ". Nuclear Physics B 16(1):77-84.

[119] G. Keyes, et al. (1973). "A measurement of the lifetime of the $^3_\Lambda$H hypernucleus". Nuclear Physics B 67(2):269-283. and the references therein.

[120] M. Raymund (1964). "The binding energy difference between the hypernuclides ^{4}He$_\Lambda$ and ^{4}H$_\Lambda$". Il Nuovo Cimento (1955-1965) 32(3):555-587.

[121] G. Bohm, et al. (1968). "A determination of the binding-energy values of light hypernuclei". Nuclear Physics B 4(6):511-526.

[122] W. Gajewski, et al. (1967). "A compilation of binding energy values of light hypernuclei". Nuclear Physics B 1(3):105-113.

[123] H. Outa, et al. (1992). "Lifetime measurement of $^4_\Lambda$H hypernucleus". Nuclear Physics A 547(1-2):109-114.

[124] D. Drijard, H. G. Fischer, and T. Nakada (1984). "Study of event mixing and its application to the extraction of resonance signals". NIM, A225(2):367-377.

[125] D. L'Hôte(1994). "About resonance signal extraction from multiparticle data: combinatorics and event mixing methods". NIM, A337(2-3):544-556.

[126] N.Herrmann (2005). "Search for ppnK$^-$ deeply bound states with FOPI". Proc. EXA05, Ed, A.Hirtl et al. Austrian Academy of Science Press, Vienna.

[127] Y.-S. Zhu (2008). "On Statistical Significance of Signal". arXiv:0812.2708.

[128] http://wwwasdoc.web.cern.ch/wwwasdoc/geant/geantall.html

[129] http://cernlib.web.cern.ch/cernlib

[130] J. Aichelin (1991). " "Quantum" molecular dynamics-a dynamical microscopic n-body approach to investigate fragment formation and the nuclear equation of state in heavy ion collisions". Physics Reports 202(5-6):233-360.

[131] P. J. Siemens and J. O. Rasmussen (1979). "Evidence for a Blast Wave from Compressed Nuclear Matter". Physical Review Letters 42:880-883.

[132] http://pdg.lbl.gov/2012/listings/rpp2012-list-lambda.pdf

[133] R. J. Prem and P. H. Steinberg (1964). "Lifetimes of hypernuclei, ${}^{3}_{\Lambda}$H ,${}^{4}_{\Lambda}$H, ${}^{5}_{\Lambda}$H". Physical Review 136, B1803.

[134] G. Keyes, et al. (1968). "New Measurement of the ${}^{3}_{\Lambda}$H Lifetime". Physical Review Letters 20:819-821.

[135] R. E. Phillips and J. Schneps (1969). "Lifetimes of Light Hyperfragments. II". Physical Review Online Archive (Prola) 180:1307-1318.

[136] G. Bohm, et al. (1970). "On the lifetime of the ${}^{3}_{\Lambda}$H ypernucleus". Nuclear Physics B 16(1):46-52.

[137] G. Keyes, et al. (1970). "Properties of ${}^{3}_{\Lambda}$H". Physical Review D 1:66-77.

[138] H. Outa, et al. (1992). "Lifetime measurement of ${}^{4}_{\Lambda}$H hypernucleus". Nuclear Physics A 547(1-2):109-114.

[139] R. E. Phillips and J. Schneps (1969). "Lifetimes of Light Hyperfragments. II". Physical Review Online Archive (Prola) 180:1307-1318.

[140] Private communication.

[141] J. M. Heuser (2011). "The Compressed Baryonic Matter Experiment at FAIR". EPJ Web of Conferences 13:03001.

[142] J. Beringer, et al. (2012). "Review of Particle Physics". Physical Review D 86:010001.

Acknowledgment

First of all, I am deeply grateful to Prof. Dr. Norbert Herrmann for giving me the chance to study at Heidelberg University and to work in the FOPI collaboration, for his patience guidance and continuous support. His passion about the research always motivates and encourages me to go to forward.

I am grateful to my co-advisors Prof. Dr. Johanna Stachel and Prof. Dr. Jürgen Schaffner-Bielich, for their suggestions and concerns about my research progress. I appreciate that Prof. Dr. Johanna Stachel agreed to be a second referee of this thesis. Thanks to Prof. Dr. Jürgen Schaffner-Bielich and Prof. Dr. Matthias Bartelmann for willing to be a member of my final examination committee.

Thanks to Dr. Krzysztof Wiśniewski and Dr. Krzysztof Piasecki for helping me to solve the simulation problems and your fruitful discussions about the analysis. I would like to express my gratitude to Victoria Zinyuk, Christian Simon, Ingo Martin Deppner, and Dr. Sean McConnell, for proof-reading the manuscript. Without your help and encouragement, this work would not finish like this. I would like to thank other colleagues in Heidelberg, Pierre-Alain Loizeau, Dr. Jianli Liu, Changzhou Xiang, Dr. Tea Im Kang and Dr. Andreas Reischl, not only for sharing a pleasant working environment, but more so for the friendship, which I really appreciate.

Thanks to Dr. Anton Andronic at GSI for providing the thermal predictions.

I wish to thank all members of the FOPI collaboration, especially Dr. Yvonne Leifels, Dr. Mladen Kiš, Dr. Arnaud Le Fèvre, Prof. Laura Fabbietti, Dr. Ralf Averbeck, Dr. Willibrord Reisdorf, Igor Gašparić, Dr. Olaf Hartmann, Dr. Ken Suzuki, Prof. Byungsik Hong, Prof. Fouad Rami, Dr. Min Sang Ryu, Dr. Klaus Dieter Hildenbrand, Dr. Jozsef Kecskemeti, Dr. Marek Kirejczyk, Dr. Roland Kotte, Dr. Piotr Koczoń, Alexander Lebedev, Robert Münzer, Prof. Mihai Petrovici, Dr. Zoltan Seres, Prof. Brunon Sikora, Prof. Krystyna Siwek-Wilczyńka, Dr. Zbigniew Tyminski, Dr. Zoran Basrak, Dr. Roman Čaplar, Martin Berger, Robert Münzer, Dr. Piotr Gasik, Paul Bühler, Igor Yushmanov and Dr. Alexander Zhilin, for your advice and concerns.

Thanks to Prof. Dr. Sandra Klevansky, Ms. Gesine Heinzelmann and Ms. Elisabeth Miller of HGSFP, for your support and organization.

Thanks to my friends in Heidelberg, your help and understanding are also important.

I want to extend my acknowledgement to Prof. Zhigang Xiao at Tsinghua University, China. Without his suggestion and recommendation, this impressive period would not even have had a start.

Last, but not least, I would like to thank my parents, my sister, brother-in-law, as well as other family members. Your love and support are so important to me that I can never appreciate it enough.